Electrochemistry of Single Nanoparticles

Xiuting Li

Hertford College

A thesis submitted for the degree of Doctor of Philosophy in Physical and Theoretical Chemistry

Michaelmas Term 2017

Abstract

This thesis presents experimental work with two main aims: one is the detection and characterization of single electrocatalytic nanoparticles with an emphasis on metal nanoparticle decorated carbon nanotubes, and the other is to develop a more comprehensive understanding of nanoscale electrocatalysis by exploring the differences in the electrocatalytic behaviour of single nanotubes as compared to their ensembles. The first chapter introduces the basic principles and techniques of electrochemistry and the second chapter gives a brief introduction to the nanomaterials and electrochemical methods used in this thesis.

Chapter 3 first reports the detection of individual carbon nanotubes with the 'nano-impact' method using the production of the under-potential deposited hydrogen (H_{UPD}) from proton reduction on palladium nanoparticle decorated carbon nanotubes (CNT-Pds). The current spikes corresponding to the reduction of proton forming H_{UPD} on the individual impacting CNT-Pds were detected via chronoamperometry. From the knowledge of the palladium nanoparticle sizes and their coverage on the CNTs it was further demonstrated how the magnitude of impact charge allows an assessment of the nanotube lengths. The correspondence between electrochemical sizing and microscopy results directly shows that a CNT-Pd is electroactive along its entire length, evidencing the reactivity and conductivity of the CNTs and further indicating the complete H_{UPD} saturation of the palladium nanoparticles decorated on the carbon nanotubes.

Chapter 4 then extends electrocatalytic nano-impacts of single CNT-Pd to investigate the hydrogen oxidation reaction (HOR). A facile procedure which enables rapidly and easily gathering single nanotube voltammetry was established and validated. Single CNT-Pds impact a micro wire electrode from dilute suspension and adhere to it for a sufficiently long

time for cyclic voltammetry to be conducted. The single adsorbed decorated CNT is electro-catalytic towards HOR which thus occurs exclusively on it and cyclic voltammetry on single decorated carbon nanotube is realized. Single nanotube voltammetry of oxygen reduction reaction (ORR) was further studied and reported in Chapter 5. It demonstrates that the reduction of oxygen on Pd involves the initial formation of absorbed superoxide with fast electron transfer kinetics but with a low apparent transfer coefficient due to double layer effects arising from the Coulombic interactions of the adsorbed superoxide species inside the double layer. The mechanism of ORR on Pd was re-evaluated.

Chapter 6 compares the oxidation of formate and of methanol at the single CNT-Pds and ensemble levels. Pd oxide formation as a competitive reaction with formate or methanol oxidation is significantly inhibited at high overpotentials at single nanotubes in comparison with what is seen with ensembles. The discovery of the superior electro-catalytic performance under high mass transport conditions created by single nanotubes suggests requirements for the design of better fuel cell development and offers the scope for new catalytic approaches to be developed.

Chapter 7 is focused on the study of the origins of the current fluctuation observed in the single nanotube voltammetry by comparing the responses of HOR at a single CNT-Pds immobilised on the gold surface to analogous data on a carbon substrate. No significant distinction between the gold and carbon was found, demonstrating that the physical motion of the nanotube at the electrode is likely responsible for the modulation of current. A simple and feasible methodology based on the ‘nano-impact’ method is then developed to enable the measurement of the resistance across individual carbon nanotube-electrode contacts. It reveals that the major component of the measured resistance is associated with the single CNT-gold contact, which has major implications for the widespread use of CNTs as electro-catalysts and as catalyst supports.

Acknowledgements

First and foremost, I would like to thank my supervisor, Professor Richard Compton, for welcoming me into his wonderful research group and providing me with such amazing opportunities and experiences over the last three years. Thank him for giving valuable guidance and inspiration in both my work and life. I would also like to express my deep gratitude to Dr. Christopher Batchelor-McAuley for his great support and for being always patient and helpful. I have learnt a lot from both of you during my time here. This thesis would not have been possible without your help and guidance.

Thank you to for all the members of the Compton group. You make the lab such a lovely place to work in. Thanks to Chuhong and Dr. Eduardo Laborda for your suggestions and help with the simulations. Thanks also go to Professor Lior Sepunaru, Dr. Enno Kätelhön and Professor Kristina Tschulik for your very helpful and professional advice. To my 'lunch' buddies: Ivana, Chuhong, Dia and Crystal, thank you very much for your companionship, encouragement and immeasurable support. I would never forget the time I spent here with all of you.

Thanks to the China Scholarship Council for financially supporting my DPhil study. I am also very grateful to my colleges, Hertford and Exeter, who have provided me with a home, lots of dinners and generous scholarship.

Last but not the least, I would like to thank my family for always giving me your endless love and care. You are always unconditionally supportive in the choices that I've made. I'm so lucky to have such a great family.

Glossary

Roman Symbols

Symbol	Meaning	Unit
A	frequency factor	unitless
A, B	species	
A_{elec}	electrode area	cm^2
(aq)	aqueous solution	
C	concentration	mol cm^{-3}
c_0, c_1	constant	
d	diffusion layer thickness	cm
D	diffusion coefficient	$cm^2\ s^{-1}$
E	electrode potential	V
E_0	standard electrode potential	V
E_f^0	formal electrode potential	V
$E_{1/2}$	half-wave potential	V
E_{mid}	mid-point potential	V
E_p	peak potential	V
ΔE_p	peak-to-peak separation	V
F	Faraday constant (96485)	C mol^{-1}
G	Gibbs energy	J mol^{-1}
I	current	A
I_p	peak current	A

I_{ss}	steady-state current	A
I_{qss}	quasi-steady state current	A
j	species	
J	flux	mol cm^{-2} s^{-1}
k^0	standard electrochemical rate constant	cm s^{-1}
$k_a;\ k_c$	anodic, cathodic rate constant	cm s^{-1}
K	Henry's law constant	Pa cm^3 mol^{-1}
l	electrode length	cm
(M)	electrode metallic phase	
m	mass	g
m_T	mass transport coefficient	cm s^{-1}
M	molar mass	mol cm^{-3}
n	number of electrons transferred	unitless
Q	charge	C
r_e	electrode radius	cm
R	universal gas constant (8.314)	J K^{-1} mol^{-1}
R	resistance	Ω
(S)	solution phase	
t	time	s
T	temperature	K
v	potential scan rate	V s^{-1}
v'	solution velocity resulting from convection	cm s^{-1}
x	distance perpendicular to the electrode surface	

Z	charge number	unitless

Greek Symbols

Symbol	Meaning	Unit
α, β	transfer coefficients	unitless
Δ	difference in a quantity	
∇	three dimensional vector gradient	
η	overpotential	V
γ	activity coefficient	unitless
Γ^0	surface coverage	mol cm^{-2}
Λ	Matsuda-Ayabe parameter	unitless
μ	chemical potential	J mol^{-1}
$\overline{\mu}$	electrochemical potential	J mol^{-1}
ϕ	electrical potential	V
τ	dimensionless time	unitless
κ	reversibility transition parameter	unitless
$\theta_{1/2}$	dimensionless half-wave potential	unitless

Contents

Chapter 1

Fundamentals of Electrochemistry

This chapter gives an overview of the fundamental aspects of electrochemistry and associated electrochemical techniques. These will aid in the understanding of the experimental results and their interpretation as reported later in this thesis. Topics covered in this chapter include the description of electrochemical equilibrium, electrode kinetics, the electrochemical cell, mass transport phenomena and voltammetric techniques.

1.1 Electrochemical Equilibrium

Electrochemistry is the important branch of physical chemistry which studies the interaction between electricity and chemical change. It involves electric charges moving between electrodes and an electrolyte. Instead of studying direct electron transfer between molecules and/or atoms as in *chemical* reactions, electrochemistry deals with the overall reactions with individual redox reactions separated but connected by an external electric circuit and an intervening electrolyte. An *electrochemical* reaction includes either a chemical reaction caused by an external power supply, as in electrolysis, or the creation of an electric current as an outcome of a spontaneous chemical reaction as in a battery. Understanding the overall electrochemical reactions requires separate interpretation for each particular electrode-solution interface.[1]

In general, whenever two dissimilar conducting phases are brought into contact, an electric potential is developed across the interface.[2] Particularly for an electrode (e.g. metal) in a

solution consisting of a redox species A^z or B^{z-1}, the following simple heterogeneous electron transfer at the electrode-solution interface is assumed,

$$\boldsymbol{A^z_{(aq)} + e^-_{(m)} \rightleftharpoons B^{z-1}_{(aq)}} \qquad \textbf{(1.1)}$$

where A^z and B^{z-1} are the oxidised and reduced forms of the redox couple in solution phase. In the electronic structure of a metal, electrons fill its conduction band up to an energy maximum known as the *Fermi level.* We first, from a thermodynamic aspect, consider the situation in which the *Fermi level* of the electrode is higher than the lowest unoccupied molecular orbital (LUMO) of A^z in the solution phase, as illustrated in the energy level diagrams in Figure 1.1 (left). In this case it is energetically favorable for the electrons leaves the *Fermi level* to join the species A^z forming B^{z-1}. As the electron transfer proceeds, the *Fermi level* of the electrode becomes progressively lower. When it has a lower energy level than the highest occupied molecular orbital (HOMO) of the formed B^{z-1}, the electron transfer is in the opposite direction and B^{z-1} is oxidized to A^z, as shown in Figure 1.1 (right). The *Fermi level* of the electrode locates between the LUMO of A^z and the HOMO of B^{z-1} making both A^z to B^{z-1} and B^{z-1} to A^z thermodynamically favorable. If kinetically the reaction rate of these two directions becomes the same, a dynamic equilibrium is achieved. No further net change in terms of either the components of the solution phase or the electron energy level of the electrode is observed at this point. Charge separations, at this time, are created at the interface between the electrode and the solution.[3] This is the origin of the electrode potential.

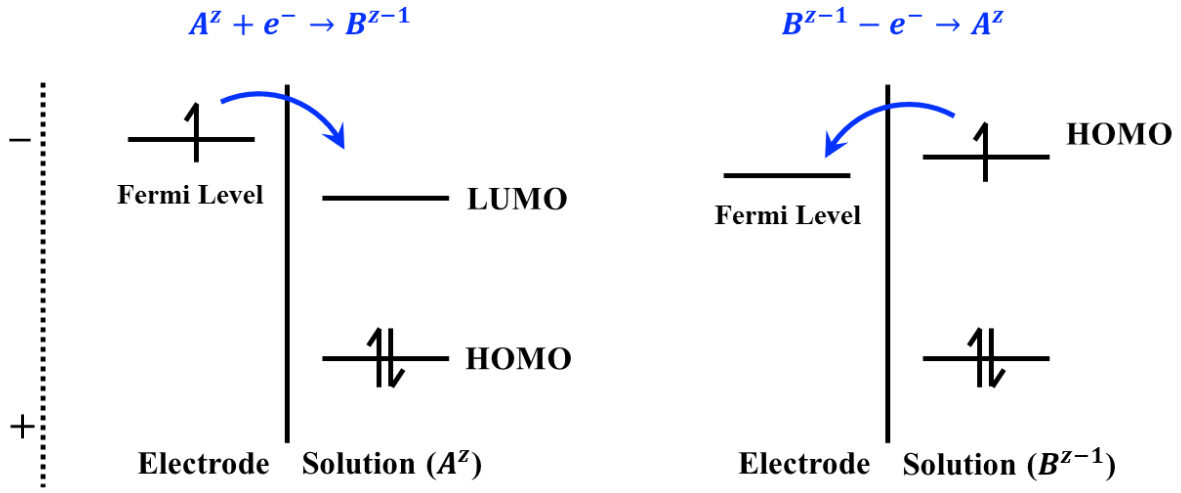

Figure 1.1: Illustration of the energy levels (not to scale) during reduction of A^z (left) and oxidation of B^{z-1} (right).

For an electrochemical equilibrium as above, the position of the equilibrium represents the balance between not only the chemical energies but also the electrical energies of all the involved entities because the electron transferred between the electrode and the solution may experience two different electrical potentials, $\emptyset_M$ (electrode) and $\emptyset_S$ (solution) respectively. To account for both the chemical energies and electrical energies of a specific species (j), the concept of electrochemical potential ($\overline{\mu}_j$) is introduced[1],

$$\overline{\mu}_j = \mu_j + Z_j F \emptyset \tag{1.2}$$

where the first term, μ_j, is chemical potential of molecule j, Z_j is the charge on j, F is the Faradic constant (96485 C mol^{-1}) indicating that the charge passed per mole of electrons and $\emptyset$ is the potential of the electrode ($\emptyset_M$) or solution ($\emptyset_S$). The second term here represents the electrical energy of j which has the same units as the chemical potential (Gibbs energy per mole).

For the electrochemical reaction in equation (1.1) at equilibrium,

$$\overline{\mu}_{A^z} + \overline{\mu}_{e^-} = \overline{\mu}_{B^{z-1}} \tag{1.3}$$

so that

$$(\boldsymbol{\mu_{A^z}} + \boldsymbol{ZF\emptyset_S}) + (\boldsymbol{\mu_{e^-}} - \boldsymbol{F\emptyset_M}) = [\boldsymbol{\mu_{B^{z-1}}} + (\boldsymbol{Z-1})\boldsymbol{F\emptyset_S}] \quad \textbf{(1.4)}$$

Rearranging equation (1.4) gives

$$\boldsymbol{F}(\emptyset_M - \emptyset_S) = \boldsymbol{\mu_{A^z}} + \boldsymbol{\mu_{e^-}} - \boldsymbol{\mu_{B^{z-1}}} \quad \textbf{(1.5)}$$

Expanding the chemical potential terms in equation (1.5) using

$$\boldsymbol{\mu_{A^z}} = \boldsymbol{\mu^0_{A^z}} + \boldsymbol{RT}\ \ln\left(\frac{[A^z]}{[\ ]^0}\right) \quad \textbf{(1.6)}$$

$$\boldsymbol{\mu_{B^{z-1}}} = \boldsymbol{\mu^0_{B^{z-1}}} + \boldsymbol{RT}\ \ln\left(\frac{[B^{z-1}]}{[\ ]^0}\right) \quad \textbf{(1.7)}$$

where R is the gas constant (8.314 J K^{-1} mol^{-1}), T is the absolute temperature (K), $[\ ]^0$ is the standard concentration (1 mol dm^{-3}) and $[\ j\ ]$ is the concentration (mol dm^{-3}) of the species.

Equation (1.5) becomes

$$\emptyset_M - \emptyset_S = \frac{\Delta\boldsymbol{\mu^0}}{\boldsymbol{F}} + \frac{\boldsymbol{RT}}{\boldsymbol{F}}\ln\left(\frac{[A^z]}{[B^{z-1}]}\right) \quad \textbf{(1.8)}$$

where

$$\Delta\boldsymbol{\mu^0} = \boldsymbol{\mu^0_{A^z}} + \boldsymbol{\mu_{e^-}} + \boldsymbol{\mu^0_{B^{z-1}}} \quad \textbf{(1.9)}$$

which is a constant at a given temperature and pressure. Equation (1.8) is the *Nernst equation*[1] associated with a single electrode-solution interface which characterizes the position of the electrochemical equilibrium of the A^z/B^{z-1} redox couple at the single interface. Note that the above expressions (1.6) and (1.7) are for the chemical potential of the species in solution, thus the standard concentration ($[\ ]^0 = 1$ mol dm^{-3}) is used. For reactions involving gases, a standard pressure ($P^0 = \sim 10^5$ N m^{-2}) for the gases is used instead. The

chemical potential of pure solid or liquid is equal to their standard chemical potential; there is no term corresponding to concentration or pressure.

The *Nernst equation* (1.8), however, is only correct for an ideal solution. The equation needs to be modified in order to allow for non-ideality. The 'activity coefficient' (γ) considers the extent of the ion-ion and ion-solvent interactions in concentrated non-ideal solutions and is introduced accordingly, so that equation (1.8) becomes

$$\emptyset_M - \emptyset_S = \frac{\Delta\mu^0}{F} + \frac{RT}{F}\ln\left(\frac{\gamma_{A^z}[A^z]}{\gamma_{B^{z-1}}[B^{z-1}]}\right) \quad \textbf{(1.10)}$$

Equation (1.10), despite considering non-ideality, only *theoretically* quantifies the position of the electrochemical equilibrium (electrode potential) of single electrode-solution interface. *Measuring* such an absolute value is experimentally impossible. Two such interfaces are required to form a circuit for a connected voltmeter to make the measurement. If the content of solution at the second electrode-solution interface is maintained constant during the measurement, the change of the measured potential difference between the two electrodes, E, represents the change of the target electrode potential. Such a second electrode is called a 'reference electrode'.[4]

$$E = (\emptyset_M - \emptyset_S)_{test} - (\emptyset_M - \emptyset_S)_{reference} \quad \textbf{(1.11)}$$

so that

$$E = c_0 + \frac{RT}{F}\ln\left(\frac{\gamma_{A^z}[A^z]}{\gamma_{B^{z-1}}[B^{z-1}]}\right) \quad \textbf{(1.12)}$$

where c_0 is a constant. Note that the solution which has a finite 'conductivity' may account for certain potential drop, therefore an additional term 'IR' could in principle appear in the right-hand side of equation (1.11). However, this is negligible since the current, I, during the potential measurement is tiny if suitable instrumentation is used.

Electrode potentials (including other reference electrodes) are measured against the standard hydrogen electrode (SHE). In particular, the standard electrode potential (E^0) of arbitrary redox couples (e.g. $A^z/\ B^{z-1}$) is measured against the standard hydrogen electrode and the concentrations of the two ions are carefully chosen to make sure both of their activity ($\gamma_j[\ j\ ]$) are unity. The 'ln' term in the expression, therefore, disappears. The *Nernst equation* can be expressed with E^0 embedded as

$$\boldsymbol{E\ =\ E^0 + \frac{RT}{F}\ln(\frac{\gamma_{A^z}[A^z]}{\gamma_{B^{z-1}}[B^{z-1}]})} \qquad \textbf{(1.13)}$$

where E is the electrode potential against the SHE, E^0 is the standard electrode potential at unity activity. The formal potential E_f^0 with respect to standard potential and activity coefficient can be expressed as,

$$\boldsymbol{E_f^0\ =\ E^0 + \frac{RT}{F}\ln(\frac{\gamma_{A^z}}{\gamma_{B^{z-1}}})} \qquad \textbf{(1.14)}$$

Thus, the *Nernst equation* becomes

$$\boldsymbol{E\ =\ E_f^0 + \frac{RT}{F}\ln(\frac{[A^z]}{[B^{z-1}]})} \qquad \textbf{(1.15)}$$

Although the standard potential (E^0) has thermodynamic generality, it is restricted to very specific conditions. In contrast, the formal potential (E_f^0) tends to be more helpful when doing experiments since it considers not only the influence of temperature and pressure as E^0 but also the different practical electrolyte environment associated with the various concentrations of the redox species and existing supporting medium.

The above *Nernst equations* (1.10), (1.13) and (1.15) successfully describe the relationship between potential and concentrations of the redox species and it is only applicable to a system at a dynamic equilibrium. The establishment of the latter requires fast electrode

kinetics. Thus the next section considers the interpretation of the kinetics of electrode processes.

1.2 Electrode Kinetics

In last section, we discussed electrochemical equilibrium which is characterized by the *Nernst equation*. Thermodynamics describes only the equilibrium state. No information is given by thermodynamics regarding the important mechanism of approaching and maintaining equilibrium. In contrast, kinetics *quantitatively* describes evolution of chemical change, including both the approach to equilibrium and the dynamic maintenance of that state. Thus, in this section we present theory by which the kinetics of electrode processes can be interpreted.

First we recognize the experimental fact that the natural logarithm of most rate constants of solution phase reactions is linear with the reciprocal of the temperature. Arrhenius proposed the following rate constant expression[5]:

$$\boldsymbol{k} = \boldsymbol{A}\, \boldsymbol{e}^{\frac{-\Delta \boldsymbol{G}^{\ddagger}}{\boldsymbol{RT}}} \tag{1.16}$$

where $\Delta G^{\ddagger}$ is the *standard Gibbs energy of activation*. The exponential term represents the probability of surmounting the barrier between reactant and product, A is the frequency factor for the reaction, describing the frequency of attempts on it, R is the universal gas constant and T is the temperature.

Consider the following simple electrochemical reaction

$$\boldsymbol{A}^{\boldsymbol{z}}_{(\boldsymbol{aq})} + \boldsymbol{e}^{-}_{(\boldsymbol{m})} \underset{\boldsymbol{k}_a}{\overset{\boldsymbol{k}_c}{\rightleftharpoons}} \boldsymbol{B}^{\boldsymbol{z-1}}_{(\boldsymbol{aq})} \tag{1.17}$$

at an electrode of area, A_{elec} (cm^2), where k_c and k_a are heterogeneous electron transfer rates of the forward (reduction of A^z to B^{z-1}) and backward (oxidation of B^{z-1} to A^z) reactions respectively. At the electrode-solution interface, the electron transfer process between the electrode and the reactant, A^z, takes place via quantum mechanical tunneling which requires A^z to be located within the distance of 10 ~ 20 ˚A of the electrode because within this zone the electron wavefunctions of A^z and the electrode can overlap.[6] The rate of tunneling drops very significantly when the reactants are located a greater distance from the electrode. Thus the concentration of the redox species which close to the electrode surface ($[\,j\,]_0$) instead of that in the remote bulk solution overwhelmingly predominantly attributes to the electron transfer at the interface. With the essential aid of a second electrode, the electron transfer will lead to the passage of an electrical current through the electrode[7, 8],

$$\boldsymbol{I = nFA_{elec}J} \tag{1.18}$$

where n is the number of the transferred electrons and equals 1 for reaction (1.17), F is Faraday constant (96485 C mol^{-1}), A_{elec} is the electrode area (cm^2) and J (mol cm^{-2} s^{-1}) is the heterogeneous reaction flux at the interface:

$$\boldsymbol{J = k_c[A^z]_0 - k_a[B^{z-1}]_0} \tag{1.19}$$

where k_c and k_a are heterogeneous electron transfer rates of the cathodic (from A^z to B^{z-1}) and anodic (from B^{z-1} to A^z) reactions respectively, $[A^z]_0$ and $[B^{z-1}]_0$ indicate the concentrations of A^z and B^{z-1} at the electrode surface.

For the electrochemical reactions of electrolysis, early studies have experimentally found that the current is often related exponentially to the applied overpotential η ($\eta = E - E_f^0$), while we know from the above equations (1.18) and (1.19) that the current is controlled by interfacial dynamics, indicating the dependence of the electrode kinetics on the potential

applied to the electrode. To establish their mathematic relationships, *transition state theory*[9, 10], an important general theory for electrode kinetics, is utilized. It states that reactions proceed through a transition state or activated complex. Figure 1.2 shows the reaction paths of equation (1.17) in terms of energy along a *reaction coordinate.* The standard Gibbs energy change (or energy barrier) from the reactants ($A^z + e^-$) to the transition state is $\Delta G_c^{\ddagger}$, whereas of that the transition state is above the products (B^{z-1}) by $\Delta G_a^{\ddagger}$.

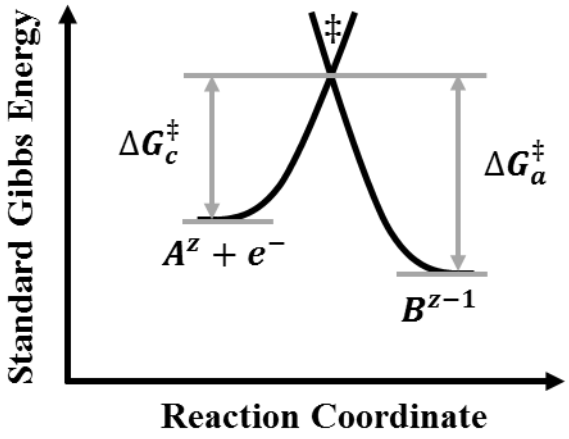

Figure 1.2: Standard Gibbs energy profiles during an electrochemical reaction.

As the electron is involved in the reaction as part of the reactants, the standard Gibbs energy of the reactants ($G^0(R)$) can be adjusted by different potentials ($\emptyset_M$) applied to the electrode. We know from Section 1.1 that

$$\boldsymbol{G^0(R) = c_1 + ZF\emptyset_S - F\emptyset_M} \qquad \textbf{(1.20)}$$

where c_1 is a constant. If the electrode potential is changed from its formal potential E_f^0 to E by ΔE, the electrode energy level is changed accordingly by $F\Delta E = -F(E - E_f^0)$. Thus the energy profile of $A^z + e^-$ moves up or down by that amount when a negative or positive ΔE is applied. Figure 1.3 shows the energy profile of $A^z + e^-$ altered by a positive potential difference ΔE. From Figure 1.3b we can clearly see that the energy barrier for B^{z-1} oxidation

decreases by a fraction of the total energy change. This fraction is called $1-\alpha$, where α is the transfer coefficient ranging from zero to unity. Thus,

$$\Delta G_a^{\ddagger} = \Delta G_{0,a}^{\ddagger} - (1-\alpha)F(E - E_f^0) \tag{1.21}$$

Brief analysis of Figure 1.3 further reveals that after shifting the potential more positively from E_f^0 the cathodic energy barrier (A^z reduction) increases by $\alpha F\left(E - E_f^0\right)$. Hence,

$$\Delta G_c^{\ddagger} = \Delta G_{0,c}^{\ddagger} + \alpha F(E - E_f^0) \tag{1.22}$$

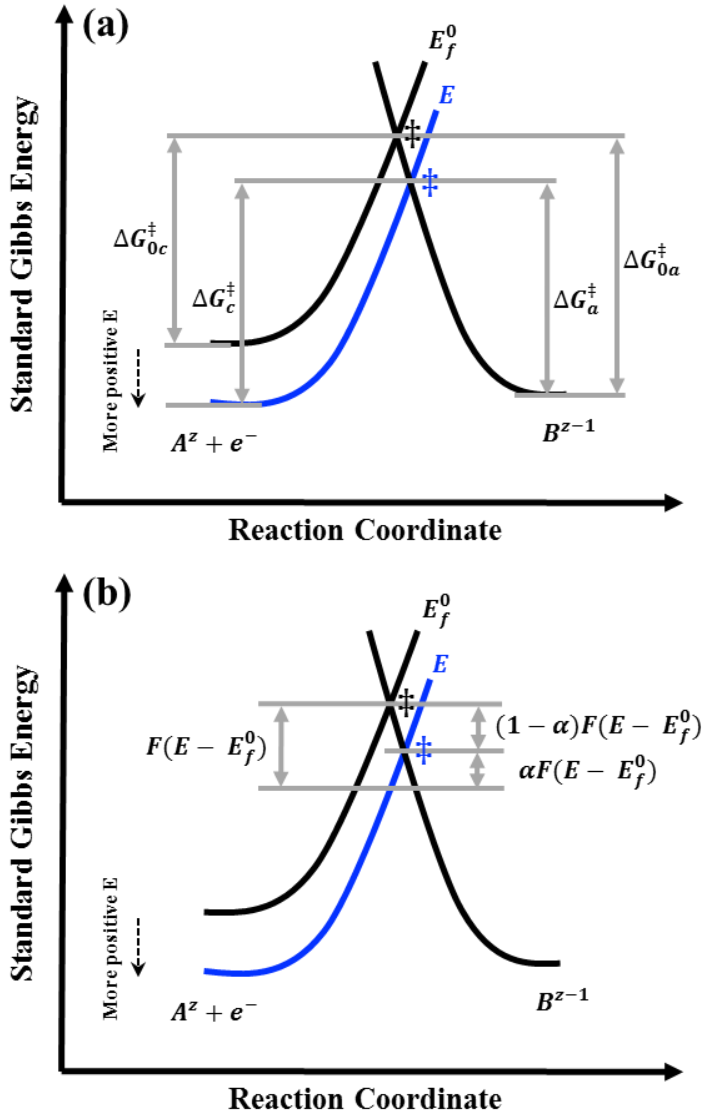

Figure 1.3: Effect of a more positive potential applied to the working electrode on the activation energy.

The rate constant of k_c and k_a in Arrhenius form can be expressed as

$$\boldsymbol{k_c} = \boldsymbol{A_c}\, \boldsymbol{e}^{\frac{-\Delta G_c^{\ddagger}}{RT}} \quad \text{and} \quad \boldsymbol{k_a} = \boldsymbol{A_a}\, \boldsymbol{e}^{\frac{-\Delta G_a^{\ddagger}}{RT}} \tag{1.23}$$

Inserting the expressions (1.21) and (1.22), gives

$$\boldsymbol{k_c} = \boldsymbol{A_c}\, \boldsymbol{e}^{\frac{-\Delta G_{0,c}^{\ddagger} - \alpha F(E - E_f^0)}{RT}} \quad \text{and} \quad \boldsymbol{k_a} = \boldsymbol{A_a}\, \boldsymbol{e}^{\frac{-\Delta G_{0,a}^{\ddagger} + (1-\alpha) F(E - E_f^0)}{RT}} \tag{1.24}$$

For the special case that the interface is at equilibrium with a solution in which $[A^z]_0 = [B^{z-1}]_0$, $E = E_f^0$ and no net current flows through the system,

$$\boldsymbol{J} = \boldsymbol{k_c}[\boldsymbol{A^z}]_{\boldsymbol{0}} - \boldsymbol{k_a}[\boldsymbol{B^{z-1}}]_{\boldsymbol{0}} = \boldsymbol{0} \tag{1.25}$$

Thus, $k_a = k_c = k^0 = A_c\, e^{\frac{-\Delta G_{0,c}^{\ddagger}}{RT}} = A_a\, e^{\frac{-\Delta G_{0,a}^{\ddagger}}{RT}}$. The quantity k^0 is the *standard electrochemical rate constant*. The rate constants at other potentials can then be expressed simply in terms of k^0:

$$\boldsymbol{k_c} = \boldsymbol{k^0}\, \boldsymbol{e}^{\frac{-\alpha F(E - E_f^0)}{RT}} \quad \text{and} \quad \boldsymbol{k_a} = \boldsymbol{k^0}\, \boldsymbol{e}^{\frac{(1-\alpha) F(E - E_f^0)}{RT}} \tag{1.26}$$

Assuming the value of α is 0.5, when the potential is changed by one Volt the rate constants k_a and k_c are changed by factors of *ca.* 10^9, indicating the overwhelming sensitivity of the electrochemical rate constant on the electrode potential. This sensitivity is central to the electrode kinetics.

Substitution of expression (1.26) into (1.19) and then (1.18) gives the following important *current-potential* relation:

$$\boldsymbol{I} = \boldsymbol{FAk^0}\, (\, [\boldsymbol{A^z}]_{\boldsymbol{0}}\, \boldsymbol{e}^{\frac{-\alpha F(E - E_f^0)}{RT}} - [\boldsymbol{B^{z-1}}]_{\boldsymbol{0}}\, \boldsymbol{e}^{\frac{(1-\alpha) F(E - E_f^0)}{RT}}\,) \tag{1.27}$$

This is the famous *Butler-Volmer equation*[11-13], from which the *Tafel Law* can be derived.

If the reduction process ($A^z + e^- \rightarrow B^{z-1}$) in reaction (1.17) is significantly faster than the backward reaction (oxidation), the oxidation term in equation (1.27) is negligible. The expression becomes

$$\boldsymbol{I_{red} = FAk^0[A^z]_0\, e^{\frac{-\alpha F(E-E_f^0)}{RT}}} \quad \textbf{(1.28)}$$

Similarly, when the oxidation process is significantly faster than the reduction process, it has

$$\boldsymbol{I_{ox} = FAk^0[B^{z-1}]_0\, e^{\frac{(1-\alpha)F(E-E_f^0)}{RT}}} \quad \textbf{(1.29)}$$

Taking natural logarithms of the above equations gives,

$$\boldsymbol{\alpha = -\frac{RT}{F}\frac{\partial ln|I_{red}|}{\partial E}} \quad \text{and} \quad \boldsymbol{1-\alpha=\beta=\frac{RT}{F}\frac{\partial ln|I_{ox}|}{\partial E}} \quad \textbf{(1.30)}$$

Plots of $ln|I_{red}|$ against E or $ln|I_{red}|$ against E are called *Tafel plots* where the gradient of this straight line is directly proportional to the transfer coefficient α or β respectively, as shown in Figure 1.4. Note that this procedure requires $[A^z]_0$ and $[B^{z-1}]_0$ to be constant over the range of the potentials studied.

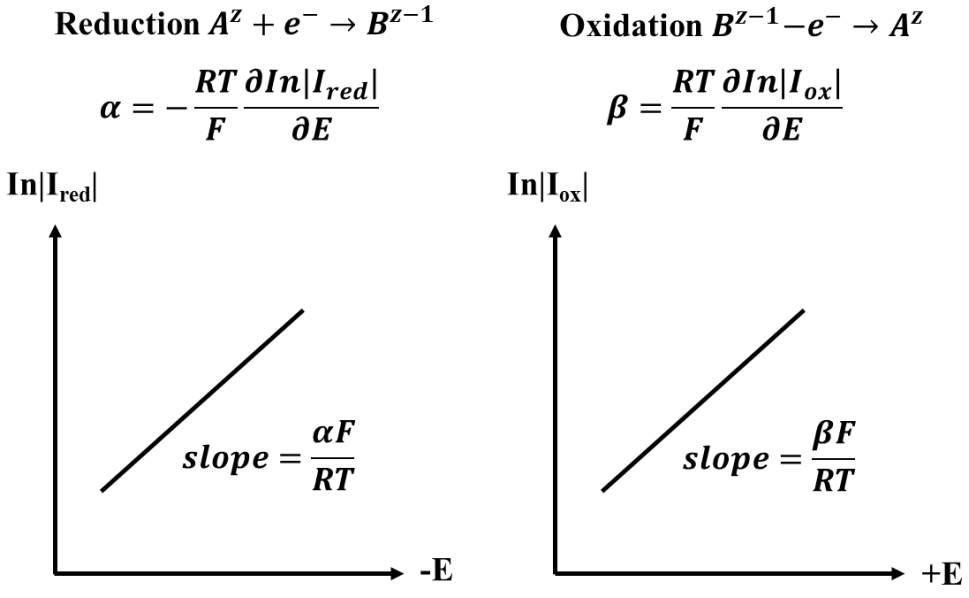

Figure 1.4: Tafel plots.

1.3 Electrochemical Cell

A typical electrochemical experiment is carried out using a three-electrode system[1, 14] (Figure 1.5). This comprises a working electrode (WE), a reference electrode (RE) and a counter electrode (CE). The working electrode is the electrochemical interface of interest. The use of reference electrode as mentioned in Section 1.1 is to enable the measurement and control of the potential of the working electrode when connecting to a voltmeter. Moreover, the passage of the current requires the use of a third electrode, the counter electrode. The current passes through the counter electrode, rather than the reference. Otherwise, the passage of the current would not only induce the chemical changes within the reference electrode hence altering the potential of the reference electrode to an unknown value, but cause a potential drop (IR) between the working electrode and reference electrode since the electrical resistance exists in the bulk solution, such that the working electrode potential would no longer be controlled.

$$\boldsymbol{E} = (\emptyset_{\boldsymbol{M}} - \emptyset_{\boldsymbol{S}})_{\boldsymbol{working}} + \boldsymbol{IR} - (\emptyset_{\boldsymbol{M}} - \emptyset_{\boldsymbol{S}})_{\boldsymbol{reference}} \quad \textbf{(1.31)}$$

Note that two-electrode (working and reference) system sometimes can be used when the working electrode is a microelectrode[15, 16] because only a very low current (~ 10^{-9} A) passes through it. The IR term is accordingly greatly minimized and can be neglected.

As shown in Figure 1.5 (right), all the electrodes are controlled by a 'potentiostat'. First, the potentiostat imposes a fixed potential, *E*, between the working electrode and the reference electrode, and only negligible current passes through the reference. The potential of the reference electrode keeps constant so that any changes in *E* are fully reflected as the changes in the potential of the working electrode. The potential changes on the working electrode will typically cause a current (*I*) to flow. This current is measured. The potentiostat then drives the counter electrode to whatever potential required to pass the same current as that flowing

through the working electrode.[1]

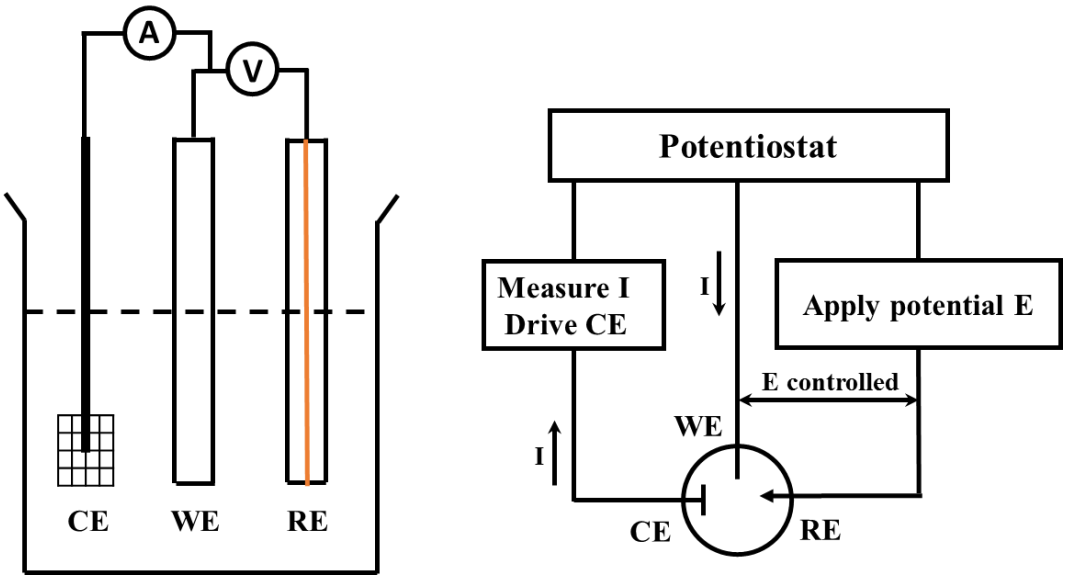

Figure 1.5: Schematic diagram of a three-electrode cell.

1.4 Mass Transport

In Section 1.2, we discussed electrode kinetics in respect to the electrode-solution interface by simply considering the rate of electron transfer of a given concentration of the species at the electrode surface. However, in practice, consumption of the reactants and formation of the products on the electrode surface leads to the movement of the reactants towards the electrode surface and of products away from the electrode surface. Thus the overall kinetics of any electrochemical reactions obviously not only depends on the rate of the electron transfer, but also the rate of the mass transport. If the electron transfer rate is fast, mass transport may limit the magnitude of current passed via the movement of reactant/product towards/away from the electrode. Three main processes contribute to the mass transport of electroactive species to an electrode: diffusion, migration and convection, which are introduced below sequentially.

Diffusion, as the dominant term of mass transport, is a phenomenon that a species spontaneously moves down its concentration gradient so as to maximize entropy. For a planar electrode in a solution containing the reactant, the bulk concentration of the reactant is constant. With a suitable potential applied to the electrode the reactant is consumed (either oxidized or reduced) at the electrode surface leading to a lower concentration of this species in the vicinity of the electrode. A concentration gradient is therefore induced between the electrode and bulk solution. Figure 1.6 shows the electrochemically created zone of depletion of the reactant near the electrode surface which is called a 'diffusion layer'.

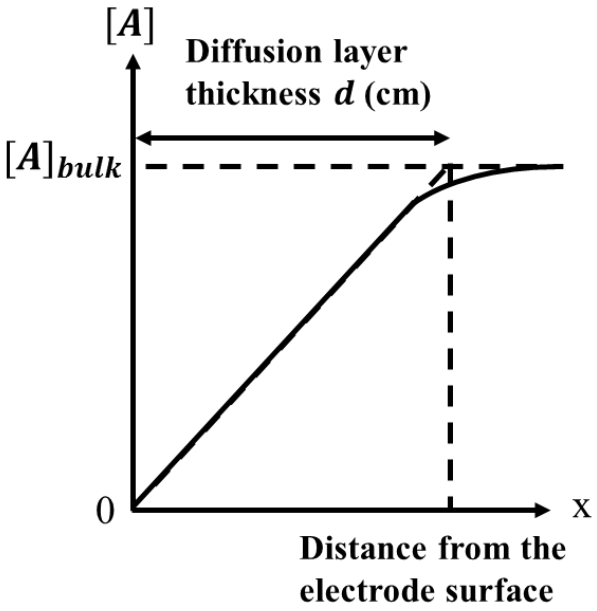

Figure 1.6: Nernst diffusion layer.

It is the created concentration gradient that drives the diffusion of the electroactive species from the bulk solution to the interface. *Fick's First Law*[17] describes the relation between the diffusive flux J (mol cm^{-2} s^{-1}) and the concentration gradient in one dimension,

$$J = -D\frac{\partial C}{\partial x} \tag{1.32}$$

where the flux J (mol cm^{-2} s^{-1}), as defined in the previous section, is the number of moles passing through a unit area in a unit time, D is the diffusion coefficient of the species (cm^2 s^{-1})

with a typical magnitude in the range $10^{-6} \sim 10^{-5}$ cm^2 s^{-1} and $\frac{\partial C}{\partial x}$ is the concentration gradient. The negative sign involved in *Fick's First Law* accounts for the species moving from an area of higher concentration to lower concentration.

Since the concentration of the species at a point x is changing with time, *Fick's Second Law* describes the rate of change in concentration at the point x,

$$\frac{\partial C}{\partial \mathrm{t}} = \boldsymbol{D}\ \frac{\partial^2 C}{\partial x^2} \tag{1.33}$$

Figure 1.7 shows the molecular basis of *Fick's Laws* in one dimension. Consider at any point x on an arbitrary concentration-distance profile, the movement of a molecule in a 'box' of $2\delta x$ in width. For each 'half box' of δx, a molecule has equal probabilities of moving to the right and to the left. The average time for the molecule moving a distance δx is δt. Hence the number of molecules travelling is $\frac{1}{2}C_1 A\delta x$ from left to right, and $\frac{1}{2}C_2 A\delta x$ from right to left. The net rate of transfer through a plane positioned at x is

$$\boldsymbol{rate} = \frac{(C_1 - C_2)A\delta x}{2\delta t} \tag{1.34}$$

The flux is expressed as

$$\boldsymbol{J} = \frac{(C_1 - C_2)\delta x}{2\delta t} \tag{1.35}$$

where the concentration gradient is

$$\frac{C_1 - C_2}{\delta x} \sim -\frac{\partial C}{\partial \mathrm{x}} \tag{1.36}$$

Substitution of equation (1.36) into (1.35) gives

$$\boldsymbol{J} = -\frac{(\delta x)^2}{2\delta t}\ \frac{\partial C}{\partial \mathrm{x}} \tag{1.37}$$

This is equivalent to *Fick's First Law* (equation 1.32) when

$$\boldsymbol{D = \frac{(\delta x)^2}{2\delta t}} \qquad \textbf{(1.38)}$$

Thus, for a molecule in solution, its diffusion coefficient, D, describes how far it travels in a certain time. The root mean square displacement in time, t, can be given as

$$\boldsymbol{\sqrt{\langle x^2 \rangle} = \sqrt{2Dt}} \qquad \textbf{(1.39)}$$

which gives a measure of the diffusion layer thickness, *d* (cm).[18, 19] When considering three-dimensional diffusion, the root mean square distance becomes

$$\boldsymbol{\sqrt{\langle x^2 \rangle + \langle y^2 \rangle + \langle z^2 \rangle} = \sqrt{6Dt}} \qquad \textbf{(1.40)}$$

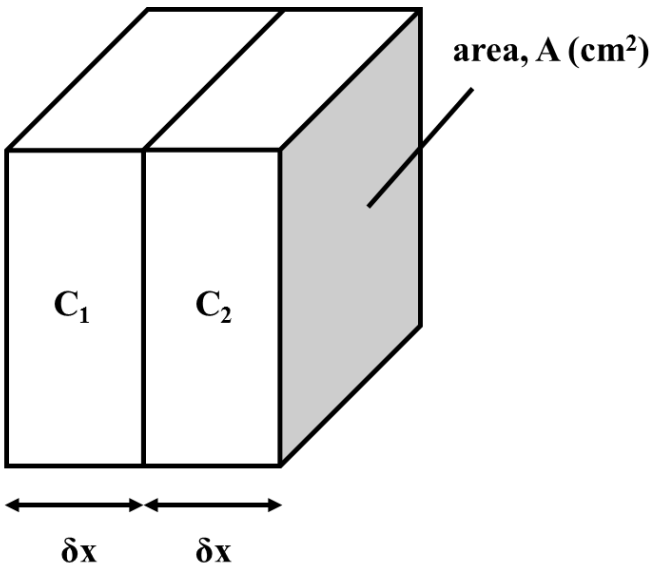

Figure 1.7: The molecular basis of *Fick's First Law* in one dimension.

Secondly, *Migration* describes the effect of an electrical field on the movement of the charged species in solution.[1, 5, 20] Concentration gradients are generally small in the bulk solution away from the electrode in which therefore the total current is carried mainly by migration. All charged species (no matter they are electroactive or not) contribute. For

species j in a bulk region of a linear electric field,

$$J_j = J_{m,j} = -\frac{Z_j F}{RT} D_j C_j \frac{\partial \emptyset}{\partial x} \quad (1.41)$$

where J_j and $J_{m,j}$ are the total flux and the migratory flux respectively (mol cm^{-2} s^{-1}), Z_j is the charge of the ion j, C_j is the concentration of the ion (mol cm^{-3}) and $\frac{\partial \emptyset}{\partial x}$ is the potential gradient (or electric field, V cm^{-1}).

Near the electrode, the total flux J_j of an electroactive substance which finally contributes to the current is a result of a mixed transport process of diffusion and migration. The diffusive and migrational components of the flux, expressed as $J_{d,j}$ and $J_{m,j}$, may be in the same or opposite directions, depending on the direction of the electric field and the charge (sign) on the electroactive species.[21] Figure 1.8 depicts situations when a positively charged (cation), a negatively charged (anion), and a neutral electroactive substance separately experience a reduction process. It is easy to understand that the migrational flux is in the same direction as the diffusive flux when cations are reduced at cathodes and anions oxidized at anodes, while it opposes the diffusive flux when anions react at cathodes and cations react at anodes.

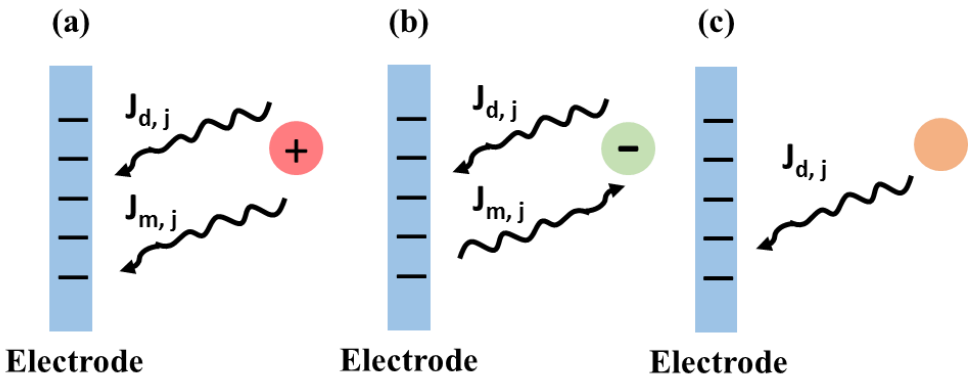

Figure 1.8: Reduction process with different directions of migratory flux. (a) Positively charged species. (b) Negatively charged species. (c) Uncharged species.

The above introduction indicates that migration can severely affect the current and make the experimental data complicate to analyze. To eliminate the effects of migration, a supporting electrolyte consisting of non-electroactive ions at a concentration much larger than that of the electroactive substances is added to compress the interfacial drop to being very close to the interface so that most of the electroactive ions can diffuse to the electrode surface to react. The migratory flux with the $\frac{\partial \phi}{\partial x}$ term eliminated is hence reduced to negligible levels. In addition to this function, the supporting electrolyte also serves to decrease the solution resistance, and hence the undesirable potential drop between the working and reference electrodes (Section 1.3), allowing the working electrode's potential to be controlled or measured more accurately. Improved solution conductivity also mitigates a requirement of high overpotential and hence simplifies the design of apparatus. Another benefit the supporting electrolyte can bring is its chemical contributions. It enables the better control of the reaction conditions through fixing the solution composition (e.g. pH, ionic strength or serving as buffer) that controls the reaction conditions. The excess supporting electrode also establishes a uniform ionic strength throughout the solution, even when ions are produced or consumed at the electrodes, allowing the activity of the redox couple to be kept consistent and facilitating the use of formal potentials (as discussed in Section 1.1).

Last but not least, the supporting electrolyte acts to compress the electrical double layer to be very thin with respect to the diffusion layer and compatible with electron tunneling distance (approximately 10-20 Å) for electrolyte concentrations of ca. 0.1 M or above.[6] This ensures the potential applied to the electrode can be mainly used for driving the electrochemical reaction sought to occur. Figure 1.9 shows a schematic diagram of the electrical double layer with (left) or without (right) anions specifically adsorbed, and the potential variation across the double layer in the absence of specific adsorption of ions. The electrical double layer is formed via the arrangement of the ions at the electrode/solution

interface. As shown in Figure 1.9, when the potential applied at the electrode is more positive than that in the solution, due to the electrostatic forces, anions and solvent molecules will migrate from solution and adsorb onto the electrode surface, forming a closest layer to the electrode. This is called Inner Helmholtz Plane (IHP). Outer Helmholtz Plane (OHP) is where the nearest solvated anions are located. These solvated anions are not specifically adsorbed to the electrode but interact with the charged electrode via only long-range electrostatic forces. Also depicted in Figure 1.9 is the diffuse layer consisting of both solvated anions and cations which extends from the OHP to the bulk solution. These layers consisting of the electrical double layer help to maintain electrical neutrality at the electrode/solution interface. The potential variation across these layers in Figure 1.9 shows that most of the potential drop, $\emptyset_M - \emptyset_S$, occurs within the compact *Helmholtz* layer. This potential drop is the driving force for electrochemical reaction to occur.

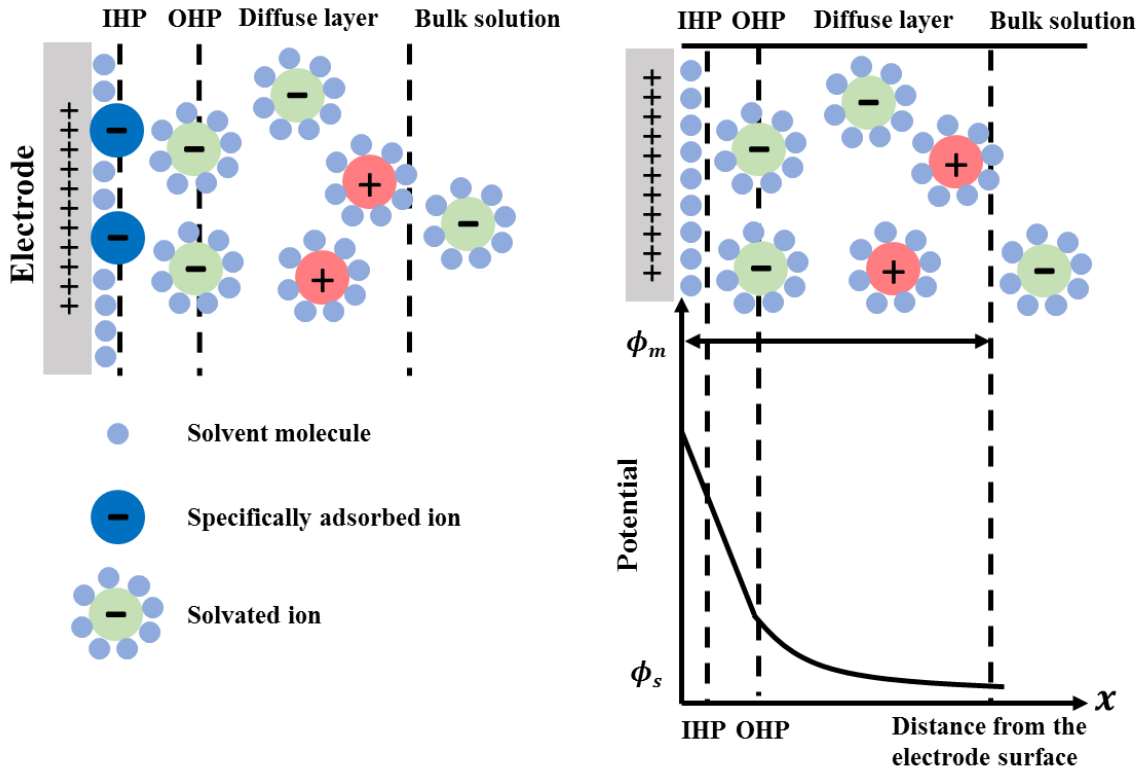

Figure 1.9: Proposed models of the double-layer region with (left) or without (right) anions specifically adsorbed. Bottom (right): potential profile across the double layer in the absence of specific adsorption of ions.

Finally, *Convection* refers to the movement of species due to a mechanical force and can be divided into two forms according to the origin of the force: natural convection and forced convection. Natural convection usually occurs when there are density or thermal gradients in the solution, Density differences can result directly from the chemical changes at the working and/or counter electrodes where electrolysis occurs when a potential is applied, or be caused by the thermal variations from, for example, strongly exothermic or endothermic coupled homogeneous chemical reactions, and the imperfect thermo-stating for large electrochemical cells. This form of convection is undesirable and can cause experimental irreproducibility. Forced convection usually arises from the deliberate mechanical agitation of the solution via stirring, gas bubbling or pumping. It is used to deliver fresh electroactive species to the electrode surface at a known rate. The effect of natural convection is eliminated, thus allowing well-defined quantitative analysis. Forced convection is commonly used in hydrodynamic studies (i.e. sonoelectrochemistry, rotating disc electrodes, or flow cells).[1, 5, 22] The flux due to convection, $J_{c,j}$ (mol cm^{-2} s^{-1}), can be expressed as:

$$\boldsymbol{J_{c,j} = C_j v'} \qquad \textbf{(1.42)}$$

where v' is the solution velocity (cm s^{-1}) and $\boldsymbol{C_j}$ is the concentration (mol cm^{-3}) of species *j*.

For fast electrode kinetics, mass transport controls the voltammogram. However, with the three different types of mass transport, it is difficult to determine the influence of each individual component. Therefore, in the experiments reported in this thesis, migration and convection are minimised to ensure a diffusional controlled response.

1.5 Electrochemical Techniques

This section is concerned with electrochemical methods in which the working electrode potential is controlled in a predetermined manner (either held constant or varied with time) as the current is measured as a function of time or potential. This technique contains the two most powerful experimental approaches to study electrochemistry: cyclic voltammetry and chronoamperometry.

1.5.1 Cyclic and Linear Sweep Voltammetry

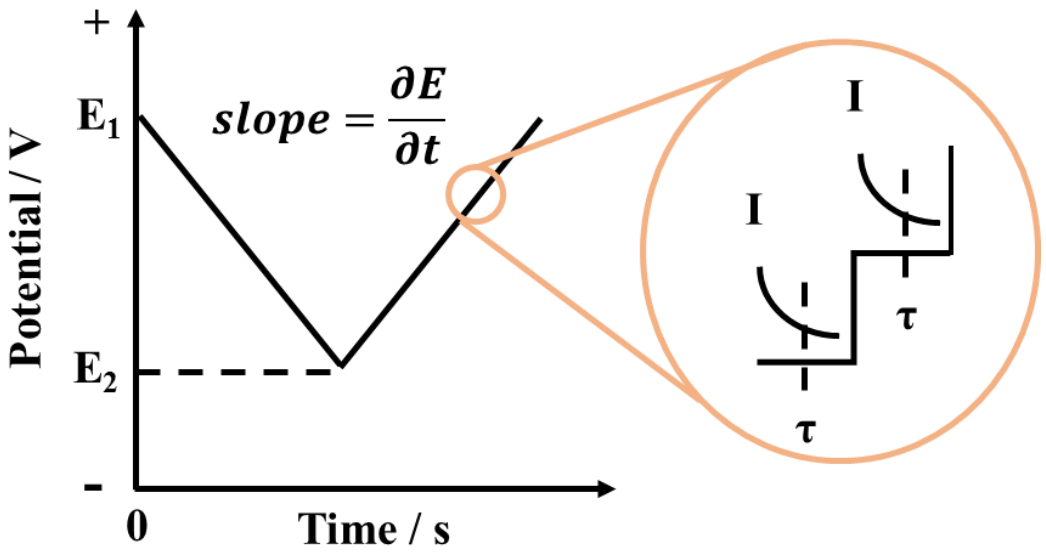

Figure 1.10: The potential-time profile of a cyclic voltammogram for a reduction. Zoom-in image shows the steps at each of which current is recorded at $t = \tau$.

As one of the most popular electrochemical methods, cyclic voltammetry (CV)[23-25] is conducted by linearly scanning the potential at the working electrode with a constant scan rate, v (V s^{-1}). The scan usually begins at a potential (E_1) where no *Faradaic* currents flow. The electrode potential is then linearly swept to a value, E_2, at which point the reaction is 'fully driven'. The direction of scan is then reversed and usually stops at the original value

(E_1). In practice, the 'linear' sweeping is actually performed with a large number of digitally generated small potential steps ('a staircase') as shown in Figure 1.10. The current, I, is simultaneously measured at one point of each potential step.[26] The plot of the resultant current against the sweeping potential is called a 'voltammogram'.

The shape of a voltammogram is determined by the rates of electron transfer and mass transport. The latter is not only related to the diffusion coefficient of the electroactive species but also the size-determined diffusion pattern involved at the specific working electrode. Linear diffusion occurs at a macro electrode (usually with dimensions of cm or mm) while convergent diffusion ('edge effects') at a micro electrode (at least one dimension of μm) (Figure 1.11a and Figure 1.11b). It is the relative magnitude of the electrode radius and diffusion layer thickness that determine the diffusion pattern. For macroelectrodes of radius much larger than the thickness of the diffusion layer ($r_e \gg d$), diffusion towards the electrode surface remains linear within the experimental time scale even though the thickness of the diffusion layer becomes progressively larger as the electrolysis proceeds. Equation (1.39) gives the expression for the diffusion layer thickness for one-dimension diffusive flux.

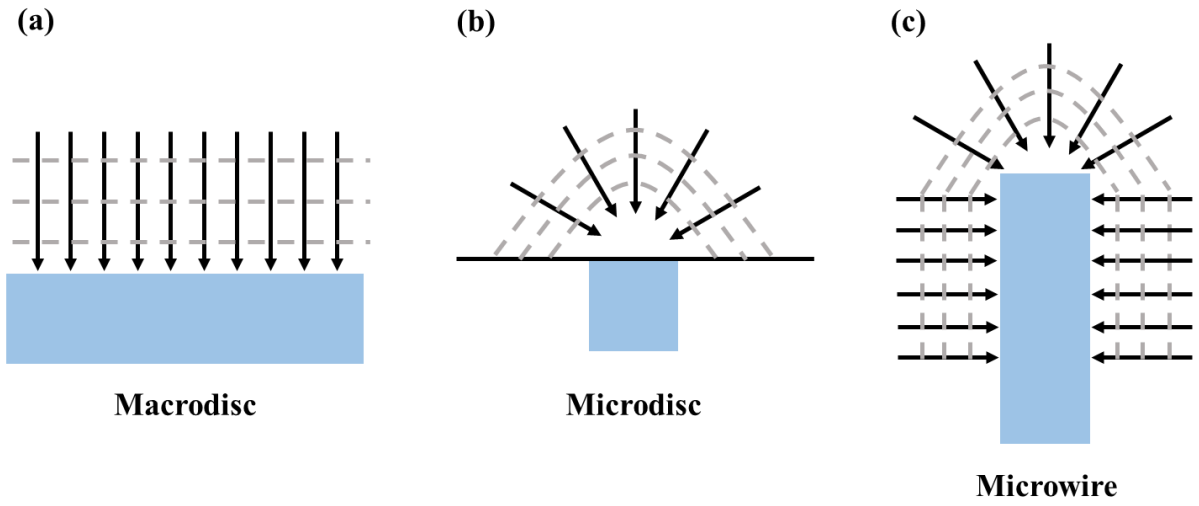

Figure 1.11: Diffusion at macrodisc (a), microdisc (b) and microwire (c) electrodes. Arrows: diffusion of electroactive species. Dashed line: the diffusion layers.

On the other hand, the much smaller size of microdisc electrodes compared to the thickness of the diffusion layer formed during electrolysis ($r_e \ll d$) results in the development of a hemispherical diffusion layer in which electroactive species move towards the electrode from all directions. This three-dimensional diffusive flux is much more efficient than the one-dimension at macroelectrodes. Thanks to the much higher rates of mass transport than seen at macroelectrodes, measurement of faster electron transfer process becomes achievable using microdisc electrodes.

Moreover, microwire electrodes are also commonly used because they not only have high mass transport rates as microdisc electrodes due to their micron-scale size, but also have a much larger surface area. The microwire electrode used in some of the experiments in this thesis is made from a cylindrical carbon fiber with a length of around 1 mm and a diameter around 7 μm. The fabrication procedure is given in Chapter 3. The high mass transport rate and surface area are favorable for electrochemical characterization of large solid particles such as the carbon nanotubes used in the experiments. As shown in Figure 1.11c, mass transport towards the cylindrical microelectrode includes linear diffusion at the side and convergent diffusion on the end.

Voltammetry of electrochemically reversible and irreversible processes at macroelectrodes and microelectrodes is next considered in the following paragraphs. Typical voltammograms for different levels of reversibility of the electrochemical process on a macrodisc electrode (Figure 1.12a) and a microdisc electrode (1.12b) are summarized in Figure 1.12. To study the voltammetry of the reduction of A, the potential is scanned from positive (E_1) to negative (E_2), then reversed to E_1. The curves 1~3 show the voltammograms with the increasing irreversibility. In Figure 1.12a, for macroelectrodes it can be observed that from the curves 1 to 3, the peak-to-peak separation of the forward (reductive) and back (oxidative) peak (ΔE_p) increases and both peak currents (I_p) decrease. In the case of microelectrodes, the curve in

Figure 1.12b is increasingly broadened from 1~3 with the half-wave potential moving more negatively. The half-wave potential, $E_{1/2}$ (V), is the potential where the current is half of the steady-state current ($I = \frac{I_{ss}}{2}$, A) The electrochemical processes (1~3) shown in Figure 1.12 can be referred as electrochemically "reversible", "quasi-reversible" and "irreversible", respectively.

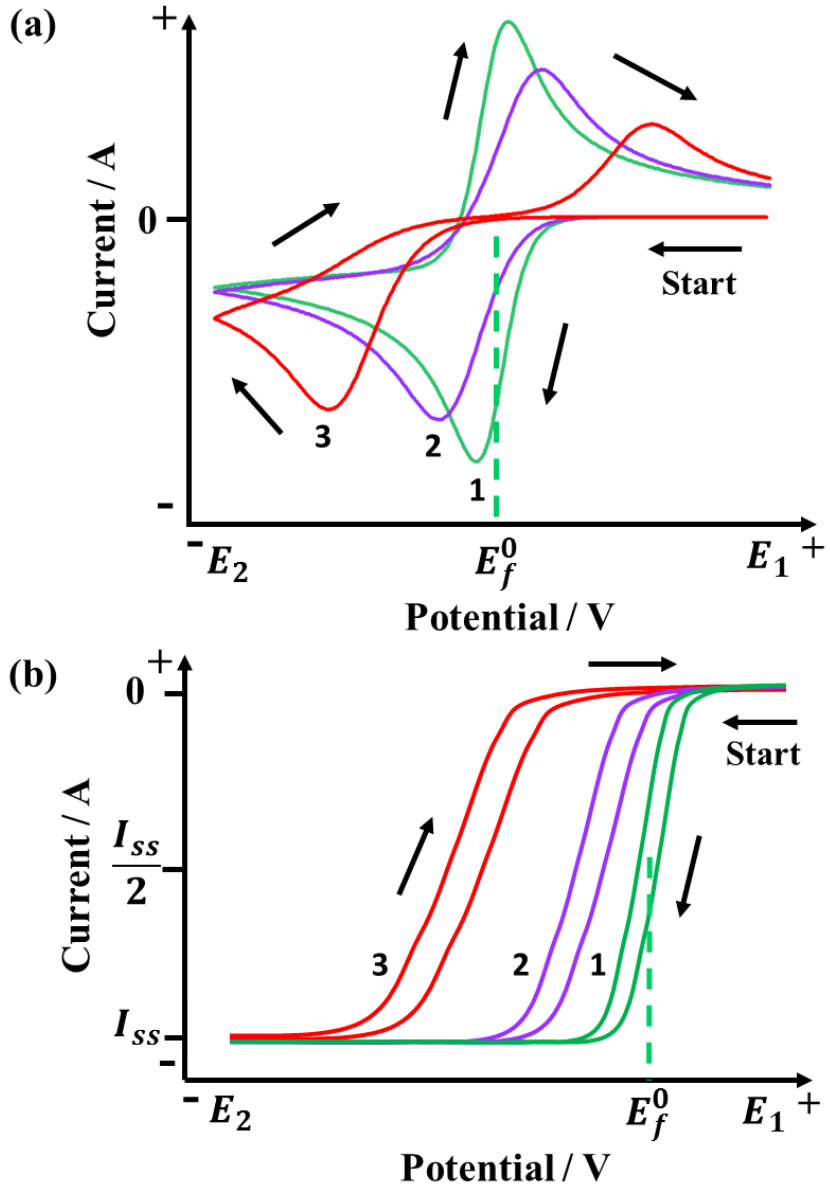

Figure 1.12: Reductive voltammetry of diffusive species at (a) macrodisc electrodes: peaked shaped responses, (b) microdisc electrodes: sigmoidal responses. Curve 1, 2 and 3 represent reversible, quasi-reversible, and irreversible systems respectively. Arrows show the starting point and scan direction.

1.5.1.1 Voltammetry at Macroelectrodes

The reversibility of a process at macroelectrodes can be quantified by comparing the standard electrochemical rate constant, k^0, with the mass transport coefficient, m_T (cm s^{-1}), where

$$\boldsymbol{m_T = \frac{D}{d}} \quad \textbf{(1.43)}$$

D is the diffusion coefficient of the species (cm^2 s^{-1}) and d is the diffusion layer thickness (cm). As equation (1.39) shows, $d = \sqrt{2Dt}$, where the experimental time t can be related to the scan rate as

$$\boldsymbol{t \sim \frac{RT}{Fv}} \quad \textbf{(1.44)}$$

so that m_T can be given as

$$\boldsymbol{m_T \sim \sqrt{\frac{DFv}{RT}}} \quad \textbf{(1.45)}$$

A rigorous mathematical evaluation for the limits of reversibility is given by the Matsuda and Ayabe parameter, Λ,[27] where:

$$\boldsymbol{\Lambda = \frac{k^0}{\sqrt{\frac{DFv}{RT}}}} \quad \textbf{(1.46)}$$

The following ranges for three different classifications at macroelectrodes are suggested:

Reversible

$$\boldsymbol{\Lambda \geq 15, \;\; k^0 \geq 0.3v^{0.5}} \textbf{ cm s}^{-1}$$

Quasi-reversible

$$\boldsymbol{15 > \Lambda > 10^{-3}, \; 0.3v^{0.5} > k^0 > 2 \times 10^{-5}v^{0.5}} \textbf{ cm s}^{-1}$$

Irreversible

$$\boldsymbol{\Lambda \leq 10^{-3},\ k^0 \leq 2 \times 10^{-5} v^{0.5}\ \text{cm s}^{-1}}$$

where T, D and α are assumed to be 298 K, 1×10^{-5} cm^2 s^{-1} and 0.5 respectively.

The shape of voltammograms in Figure 1.12a can be understood by considering the relative rates of electron transfer and mass transport. At the initial potential E_1 which is positive than the reduction potential of A, no current is observed. When the potential sweeps towards E_f^0, reductive current starts to flow. For an electrochemically reversible system (curve 1 in Figure1.12), the product is formed at the electrode surface, as predicted by the *Nernst Equation*. For an irreversible system (curve 3 in Figure 1.12), in this region the electron transfer rate is smaller than the rate of mass transport, thus the current, following *Butler-Volmer equation*, is a function of the reaction rate and the concentration of A. The further increase of the potential makes the current reaching a peak at which the electron transfer rate is balanced by the diffusion rate of A. As the potential continues to grow more negatively, the current decreases because the diffusion rate of A is not sufficient to replenish the material consumed at the electrode surface. When the potential scan is reversed, with the accumulated high concentration of B in the electrode's vicinity, the electrochemical balance at the surface grows more and more favorable toward the formation of A. Thus an anodic current from the oxidation of B flows and has a similar shape with the forward scan for essentially the same reasons.

Comparison of reversible and irreversible voltammetry for a one-electron transfer process at macroelectrodes can be summarized as below: First, when the value of peak-to-peak separation shown in the voltammogram, ΔE_p (V), is at about 57.4 mV at 298 K, the process is electrochemically reversible (Figure 1.12, curve 1). ΔE_p (V) in reversible voltammetry is independent with the potential scan rate, while for quasi- and irreversible system, ΔE_p (V)

becomes larger as the scan rate increases. Second, the mid-point potential of the forward and back peak, E_{mid} (V), can be expressed with the formal potential, E_f^0 (V), embedded.[1] For an reversible process,

$$\boldsymbol{E_{mid} = E_f^0 + \frac{RT}{2F}\ln\left(\frac{D_B}{D_A}\right)} \quad \textbf{(1.47)}$$

For an irreversible process, assuming $\alpha = \beta = 1/2$,

$$\boldsymbol{E_{mid} = E_f^0 + \frac{RT}{F}\ln\left(\frac{D_B}{D_A}\right)} \quad \textbf{(1.48)}$$

where

$$\boldsymbol{E_{mid} = \frac{E_{p,forward} + E_{p,reverse}}{2}} \quad \textbf{(1.49)}$$

$E_{mid} = E_f^0$ when the diffusion coefficients of A and B are equal (D_A=D_B). Therefore, no matter the process is reversible or not, the formal potential of the couple can be indicated by the mid-point potential, as shown in Figure 1.12a. Third, as described in the *Randles-Sevcik* equations, the peak current, I_p(A), for one electron transfer process at a macroelectrode is related to the bulk concentration of species A, $[A]_{bulk}$ (mol cm^{-3}), the scan rate, υ (V s^{-1}), the diffusion coefficient of species A, D_A (cm^2 s^{-1}) and the surface area of electrode, A_{elec} (cm^2). α is the transfer coefficient[1]

$$\boldsymbol{I_p = -0.446FA_{elec}[A]_{bulk}\sqrt{\frac{F\upsilon D}{RT}},\ \text{reversible}} \quad \textbf{(1.50)}$$

$$\boldsymbol{I_p = -0.496\sqrt{\alpha}FA_{elec}[A]_{bulk}\sqrt{\frac{F\upsilon D}{RT}},\ \text{irreversible}} \quad \textbf{(1.51)}$$

If there is specific adsorption for both the reactant and product on the electrode surface, a distinctive voltammetry compared to that of the diffusive species can be obtained. Figure

1.13 depicts an ideal votammetric wave of a surface-bound species undergoing a reversible process where symmetric forward and back peaks prevail and both of the two peak potentials are located at the formal potential of the redox couple. Due to the finite quantity of electroactive species adsorbed on the electrode surface, the current drops to zero after the peak. The current-potential wave-shape of the surface-bound species is only determined by the rate of electron transfer. In the case of slow electron transfer, the voltammetry is distorted with two asymmetric waves at either side of the formal potential as shown in Figure 1.13 (dashed line). The peak current I_p for reversible and irreversible processes of the surface-bound species is given as[28]

$$\boldsymbol{I_p = \frac{F^2}{4RT} v A_{elec} \Gamma_A^0, \ \text{reversible}} \tag{1.52}$$

$$\boldsymbol{I_p = \frac{\alpha F^2 v A_{elec} \Gamma_A^0}{2.718 RT}, \ \text{irreversible}} \tag{1.53}$$

where Γ_A^0 is the surface coverage of reactant at the electrode surface and other terms have been defined previously.

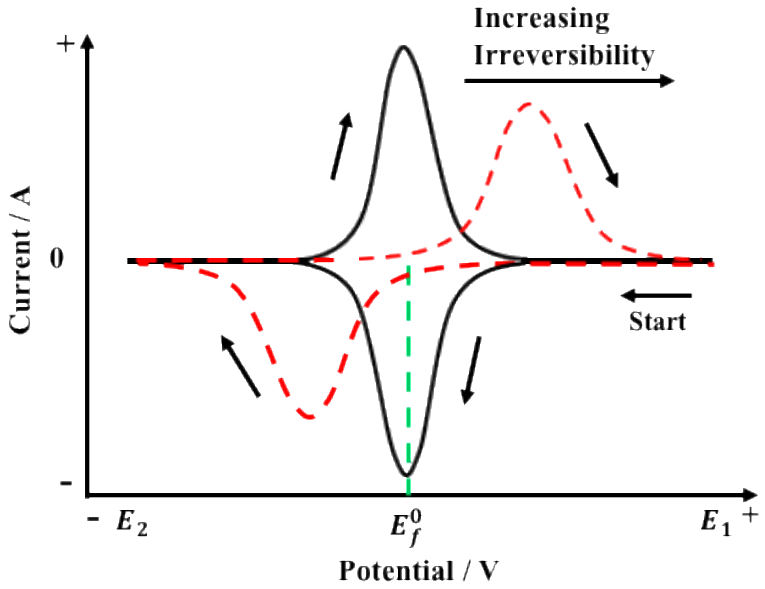

Figure 1.13: Reversible (solid) and irreversible (dashed) cyclic voltammetry profiles of surface bound species.

1.5.1.2 Voltammetry at Microelectrodes

Next, voltammetry at microdisc and microwire electrodes is introduced sequentially. Figure 1.12b shows three voltammograms at a microdisc electrode corresponding to three processes with the increasing irreversibility from curve 1 to 3. Similar to the above discussion on macroelectrodes, the boundaries of three kinetic regimes regarding the reversibility level are defined. A parameter κ_0 is used to quantify the transition with [5]

$$\boldsymbol{\kappa_0 = \frac{r_e k^0}{D_A}} \quad \textbf{(1.54)}$$

where r_e the radius of the electrode (cm), k^0 is the standard electrochemical rate constant (cm s^{-1}) and D_A is the diffusion coefficient (cm^2 s^{-1}). The following three kinetic regimes at microelectrodes are suggested:

Reversible

$$\boldsymbol{\kappa_0 > 10}$$

Quasi-reversible

$$\boldsymbol{10 \geq \kappa_0 \geq 10^{-2\alpha}}$$

Irreversible

$$\boldsymbol{\kappa_0 \leq 10^{-2\alpha}}$$

where α is the transfer coefficient.

In the voltammograms of a microelectrode (Figure 1.12b), when the potential scans from E_1 to E_f^0, the current response is approximately similar to that at a macroelectrode. However, a steady-state, instead of a peak, is reached when the potential sweeps more negatively to E_2. This is attributed to the more efficient convergent diffusion at microdisc electrodes. The diffusion of A is sufficient to compensate the depletion in the surface concentration of A, thus

a steady state is generated. Note that when very fast scan rates are applied the diffusion may transit from convergent to linear due to the short experimental time scale, leading to a wave shape change from a steady state to a peak.

Quantification of the voltammograms at microdisc electrodes gives the half-wave potential $E_{1/2}$ (V) expression with the formal potential, E_f^0 (V), embedded[5]

$$\boldsymbol{E_{1/2} = E_f^0 + \frac{RT}{2F}\ln\left(\frac{D_B}{D_A}\right),\ \text{reversible}} \quad \textbf{(1.55)}$$

$$\boldsymbol{E_{1/2} = E_f^0 + \frac{RT}{\alpha F}\ln\left(\frac{r_e k^0}{D_A}\right),\ \text{irreversible}} \quad \textbf{(1.56)}$$

$E_{1/2}$ is as defined before namely the potential where the current is half of the steady-state current. For a reversible process, $E_{1/2} = E_f^0$ when $D_A = D_B$, as shown in Figure 1.12. While for the irreversible process the $E_{1/2}$ of the couple is dependent on the electrochemical rate constant thus not shown in Figure 1.12. The steady-state current at a microdisc electrode, I_{ss} (A), can be expressed by the equation:

$$\boldsymbol{I_{ss} = 4nFD[A]_{bulk}r_e} \quad \textbf{(1.57)}$$

where the terms have been defined previously.

For voltammetry at microwire electrodes, the peak current, I_p (A), can be predicted via the equation[29, 30]

$$\boldsymbol{I_p = 2\pi nFD[A]_{bulk}l(0.446p + 0.335p^{0.15})} \quad \textbf{(1.58)}$$

$$\textbf{with } \boldsymbol{p = \sqrt{\frac{nFr_e^2 v}{RTD}}} \quad \textbf{(1.59)}$$

where l is length of the electrode (cm) and the rest of the terms have been defined previously. The diffusion at microwire electrodes, as shown in Figure 1.11c, is a combination of linear

and convergent diffusion. Correspondingly, the first term in equation (1.58) relates to linear diffusion towards the side of the electrode, while the second term corresponds to the convergent diffusion occurring at the end of the electrode.

In this section, the cyclic voltammetry technique has been introduced and the influence of the reversibility, diffusion and adsorption on the voltammogram discussed. In next section, we move on to briefly explore the method of chronoamperometry.

1.5.2 Chronoamperometry

Chronoamperometry is another popular electrochemical technique. It records the current with time as the potential applied at the working electrode is stepped instantaneously from a starting potential E_1 where usually no electrolysis takes place to a second potential E_2 at which electrolysis of interest occurs. As shown in Figure 1.14, a huge current flows at the start of the chronoamperogram and the current decreases with time due to the continuous consumption of the reactants near the electrode surface. The shape of the chronoamperomogram depends on the diffusion type towards the electrode during the electrolysis. Hence chronoamperometry at different electrodes (macrodisc, microdisc and microwire) is discussed sequentially.

In the case of a macroelectrode where the reactant is solely arriving at the electrode surface via linear diffusion, the *Cottrell equation* is used to describe the current response as a function of time when a sufficient potential is applied

$$\boldsymbol{I = \frac{nFA_{elec}\sqrt{D}[A]_{bulk}}{\sqrt{\pi t}}} \qquad \textbf{(1.60)}$$

where I is the net current (A), F is the Faraday constant (96485 C mol^{-1}), n is the number of electrons transferred, A_{elec} is the electrode area (cm^2), D is the diffusion coefficient (cm^2 s^{-1}), $[A]_{bulk}$ is the bulk concentration (mol cm^{-3}) and t is the time (s). According to the equation

(1.60), I becomes zero when t is infinite. This is because the inefficient diffusion cannot replenish the reactant in time making that all the reactants near the electrode are consumed.

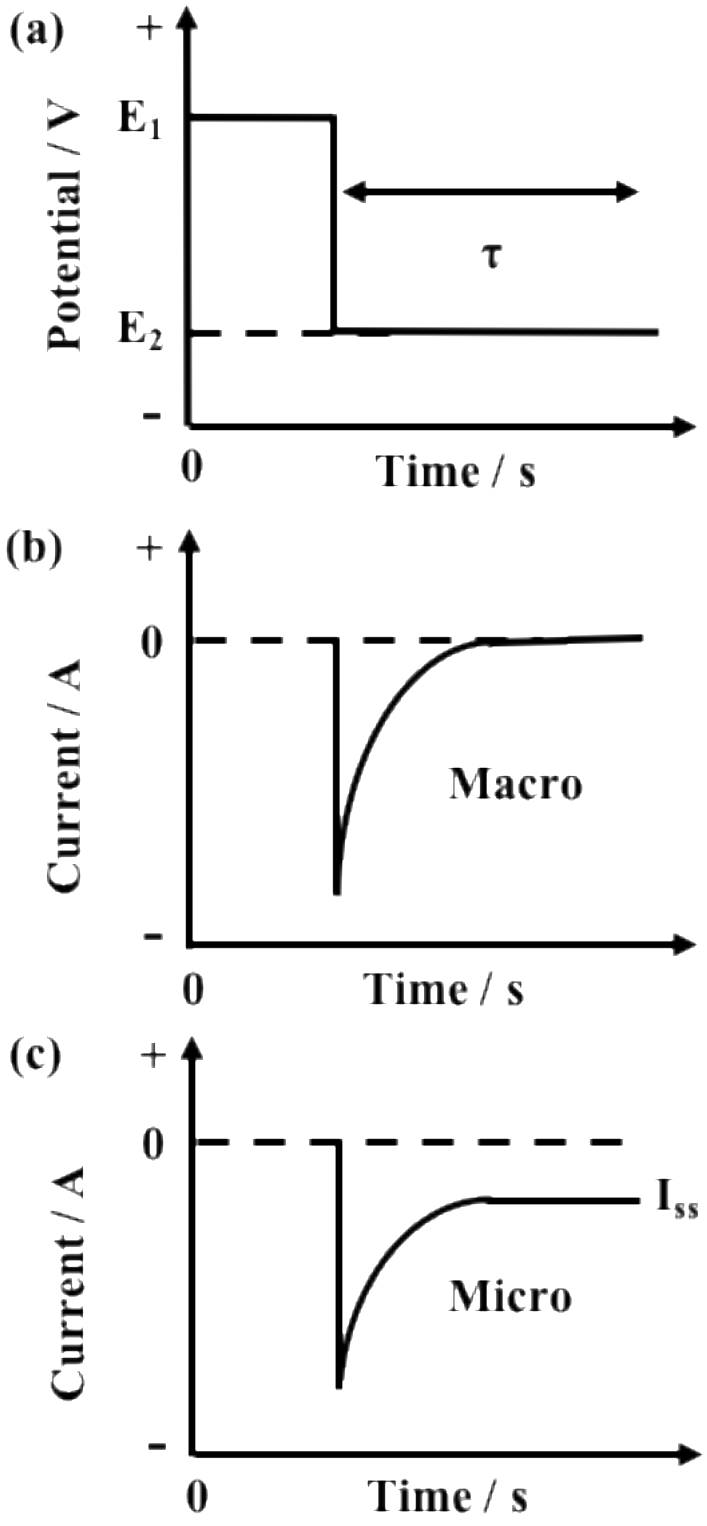

Figure 1.14: (a) The potential-time profile for a single step chronoamperometry experiment. The resulting chronoamperometric response at macroelectrodes (b) and at microelectrodes(c).

For a microdisc electrode at which the convergent diffusion takes place, the current decay can be determined by the *Shoup and Szabo Equation*:[31]

$$\boldsymbol{I = 4nFD[A]_{bulk} r_e f(\tau)} \quad \textbf{(1.61)}$$

$$\textbf{with} \quad \boldsymbol{f(\tau) = 0.7854 + 0.8862\tau^{-0.5} + 0.2146\, e^{-0.7823\tau^{-0.5}}} \quad \textbf{(1.62)}$$

where the dimensionless time parameter, τ, is expressed as

$$\boldsymbol{\tau = \frac{4Dt}{r_e^2}} \quad \textbf{(1.63)}$$

At long experimental times, steady state current, I_{ss}, is recorded and has an expression as equation (1.57).

The current transient at a microwire electrode with the linear diffusion at the side and convergent diffusion at the end was provided by Szabo et al.:[32]

$$\boldsymbol{I = 2\pi nFD[A]_{bulk} l f(\tau)} \quad \textbf{(1.64)}$$

$$\textbf{with} \quad \boldsymbol{f(\tau) = \frac{2e^{-\sqrt{\pi\tau}/20}}{\sqrt{\pi\tau}} + \frac{1}{\ln(\sqrt{e^{-\theta\tau}} + e^{5/3})}} \quad \textbf{(1.65)}$$

where l is the length of the wire electrode (cm), θ equals 0.5772156 and is a constant derived from the limits of the Bessel functions in the full formula for $f(\tau)$ and τ has been defined by equation (1.63).

Equation (1.64) reduces to *Cottrell Equation* at short times, while at long times, τ becomes large and hence its 'ln' term dominates, equation (1.64) becomes

$$\boldsymbol{I_{qss} = \frac{4\pi nFD[A]_{bulk} l}{\ln \tau}} \quad \textbf{(1.66)}$$

Due to the micro scale dimension of the electrode length, a mix of linear and convergent diffusion takes place at the microwire electrode, leading to only a quasi-steady state current at long times, the values of which can be predicted by equation (1.66).

References

[1] R. G. Compton and C. E. Banks, *Understanding Voltammetry, 2nd edn.*, Imperial College Press, London, **2011**.

[2] P. H. Rieger, *Electrochemistry, 2nd edn.*, Springer Netherlands, New York, London, **1994**.

[3] L. R. Faulkner, *J. Chem. Educ.*, **1983**, *60*, 262.

[4] J. R. Runo and D. G. Peters, *J. Chem. Educ.*, **1993**, *70*, 708.

[5] A. J. Bard and L. R. Faulkner, *Electrochemical Methods: Fundamentals and Applications*, Wiley, **2000**.

[6] S. Tadayoshi and A. Masashi, *Bull. Chem. Soc. Jpn.*, **2013**, *86*, 1158-1173.

[7] F. C. Strong, *J. Chem. Educ.*, **1961**, *38*, 98.

[8] R. G. Ehl and A. J. Ihde, *J. Chem. Educ.*, **1954**, *31*, 226.

[9] D. G. Truhlar, W. L. Hase and J. T. Hynes, *J. Phys. Chem.*, **1983**, *87*, 2664-2682.

[10] D. G. Truhlar, B. C. Garrett and S. J. Klippenstein, *J. Phys. Chem.*, **1996**, *100*, 12771-12800.

[11] J. A. V. Butler, *Trans. Faraday Soc.*, **1924**, *19*, 659-665.

[12] J. A. V. Butler, *Trans. Faraday Soc.*, **1924**, *19*, 729-733.

[13] J. A. V. Butler, *Trans. Faraday Soc.*, **1924**, *19*, 734-739.

[14] W. D. Ellis, *J. Chem. Educ.*, **1973**, *50*, A131.

[15] E. I. Rogers, D. S. Silvester, D. L. Poole, L. Aldous, C. Hardacre and R. G. Compton, *J. Phys. Chem. C*, **2008**, *112*, 2729-2735.

[16] M. Fleischmann, F. Lasserre, J. Robinson and D. Swan, *J. Electroanal. Chem. Interfacial Electrochem.*, **1984**, *177*, 97-114.

[17] A. Fick, *Annalen der Physik*, **1855**, *170*, 59-86.

[18] M. von Smoluchowski, *Annalen der Physik*, **1906**, *326*, 756-780.

[19] A. Einstein, *Annalen der Physik*, **1905**, *322*, 549-560.

[20] S. R. Belding, J. G. Limon-Petersen, E. J. F. Dickinson and R. G. Compton, *Angew. Chem. Int. Ed.*, **2010**, *49*, 9242-9245.

[21] D. Pletcher, *A First Course in Electrode Processes*, Royal Society of Chemistry, **2009**.

[22] M. I. Q. o. Montenegro, M.A.; Daschbach, J. L., *Microelectrodes: Theory and Applications:*, Springer Netherlands, **1991**.

[23] G. A. Mabbott, *J. Chem. Educ.*, **1983**, *60*, 697.

[24] J. J. Van Benschoten, J. Y. Lewis, W. R. Heineman, D. A. Roston and P. T. Kissinger, *J. Chem. Educ.*, **1983**, *60*, 772.

[25] P. T. Kissinger and W. R. Heineman, *J. Chem. Educ.*, **1983**, *60*, 702.

[26] A. S. Barnes, I. Streeter and R. G. Compton, *J. Electroanal. Chem.*, **2008**, *623*, 129-133.

[27] H. Matsuda and Y. Ayabe, *Zeitschrift für Elektrochemie, Berichte der Bunsengesellschaft für physikalische Chemie*, **1955**, *59*, 494-503.

[28] R. G. B.-M. Compton, C.; Dickinson, E. J. F., *Understanding Voltammetry - Problems and Solutions*, Imperial College Press, **2012**.

[29] J. Ellison, K. Tschulik, E. J. E. Stuart, K. Jurkschat, D. Omanović, M. Uhlemann, A. Crossley and R. G. Compton, *ChemistryOpen*, **2013**, *2*, 69-75.

[30] K. Aoki, K. Honda, K. Tokuda and H. Matsuda, *J. Electroanal. Chem. Interfacial Electrochem.*, **1985**, *182*, 267-279.

[31] D. Shoup and A. Szabo, *J. Electroanal. Chem. Interfacial Electrochem.*, **1982**, *140*, 237-245.

[32] A. Szabo, D. K. Cope, D. E. Tallman, P. M. Kovach and R. M. Wightman, *J. Electroanal. Chem. Interfacial Electrochem.*, **1987**, *217*, 417-423.

Chapter 2

Single Nanoparticle Electrochemistry

The development of methods for studying matter at the nanoscale or over dimensions approaching those of individual molecules has brought a myriad of new fundamental insights and experimental capabilities. In the field of electrochemistry, the methodology development for studying nanomaterials has an impact on not only electrochemical energy and sensing technologies, but also fundamental electrochemistry.

In last chapter, we introduced some of the basic concepts and theories of electrochemistry, much of which is based on mean-field descriptions of average fluxes and reaction rates. Macroscopic (ensemble) measurements are still predominantly used to infer the underlying microscopic processes particularly those associated with nanomaterials. However, this is not always straightforward or fully representative. A greater mechanistic understanding of the electrochemical reactivity of nanomaterials requires the development of method for probing electron transfer events on single particle redox nanomaterials and individual catalytic entities. One of these emerging methods is the 'nano-impact' approach which is built directly upon the conventional electrochemical method of amperometry. This chapter provides a brief introduction to both the nanomaterials and the 'nano-impact' method used in the experiments reported in the following chapters.

2.1 Nanomaterials

Nanoparticles, according to the guidelines of IUPAC (International Union of Pure and Applied Chemistry),[1] refer to a special class of material of any shape but with at least one

dimension between 1 to 100 nm. They have received a tremendous amount of attention in recent decades due to their structure-dependent properties which can deviate significantly from those of bulk materials. Taking the optical properties as an example, for some metal nanoparticles, fluorescence develops at a size smaller than ~ 2 nm because, at this size, the interaction of the low number of orbitals makes the energy levels no longer continuous as in a bulk metal and become more distinct.[2] For nanoscale semiconductor materials, also known as quantum dots, fluorescence may even arise at sizes greater than 2 nm due to their special electronic structure. Their optoelectronic properties are strongly dependent on both size and shape. The highly tuneable properties make quantum dots of wide interest.[3] Moreover, the physical properties of the particles also change significantly at the nanoscale. The particles with a small size have a much higher percentage of surface atoms. For example, the surface atoms account for about 80% for a palladium nanoparticle of 1 nm diameter.[4] It provides more catalytic sites for reactions and hence highly boosts its catalytic efficiency. In the following paragraphs, we will specifically introduce metal nanoparticles and carbon nanomaterials and their applications in electrochemistry since they are involved in the experiments reported in this thesis.

Metal nanoparticles (NPs) find a wide range of applications in electrocatalysis, electrochemical sensing and fundamental electron transfer studies because of their large surface-volume ratio, high density of active sites, and remarkable physicochemical properties.[5] In particular, significant attention has been given to the electrocatalysis of metal nanoparticles due to their excellent performance in the area of energy conversion and storage. For example, from a vast body of systematic studies, platinum (Pt), of the pure metals, is acknowledged to have the highest electrocatalytic activity towards the hydrogen oxidation reaction (HOR).[6, 7] Major interest in the latter has emerged because of its role as

the anode reaction of hydrogen fuel cells, where its fast kinetics spare the necessity of a high overpotential to obtain reasonable current densities.[8]

The oxidation of hydrogen is represented by the overall reaction:

$$\boldsymbol{H_2\,(aq) - 2e^- \rightarrow 2H^+\,(aq)} \qquad \textbf{(2.1)}$$

Pt provides an optimal balance in energy required for the dissociative adsorption of H_2, the formation of H^*_{ads} followed by a fast charge-transfer step and the desorption of protons. The mechanism is shown below which consists of three steps. [9-11]

$$\boldsymbol{H_2(aq) \rightarrow 2H^*_{ads}} \qquad \textbf{(Tafel)} \qquad \textbf{(2.2)}$$

$$\boldsymbol{H^*_{ads} \rightarrow H^+(aq) + e^-} \qquad \textbf{(Volmer)} \qquad \textbf{(2.3)}$$

$$\boldsymbol{H_2(aq) \rightarrow H^*_{ads} + H^+(aq) + e^-} \qquad \textbf{(Heyrovsky)} \qquad \textbf{(2.4)}$$

In the electrochemical experiments, when low overpotentials ($E - E_f^0 < 50$ mV) are applied at platinum, the Tafel-Volmer pathway applies. The first step (equation 2.2), called Tafel step, is a rate-determining dissociative adsorption of the dissolved hydrogen molecule from the solution onto two adjacent surface sites. A fast second step is the oxidative dissociation of the adsorbed hydrogen atom (H^*_{ads}) to produce a solvated proton, known as the Volmer step. At higher overpotentials, the Heyrovsky step, a combined adsorption and oxidation replaces the Tafel step as the rate-determining step.[12-14]

The development of catalysts for the HOR, hydrogen evolution reaction (HER) and oxygen reduction reaction (ORR) has been closely tied to the concept of the volcano plot, which generally expresses the rate of an electrocatalytic reaction as a function of more fundamental properties of the catalyst.[15, 16] With a few exceptions, close relationships between the Gibbs energy of intermediate adsorption (e.g. H^*_{ads} for HOR and HER) on the

catalyst surface and the kinetics have been found for reactions in acid media. The volcano plot for HER in acid solutions is shown in Figure 2.1. Note that the same activity trend is assumed for the HOR due to its reversibility.

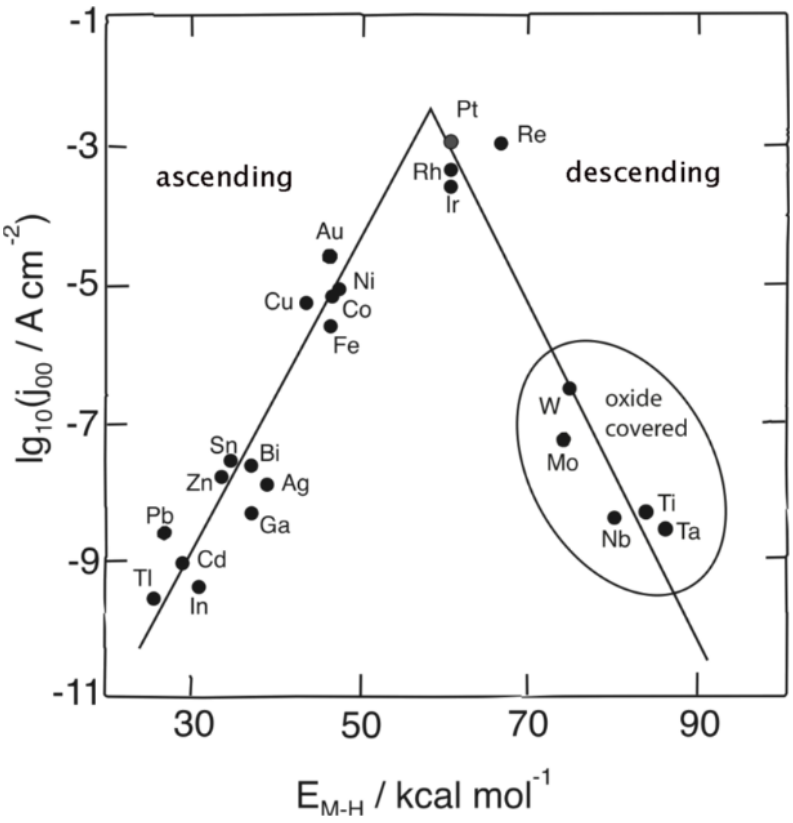

Figure 2.1: Trassati's volcano plot for the hydrogen evolution reaction (HER) in acid solutions. j_{00} denotes the exchange current density, and E_{M-H} represents the energy of hydride formation. Adapted from Ref. [17]. Copyright 2014, Beilstein-Institute. Original Figure in Ref. [18], Copyright 1972, Elsevier.

Although Pt shows the best catalytic performance and the use of its nanoparticles, to some extent, mitigates its high cost as a noble metal due to the improved efficiency, it has shortcomings including its scarcity and susceptibility to CO poisoning from trace impurities in the hydrogen fuel which greatly hinders its activity. This have prompted research into palladium (Pd) as an alternative anode material.[14] Despite a relatively low activity compared to Pt, Pd-based materials show a much lower poisoning from adsorbed impurities or intermediates, making them not only alternative catalysts for the HOR (and HER) but also

even better catalytic materials for methanol and formic acid oxidation in their relative fuel cells. [19-21] Moreover, its drawbacks in terms of activity can be mitigated by forming nanostructures which, as described above, create much more active sites for the reaction hence improving the catalytic efficiency.[14]

On the other hand, carbon materials are tremendously important as electrode materials in both fundamental and applied electrochemistry.[22] With the advent of new forms of carbon nanomaterials, particularly, carbon nanotubes (CNTs) and graphene, carbon electrode materials have taken on even greater significance for electrochemical studies, both in their own right and as components and supports in an array of functional composites.[23-26] Taking CNTs as an example, their special physical properties and morphology make them extremely attractive as optimal templates for the deposition of metal nanoparticles to form nano-composites. Metal nanoparticles (Pt, Pd, Ru, Au, Ag, Cu, Fe, alloys and metal oxides etc.) decorated CNTs have been developed for electrochemical (bio)sensing[27, 28], hydrogen storage and highly efficient catalysis,[29-34] particularly hydrogen and methanol oxidation, or oxygen reduction catalysis for fuel cell and battery technologies. In the rest of this thesis, we mainly report investigations on the catalytic performance of palladium nanoparticle decorated carbon nanotubes (CNT-Pds) towards various essential reactions in the energy storage applications such as the proton reduction with the formation of H_{UPD} (Chapter 3), the hydrogen oxidation reaction (Chapter 4), the oxygen reduction reaction (Chapter 5), and the methanol oxidation and formate oxidation reactions (Chapter 7). The method used in the experiments will be introduced in the next section.

2.2 Nano-impacts

The relation between the design and synthesis of nanoparticles and their electrocatalytic properties is receiving much scrutinization. Most published electrochemical studies have

involved ensemble measurement where the effect of size and morphology on the catalysis is averaged over a large population of nanoparticles. This, however, may be affected by polydispersity, different particle orientations, the formation of the likely agglomerated and irregular 'mat' associated with the dropcast technique and other phenomena that make it difficult to interpret. Electrochemical experiments at the level of a single NP can not only help clarify the structure-activity relationships, but also give an understanding of the link between the properties of individual particles and those of their ensembles. Methods for examining individual nanoparticles are therefore highly desirable.

The technique of electrochemical particle impacts (or 'nano-impacts') has quickly grown into a popular electroanalytical technique in recent years as it provides a simple but efficient and reliable way to characterise individual nanoparticles and probe their activities. This technique involves the detection of enhanced current signals from large numbers of individual nanoparticles randomly colliding on a microelectrode. A similar procedure was originally described by Lemay and co-workers in which nanoparticle collisions were detected via inhibition of the current due to the oxidation or reduction of a solute molecule.[35] Recent developments on the particle impacts were covered in several literature reviews.[36-40]

Specifically, the nano-impact experiment can be performed by recording the current change caused by oxidation or reduction of single nanoparticles when they randomly collide, by virtue of their Brownian motion, with a potentiostated electrode which is immersed in their suspension.[41-49] Due to the continuous consumption of the impacting nanomaterials during the measurement, the signals appear as current spikes (Figure 2.2a). In addition, as an alternative to the direct redox reaction of the nanoparticles themselves, mediated (indirect) electron transfer can also take place on the surface of impacting nanoparticles. When catalytically active nanoparticles stochastically collide with an inert microelectrode in a solution of redox molecules, transient current increases may be observed due to enhanced

catalytic activity on nanoparticle surfaces.[37, 50-54] The current response of these collisions may adopt one of two general forms: a current spike or a current step, as shown in Figure 2.2b and Figure 2.2c respectively. This is dependent on the residence time of the impacting catalytic nanoparticles on the electrode surface. If the nanoparticle desorbs or deactivates very fast on the experimental time scale, a current spike response appears in the chronoamperometric curve. If the nanoparticle desorption or deactivation is relatively slow compared to the experimental time, a 'step on' in the current-time response is observed.

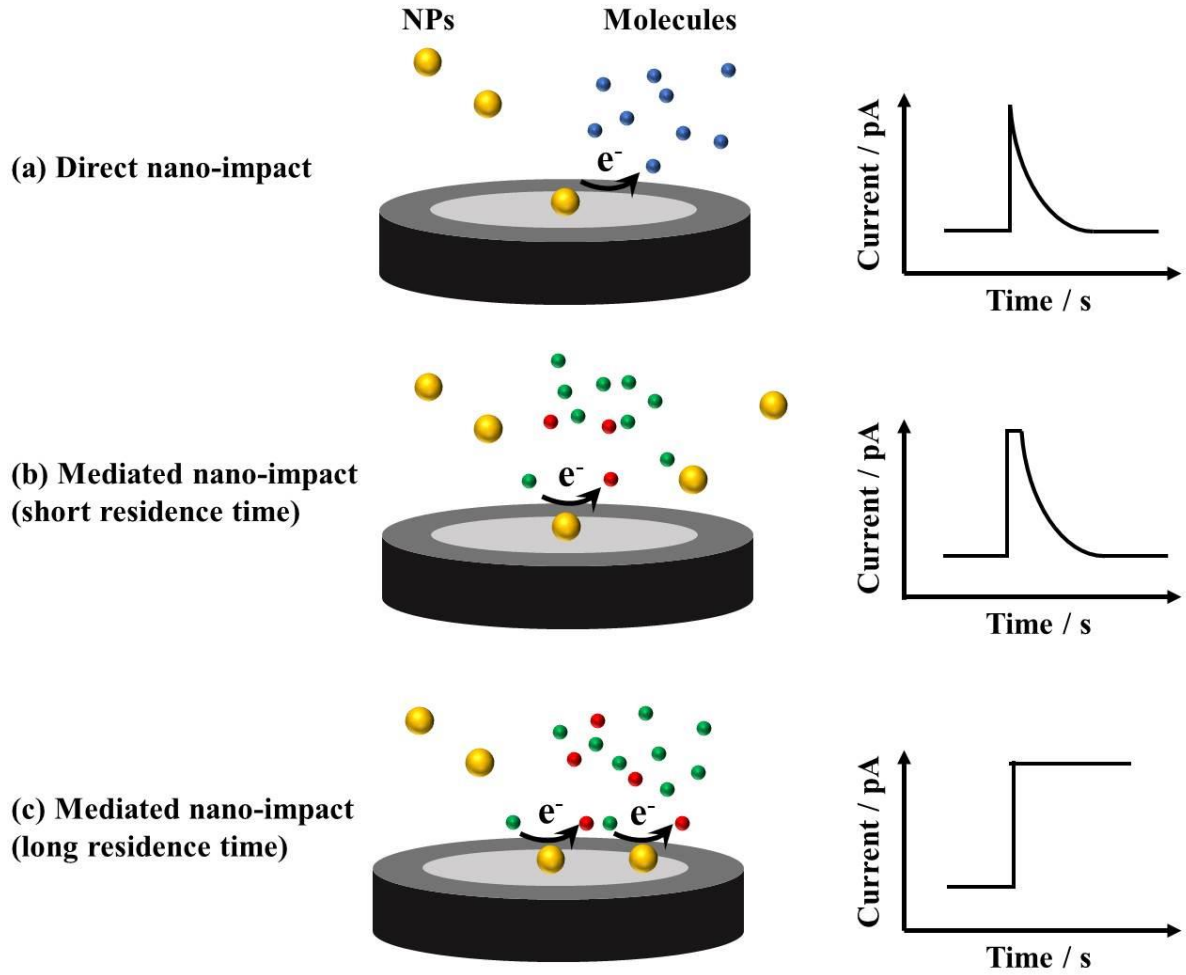

Figure 2.2: The three main scenarios of impact experiments. The current-time transient generated by each mechanism is shown next to the schematic diagram. (a) direct nano-impact, (b) mediated nano-impact with short residence time and (c) mediated nano-impact with long residence time.

Many significant applications of the current amplification from mediated electron transfer are emerging, such as the investigation of single particle activities by analysing the magnitude of the current, which may lead to deeper insights into the specific structure-activity relationship[55] of various nanoparticle systems. Examples range from the initial studies on protonated TiO_2 colloids,[56] to Pt nanoparticles which catalysed proton reduction on impact with a carbon substrate;[50] IrO_x nanoparticles catalysing the oxidation of water on impact with a Pt substrate[57] and the reduction of hydrogen peroxide mediated at silver nanoparticles impacting on carbon.[58]

Even though collision and adsorption of nanoparticles can take place on a macroelectrode, exceedingly high frequencies of collision and huge background signals associated with the large electrode area make it challenging to individually resolve the collision events. Thus a microelectrode is adopted, which not only reduces the collision frequency, but also greatly decreases baseline noise, thereby resulting in clear resolution of single impact events.

In the rest of this thesis, we report the catalytic nano-impacts of palladium nanoparticle decorated carbon nanotubes (CNT-Pds) with the aim of characterising individual CNT-Pds (Chapter 3 and 4) and probing their activities towards different reactions at the single nanoparticle level (Chapter 5 and 6). Exciting results are achieved especially the observation of single nanotube *voltammetry* due to the long residence time of the impacting CNTs on the electrode surface. This eliminates the prime shortcomings of the amperometry where extraction of significant kinetic and thermodynamic information from a sole potential is not feasible and repeat experiments performed over a range of potentials to yield statistically useful information must be undertaken. Single nanotube voltammetry enables us to develop a more comprehensive understanding of the structure-function relationship in nanoparticle-based electrocatalysts. In addition, a comparison between the measurements of ensemble and single nanoparticles not only provides better mechanistic understanding (Chapter 5) but also

gives new insights into the effect of the design of nanomaterials in fuel cell on their performance (Chapter 6). Finally, by using the nano-impact method, an experiment was carried out to quantify the magnitude of the single carbon nanotube-electrode electrical contact via the use of interdigitated electrode arrays (Chapter 7).

References

[1] M. Vert, Y. Doi, K.-H. Hellwich, M. Hess, P. Hodge, P. Kubisa, M. Rinaudo and F. Schué, *Pure Appl. Chem.*, **2012**, *84*, 377.

[2] C. N. R. Rao, G. U. Kulkarni, P. J. Thomas and P. P. Edwards, *Chem. Soc. Rev.*, **2000**, *29*, 27-35.

[3] J. Li and J.-J. Zhu, *Analyst*, **2013**, *138*, 2506-2515.

[4] C. Nützenadel, A. Züttel, D. Chartouni, G. Schmid and L. Schlapbach, *The European Physical Journal D*, **2000**, *8*, 245-250.

[5] R. W. Murray, *Chem. Rev.*, **2008**, *108*, 2688-2720.

[6] D. Strmcnik, M. Uchimura, C. Wang, R. Subbaraman, N. Danilovic, V. van der, A. P. Paulikas, V. R. Stamenkovic and N. M. Markovic, *Nat Chem*, **2013**, *5*, 300-306.

[7] B. E. Conway and B. V. Tilak, *Electrochim. Acta*, **2002**, *47*, 3571-3594.

[8] M. Shao, *Electrocatalysis in Fuel Cells: A Non- and Low- Platinum Approach*, Springer, **2013**.

[9] J. Tafel, *Z. Phys. Chem*, **1905**, *50*, 641.

[10] T. Erdey-Gruz and M. Volmer, *Z. Phys. Chem. A*, **1930**, *150*, 203.

[11] J. Heyrovský, *Recl. Trav. Chim. Pays-Bas*, **1927**, *46*, 582-585.

[12] C. Lin, X. Jiao, K. Tschulik, C. Batchelor-McAuley and R. G. Compton, *J. Phys. Chem. C*, **2015**, *119*, 16121-16130.

[13] M. Shao, *J. Power Sources*, **2011**, *196*, 2433-2444.

[14] X. Jiao, C. Lin, N. P. Young, C. Batchelor-McAuley and R. G. Compton, *J. Phys. Chem. C*, **2016**, *120*, 13148-13158.

[15] E. Santos, P. Quaino and W. Schmickler, *Phys. Chem. Chem. Phys.*, **2012**, *14*, 11224-11233.

[16] R. Parsons, *Trans. Faraday Soc.*, **1958**, *54*, 1053-1063.

[17] P. J. Quaino, F.; Santos, E.; Schmickler, W., *Beilstein J. Nanotechnol.*, **2014**, *5*, 846-854.

[18] S. Trasatti, *J. Electroanal. Chem. Interfacial Electrochem.*, **1972**, *39*, 163-184.

[19] C. Bianchini and P. K. Shen, *Chem. Rev.*, **2009**, *109*, 4183-4206.

[20] T. Takamura and Y. Sato, *Electrochim. Acta*, **1974**, *19*, 63-68.

[21] A. Capon and R. Parsons, *J. Electroanal. Chem. Interfacial Electrochem.*, **1973**, *44*, 239-254.

[22] R. L. McCreery, *Chem. Rev.*, **2008**, *108*, 2646-2687.

[23] K. Gong, F. Du, Z. Xia, M. Durstock and L. Dai, *Science*, **2009**, *323*, 760-764.

[24] P. J. Britto, K. S. V. Santhanam, A. Rubio, J. A. Alonso and P. M. Ajayan, *Adv. Mater.*, **1999**, *11*, 154-157.

[25] G. Che, B. B. Lakshmi, E. R. Fisher and C. R. Martin, *Nature*, **1998**, *393*, 346-349.

[26] S. Zhang, Y. Shao, G. Yin and Y. Lin, *J. Mater. Chem.*, **2010**, *20*, 2826-2830.

[27] J. Kong, M. G. Chapline and H. Dai, *Adv. Mater.*, **2001**, *13*, 1384-1386.

[28] S. Banerjee, K. Dasgupta, A. Kumar, P. Ruz, B. Vishwanadh, J. B. Joshi and V. Sudarsan, *Int. J. Hydrogen Energy*, **2015**, *40*, 3268-3276.

[29] B. Xue, P. Chen, Q. Hong, J. Lin and K. L. Tan, *J. Mater. Chem.*, **2001**, *11*, 2378-2381.

[30] S. Hermans, J. Sloan, D. S. Shephard, B. F. G. Johnson and M. L. H. Green, *Chem. Commun.*, **2002**, DOI: 10.1039/B109923J, 276-277.

[31] J.-P. Tessonnier, L. Pesant, G. Ehret, M. J. Ledoux and C. Pham-Huu, *Appl. Catal. A*, **2005**, *288*, 203-210.

[32] G. G. Wildgoose, C. E. Banks and R. G. Compton, *Small*, **2006**, *2*, 182-193.

[33] V. J. González, C. Martín-Alberca, G. Montalvo, C. García-Ruiz, J. Baselga, M. Terrones and O. Martin, *Carbon*, **2014**, *78*, 10-18.

[34] M. Tavakkoli, T. Kallio, O. Reynaud, A. G. Nasibulin, C. Johans, J. Sainio, H. Jiang, E. I. Kauppinen and K. Laasonen, *Angew. Chem. Int. Ed.*, **2015**, *54*, 4535-4538.

[35] B. M. Quinn, P. G. van't Hof and S. G. Lemay, *J. Am. Chem. Soc.*, **2004**, *126*, 8360-8361.

[36] S. V. Sokolov, S. Eloul, E. Katelhon, C. Batchelor-McAuley and R. G. Compton, *Phys. Chem. Chem. Phys.*, **2017**, *19*, 28-43.

[37] A. J. Bard, H. Zhou and S. J. Kwon, *Isr. J. Chem.*, **2010**, *50*, 267-276.

[38] N. V. Rees, *Electrochem. Commun.*, **2014**, *43*, 83-86.

[39] M. Pumera, *ACS Nano*, **2014**, *8*, 7555-7558.

[40] W. Cheng and R. G. Compton, *Trends Anal. Chem.*, **2014**, *58*, 79-89.

[41] W. Cheng and R. G. Compton, *Trends Anal. Chem.*, **2014**, *58*, 79-89.

[42] H. S. Toh, K. Jurkschat and R. G. Compton, *Chem. Eur. J.*, **2015**, *21*, 2998-3004.

[43] X.-F. Zhou, W. Cheng and R. G. Compton, *Nanoscale*, **2014**, *6*, 6873-6878.

[44] W. Cheng and R. G. Compton, *Angew. Chem. Int. Ed.*, **2014**, *53*, 13928-13930.

[45] X. F. Zhou, W. Cheng and R. G. Compton, *Angew. Chem. Int. Ed.*, **2014**, *53*, 12587-12589.

[46] W. Cheng, X.-F. Zhou and R. G. Compton, *Angew. Chem. Int. Ed.*, **2013**, *52*, 12980-12982.

[47] Y.-G. Zhou, N. V. Rees, J. Pillay, R. Tshikhudo, S. Vilakazi and R. G. Compton, *Chem. Commun.*, **2012**, *48*, 224-226.

[48] Y.-G. Zhou, N. V. Rees and R. G. Compton, *Angew. Chem.*, **2011**, *123*, 4305-4307.

[49] E. J. E. Stuart, K. Tschulik, C. Batchelor-McAuley and R. G. Compton, *ACS Nano*, **2014**, *8*, 7648-7654.

[50] X. Xiao and A. J. Bard, *J. Am. Chem. Soc.*, **2007**, *129*, 9610-9612.

[51] J. M. Kahk, N. V. Rees, J. Pillay, R. Tshikhudo, S. Vilakazi and R. G. Compton, *Nano Today*, **2012**, *7*, 174-179.

[52] Z. Guo, S. J. Percival and B. Zhang, *J. Am. Chem. Soc.*, **2014**, *136*, 8879-8882.

[53] L. S. Y. Ly, C. Batchelor-McAuley, K. Tschulik, E. Kätelhön and R. G. Compton, *J. Phys. Chem. C*, **2014**, *118*, 17756-17763.

[54] A. R. Jung, S. Lee, J. W. Joo, C. Shin, H. Bae, S. G. Moon and S. J. Kwon, *J. Am. Chem. Soc.*, **2015**, *137*, 1762-1765.

[55] K. L. Wustholz, A.-I. Henry, J. M. McMahon, R. G. Freeman, N. Valley, M. E. Piotti, M. J. Natan, G. C. Schatz and R. P. V. Duyne, *J. Am. Chem. Soc.*, **2010**, *132*, 10903-10910.

[56] M. Heyrovsky, J. Jirkovsky and M. Struplova-Bartackova, *Langmuir*, **1995**, *11*, 4300-4308.

[57] S. J. Kwon, F.-R. F. Fan and A. J. Bard, *J. Am. Chem. Soc.*, **2010**, *132*, 13165-13167.

[58] E. J. E. Stuart, N. V. Rees and R. G. Compton, *Chem. Phys. Lett.*, **2012**, *531*, 94-97.

Chapter 3

Ultra-small Palladium Nanoparticle Decorated Carbon Nanotubes: Conductivity and Reactivity

Carbon nanotubes decorated with ultra-small metal nanoparticles have great value in catalysis. In this chapter, we show that individual ultra-small palladium nanoparticle decorated multiwalled carbon nanotubes can be detected via the nano-impacts method (Chapter 2, Section 2.2). The high conductivity and reactivity of individual decorated carbon nanotubes is directly evidenced; this is achieved by studying the proton reduction reaction to form under-potential deposited hydrogen on the nanoparticles decorated on the carbon nanotube walls. The reductive spikes from current amplification are analyzed to estimate the approximate length of the decorated carbon nanotubes, revealing that the decorated carbon nanotube is electroactive along its entire length of several micrometers.

The work herein presented has been published in *ChemPhysChem*[1] and was carried out in collaboration with Dr. Christopher Batchelor-McAuley, Dr. Kristina Tschulik and Prof. Dr. Lidong Shao. Dr. Christopher Batchelor-McAuley and Dr. Kristina Tschulik helped with the interpretation of the experimental results. Dr. Kristina Tschulik obtained the scanning electron microscope images. Prof. Dr. Lidong Shao performed the synthesis, transmission electron microscopy and energy-dispersive X-ray spectroscopy for the decorated carbon nanotubes.

3.1 Introduction

Carbon nanotubes (CNTs) are one of the most intensively studied nanomaterials because of their special set of mechanical and electrical properties. In particular, their physical properties and morphology make them extremely attractive as supports for heterogeneous catalysts.[2-6] One area of increasing interest is in CNTs serving as optimized templates for the immobilization/deposition of metal nanoparticles to form nano-architectures. Thus, CNTs decorated with metal nanoparticles (Pt, Pd, Ru, Au, Ag, Cu, Fe, alloys and metal oxides etc.) have been developed for highly efficient catalysis,[7-12] hydrogen storage and sensing,[13, 14] biological applications such as fabrication of electrochemical biosensors,[15, 16] and particularly hydrogen and methanol oxidation, or oxygen reduction catalysis for fuel cell and battery technologies in energy storage applications.[17-22] Moreover, nanoparticles in the size range of 1-3 nm, called ultra-small nanoparticles (USNPs), are known to possess properties distinct from those of free molecules or larger-sized nanoparticles.[23] It has been revealed that compared to their larger-sized counterparts USNPs exhibit remarkably enhanced catalytic activities because of their enormously large surface areas and distinct electronic structures.[24-26]

In the 'nano-impact' method, as introduced in Chapter 2, mediated electron transfer can take place on the surface of impacting nanoparticles. In the experimental setups the mediated reaction leads to current amplification of the impact event facilitating stochastic measurement of the rates of reaction at individual particles; most research focuses on electrocatalytic processes.[27-32] Single particle activities can be evaluated by analysing the magnitude of the current, leading to deeper insights into the specific structure-activity relationship [33] of nanoparticles. In addition, the mediated 'nano-impact' holds great potential for the study and validation of the fundamentals and dynamics of electrochemical processes by the measurement of the current at the nanoscale.[34, 35]

In this chapter, for the first time, we use current amplification by proton reduction and the production of under-potential deposited hydrogen (H_{UPD}) on multiwalled carbon nanotube supported ultra-small palladium nanoparticles (CNT-Pd) as an indicator to evidence the electrode collision of individual carbon nanotubes. H_{UPD} is an electrodeposition product of proton reduction at a potential less negative than its equilibrium potential, and it is characteristic of Pt group metals only. The nano-impacts approach enables the non-destructive and stochastic detection of single decorated CNTs. The correspondence between the electrochemical measurement of the approximate length distribution of individual CNT-Pd, as estimated from the magnitude of the current spikes, and the SEM sizing provides direct evidence for the high conductivity and reactivity of the entire length of the ultra-small palladium nanoparticles decorated carbon nanotubes.

3.2 Experimental section

3.2.1 Chemicals

PR24-LHT carbon nanotubes were purchased from Pyrograf Products Inc. (Ohio, USA). Nitric acid (70%) (HNO_3) and Potassium nitrate (KNO_3) were acquired from Sigma-Aldrich and used as received without further purification. 0.20 M KNO_3 was used as a supporting electrolyte in all cyclic voltammetric and chronoamperometric measurements. All solutions were made up with deionised water of resistivity not less than 18.2 MΩ cm (Millipore) at 298 K and degassed with nitrogen (oxygen-free, BOC Gases plc) before use.

3.2.2 Preparation of multi-walled carbon nanotubes decorated with palladium nanoparticles (CNT-Pd)

Concentrated nitric acid was used to functionalize carbon nanotubes at 120°C for 1 h. Palladium nitrate (ca. 40% Pd, Roth) was dissolved in ethanol. Functionalized carbon nanotubes were then added into the solution. Ultrasonication was carried out and followed by evaporation using stirring at room temperature. The sample was then collected and reduced in 25% H_2 mixed with He in a total flow of 100 mL min^{-1} at 200°C.

3.2.3 Characterization of CNT-Pd

The prepared CNT-Pd were characterized with Transmission Electron Microscopy (TEM), Energy-dispersive X-ray Spectroscopy (EDX) mapping and Scanning Electron Microscopy (SEM) respectively. A FEI aberration-corrected Titan 80-300 TEM was employed to conduct structural investigations in TEM mode (Figure 1(a)) and the EDX mapping analysis (Figure S1). SEM Imaging of CNT-Pd was conducted with a Leo Gemini II Field Emission Gun Scanning Electron Microscope (Zeiss, Germany) using a detector in in-lens geometry at an acceleration voltage of 5 kV. A suspension of CNT-Pd was briefly sonicated in water and then drop cast on a sample holder prior to SEM analysis. The software ImageJ (The National Institute of Health, USA) was employed to analyze the SEM images and determine the size distribution of the CNT-Pd.

3.2.4 Preparation of CNT-Pd suspensions

A suspension of 9.7×10^{-13} mol L^{-1} CNT-Pd was prepared by adding 1.2 mg of CNT-Pd to 20 mL supporting electrolyte. To get a well dispersed solution, the suspension was then sonicated for 10 min in a Fisher Scientific FB15050 ultrasonic bath. The above suspension was used as a stock solution, and diluted to obtain the suspensions for the following measurements.

3.2.5 Sticking experiments and cyclic voltammetry

Sticking measurements were performed by immersing a glassy carbon (GC) electrode (diameter: 3.0 mm) in a suspension of 9.7×10^{-13} mol L^{-1} CNT-Pd for 120 min, leading to the in situ immobilisation of CNT-Pd on the electrode as a result of the irreversible adsorption of the CNT-Pd onto the electrode surface. To keep the suspension well dispersed during the period of sticking, the suspension was sonicated for 1 min in the absence of the electrode after every 20 min of sticking. Subsequent cyclic voltammetry was carried out at 298 K in a double Faraday cage with three electrode system using an Autolab III potentiostat (Metrohm-Autolab BV, Netherlands) and NOVA 1.10 software. The as-prepared GC electrode was used as the working electrode, a mercury-mercurous sulfate electrode (MSE) as the reference electrode and a platinum foil as the counter electrode. 20 mL of aqueous solution containing 0.20 M KNO_3 and 1.0 mM HNO_3 was used for test solutions and was degassed with nitrogen for 5 min to remove dissolved electroactive oxygen before the measurements. Analogous experiments were also carried out in the same solution but in the absence of HNO_3.

3.2.6 Nano-impact experiments

Nano-impact experimental measurements were made by applying a potential step and then monitoring current as a function of time (chronoamperometry) using an Autolab II

potentiostat (Metrohm-Autolab BV, Netherlands) and NOVA 1.10 software. A carbon fibre wire microelectrode of 7 μm diameter and 1 mm in length was used as the working electrode, together with the same reference electrode and counter electrode as above. The fabrication method of carbon fibre wire microelectrodes has been reported previously.[36] 20 mL of aqueous solution with 0.20 M KNO_3 and 1.0 mM HNO_3 was used as a test solution, which was degassed with nitrogen for 5 min to remove dissolved electroactive oxygen, and then 600 μL CNT-Pd stock solution (9.7×10^{-13} mol L^{-1}) was added while nitrogen kept bubbling for 10 s more, following by immediate chronoamperometric scans. The resultant suspensions of 2.8×10^{-14} mol L^{-1} CNT-Pd were also investigated in the absence of 1.0 mM HNO_3. The impact spike identification and individual spike area determination were conducted with the program "Signal Counter" (Centre for Marine and Environmental Research, Zagreb, Croatia).[37]

3.3 Results and discussion

3.3.1 Characterization of CNT-Pd

The prepared CNT-Pd was characterized with TEM (Figure 3.1a), SEM (Figure 3.1b) and EDX mapping (Figure 3.2) respectively. Tube shaped nanostructures are observed in both the TEM and SEM images (Figure 3.1), and highly dispersed spherical nanoparticles on the surface of the nanotube are shown in the TEM image. A total of 96 random samples of palladium nanoparticles from the TEM images were analysed, giving a mean diameter of palladium nanoparticles as 1.36 ± 0.37 nm (inset Figure 3.1a). The length (48 samples) and width (53 samples) distributions of CNTs displayed in the SEM images are 5.87 ± 2.40 μm (inset Figure 3.1b) and 127.4 ± 19.4 nm respectively. Moreover, the EDX maps shown in Figure 3.2 evidence the existence of the elements C, O and Pd in the materials.

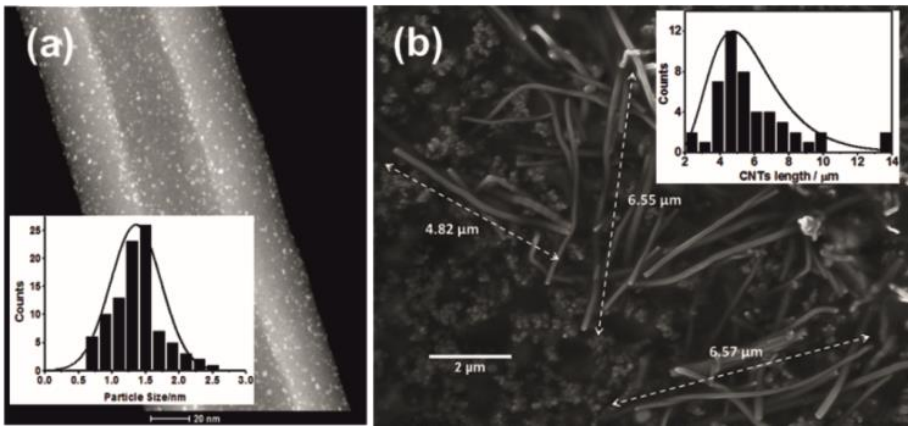

Figure 3.1: (a) TEM image of CNT-Pd. The inset shows the diameter (1.36 ± 0.37 nm) distribution of palladium nanoparticles decorated on a carbon nanotube. (b) SEM image of CNT-Pd. The inset shows the length (5.87 ± 2.40 µm) distribution of the decorated CNTs.

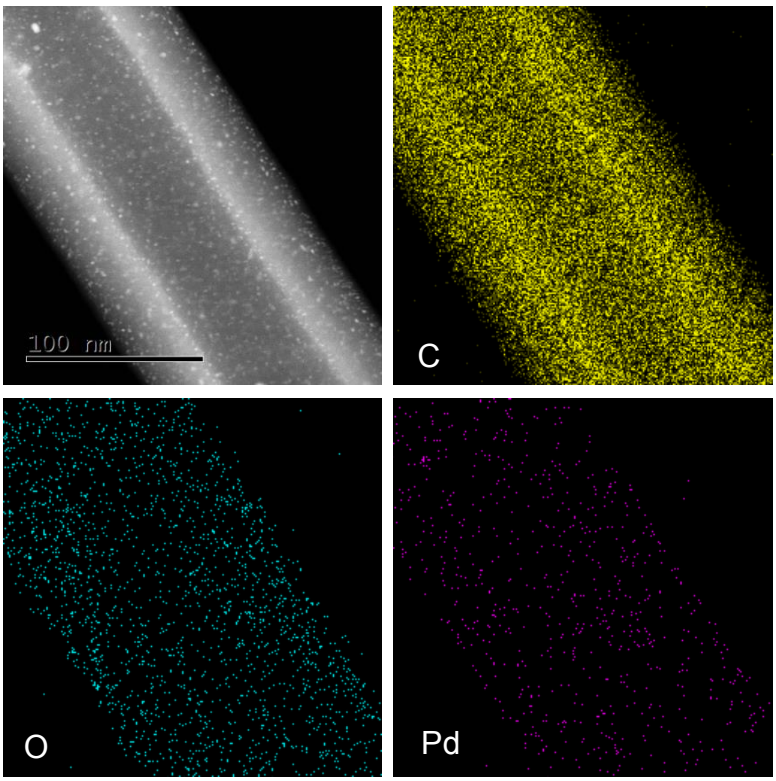

Figure 3.2: TEM image and EDX maps (C, O, Pd) of CNT-Pd.

To calculate the surface coverage of palladium nanoparticles on the carbon nanotube surface, the zoom-in TEM images (Figure 3.3) were analysed. 90 samples of palladium

nanoparticles were observed on the surface of carbon nanotubes with an area of 1.11×10^{-15} m^2, giving the surface coverage of palladium nanoparticles on CNT-Pd as 8.11×10^{16} m^{-2}.

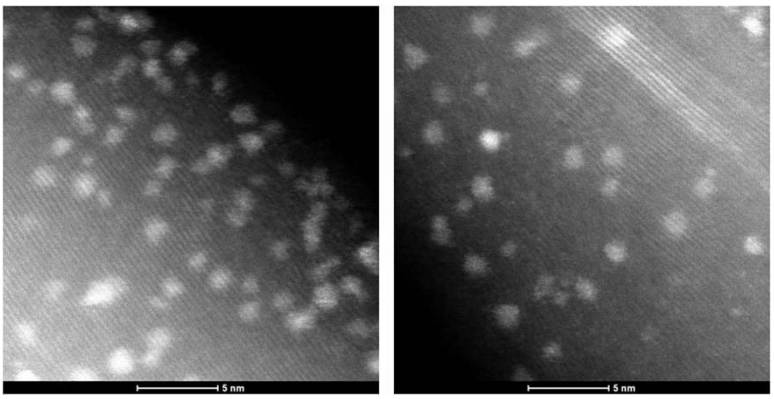

Figure 3.3: TEM images of CNT-Pd used for the calculation of surface coverage of palladium nanoparticles on CNT-Pd.

3.3.2 Cyclic voltammetry of the dropcast CNT-Pd

To characterize the CNT-Pd in aqueous solution and determine a suitable potential for chronoamperometry measurements, CNT-Pd 'sticking' experiments were performed by immersing a glassy carbon (GC) electrode (diameter: 3.0 mm) in an aqueous suspension of 9.7×10^{-13} mol L^{-1} CNT-Pd for 120 min. During this process, collisions of some CNT-Pd with the electrode by virtue of their Brownian motion led to the immobilization of CNT-Pd on the electrode as a result of the irreversible adsorption of the CNT-Pd onto the electrode surface. Subsequently, cyclic voltammetry (CV) was carried out to determine the coverage of CNT-Pd on the electrode. As shown in the inset of Figure 3.4, no CV signal was observed for a solution containing no KNO_3. Analogous experiments were then performed in the same solution but in the presence of 1.0 mM HNO_3. The resulting CV curves are also shown in Figure 3.4. The two reduction peaks at -1.15 V (*vs.* MSE) and -0.40 V (*vs*. MSE) were observed and correspond to hydrogen evolution and H_{UPD} respectively,[38] both of which are

attributed to the proton reduction on the surface of the palladium nanoparticles decorated on the CNTs. No such features are observed for undecorated CNTs.

In the potential range of H_{UPD} production, as shown in Figure 3.4 (the red curve), the formed surface H_{UPD} can undergo an interfacial transfer from the electro-adsorbed state to an absorbed state through an intermediate subsurface state.[39] Consequently, we must consider two possible contributions to the H_{UPD} signal at -0.4 V, specifically that from surface and 'bulk' hydrogen. To identify the specific contribution of the two different forms of sorption hydrogen on the CV signals, calculations accounting for the absence and presence of bulk absorption were separately analysed to quantify the amount of CNT-Pd adherent on the electrode. The estimated charge density for surface *adsorption* is 255 μC cm^{-2}, this value is attained from assuming a coverage of one hydrogen atom per Pd surface atom of a close-packed Pd (111) surface.[40] The charge contributed per palladium nanoparticle is calculated to be 1.48×10^{-17} C when only surface adsorption is considered. In the presence of bulk *absorption*, where the composition of palladium hydride at room temperature is $PdH_{0.6}$,[41] leads to an estimate of 2.34×10^{-17} C of charge per palladium nanoparticle. The voltammetric experimental results show that the average total amount of charge for the cathodic and anodic peaks is 4.50 μC. Thus, the total accumulative number of palladium nanoparticles on the electrode surface was calculated to be 3.04×10^{-11} and 1.92×10^{-11} respectively. Based on these values and the measured surface coverage (8.11×10^{16} m^{-2}) of the palladium nanoparticles on the CNT-Pd from the TEM images (Figure 3.3), the total accumulative length of carbon nanotubes (*ca.* 9.4 m for surface adsorption only and 5.9 m for surface adsorption and bulk absorption combined) on the electrode surface is derived directly from the total accumulative surface area of the carbon nanotubes and the measured 127.4 nm average diameter from the SEM analysis.

Consequently, the charge contributed by one meter of carbon nanotube is calculated to be 4.8×10^{-7} C m^{-1} for surface adsorption only and 7.6×10^{-7} C m^{-1} for surface adsorption and bulk absorption combined. The difference in charge between the limiting cases is too small to distinguish here. Notably, the comparable magnitudes for the two values is related to the small size of the individual palladium nanoparticles.[42] The above results in this section thus show that by using the 'sticking' method followed by CV, the CNT-Pd in aqueous solution can be pre-concentrated, immobilised and quantified.

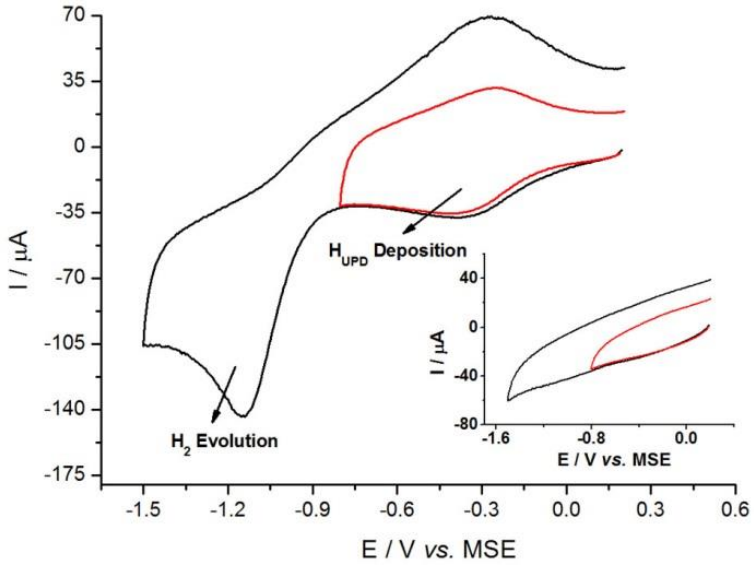

Figure 3.4: Voltammetric profiles at a scan rate of 1.6 V s^{-1} from a glassy carbon macroelectrode (d = 3.0 mm) in 0.20 M KNO_3 in the presence and absence (inset) of 1.0 mM HNO_3 after immersing in a suspension containing CNT-Pd of 9.7×10^{-13} mol L^{-1} for 120 min. Red curves: the voltammetric curves for H_{UPD} deposition.

3.3.3 Nano-impacts of CNT-Pd

Nano-impacts experiments of CNT-Pd were conducted by recording chronoamperograms at a clean carbon fibre wire microelectrode[36] (d = 7.0 μm; l = 1.0 mm) in 0.20 M KNO_3, 1.0 mM HNO_3 and 2.8×10^{-14} mol L^{-1} CNT-Pd. Based on the CV results reported above, a

reductive potential -0.80 V (*vs.* MSE) was used for the chronoamperometry to ensure the production of sorption hydrogen on the palladium nanoparticles when the individual CNT-Pd collided with the wire electrode by virtue of their Brownian motion. As shown in Figure 3.5(a), reductive spikes from proton reduction and the production of H_{UPD} on the palladium nanoparticles decorated on individual carbon nanotubes were detected at -0.80 V (*vs.* MSE). The slight increase of the background current in the presence of CNT-Pd might be attributed to the permanent sticking of some carbon nanotubes on the surface of wire electrode during the measurement. It was found that these Faradaic spikes were dependent on potential: no spikes were observed at the positive potential +0.20 V (*vs.* MSE) (Figure 3.6), which indicates that those spikes are a result of proton reduction on CNT-Pd. The same solution containing no CNT-Pd was used to perform control experiments (black curve in Figure 3.5), and no spikes were observed at the potential of -0.80 V (*vs.* MSE), confirming that these current spikes result from the random collisions of single CNT-Pd with the wire microelectrode and the proton reduction by electron transfer from the electrode (Figure 3.7).

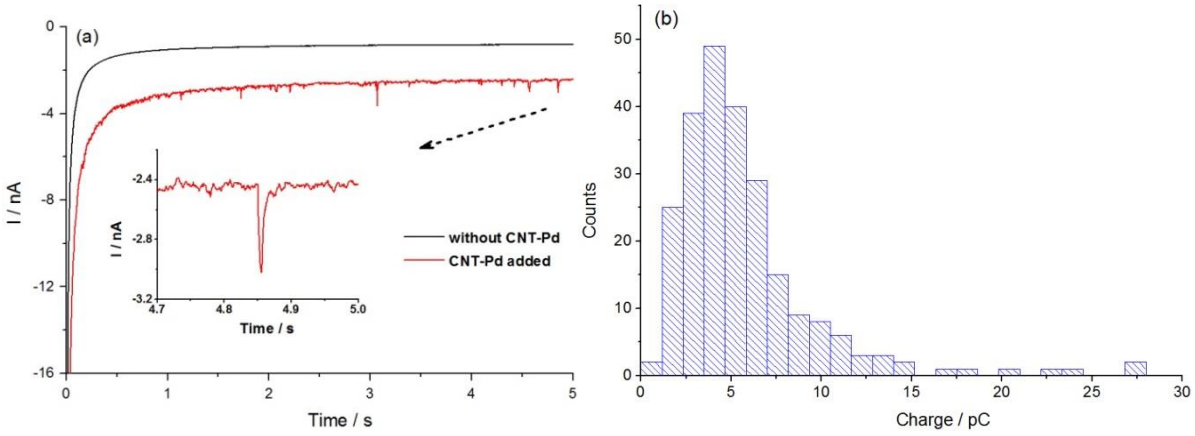

Figure 3.5: (a) Chronoamperometric profiles showing reductive Faradaic spikes from proton reduction and the production of H_{UPD} on CNT-Pd in 1.0 mM HNO_3, 0.20 M KNO_3 at -0.80 V (*vs.* MSE). The inset is an enlarged view of impact spikes; (b) Charge distribution of 237 current spikes from proton reduction and the production of H_{UPD} on CNT-Pd.

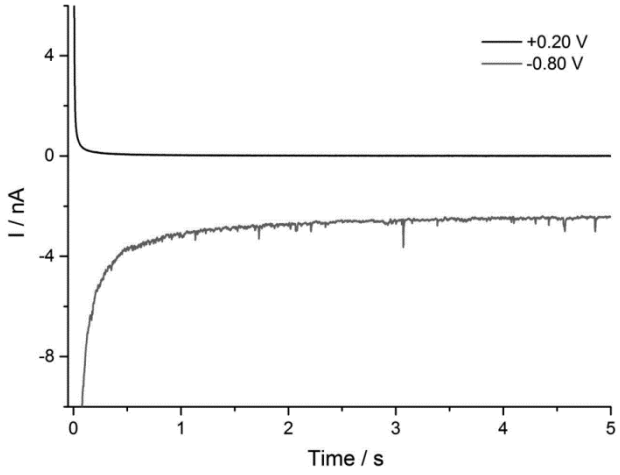

Figure 3.6: Chronoamperometric profiles of CNT-Pd in 1.0 mM HNO_3, 0.20 M KNO_3 at +0.20 V (*vs.* MSE) (the black curve) and -0.80 V (*vs.* MSE) (the grey curve).

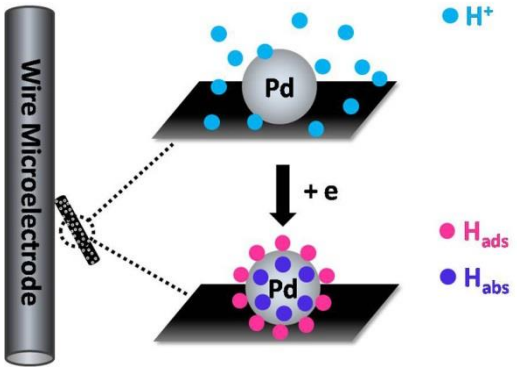

Figure 3.7: Illustration of the process of H_{UPD} production during the collision of single CNT-Pd with the wire microelectrode.

At -0.80 V, a total number of 237 spikes were collected from 6 chronoamperograms each of 20 seconds duration; the spikes correspond to the production of sorption hydrogen from proton reduction on 237 CNT-Pd. Individual current spikes were integrated to get the charge from each collision of CNT-Pd. The charge distribution is shown in Figure 3.5(b). Herein, for the first time, the production of H_{UPD} from proton reduction on individual palladium nanoparticles decorated CNTs was observed and measured during random collisions of the decorated carbon nanotube with the electrode by Brownian motion. Furthermore, based on

the unit charge per meter carbon nanotube from the calculation before (section 3.3.2), the length of the individual carbon nanotubes was derived by the charge of the corresponding reduction spikes according to two different forms of sorption. The length distribution of the CNTs in the cases of surface adsorption of H_{UPD} in the absence and presence of bulk absorption on the palladium nanoparticles are shown in Figure 3.8 (red circles), giving the mean length of CNT-Pd as 12.0 ± 8.4 μm and 7.6 ± 5.3 μm respectively.

Typical SEM images (Figure 3.1) from the same batch of CNT-Pd were analysed and the mean width and length of CNTs are 127.4 ± 19.4 nm (53 samples) and 5.9 ± 2.4 μm (48 samples) respectively. The mean length of CNTs from SEM images is slightly less than the inferred sizes from the nano-impacts method, which is tentatively attributed to the aggregation of a small amount of CNTs. Figure 3.8 shows the comparison of the length distribution from analysis of SEM images and the nano-impacts method. As displayed in Figure 3.8, the results from the case where surface adsorption and bulk absorption combined show better correspondence with the SEM results, however the difference is small due to the dimensions of the individual palladium nanoparticles employed here.

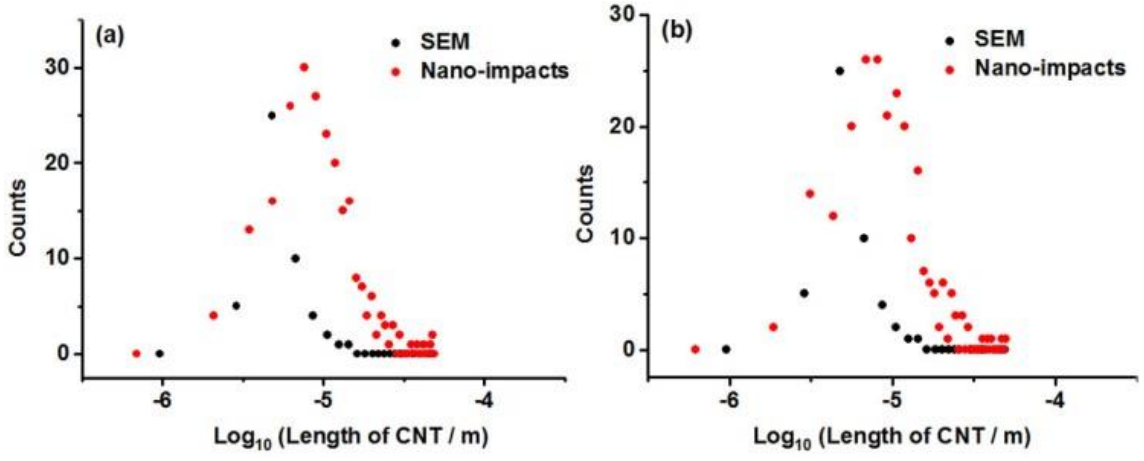

Figure 3.8: Comparison of the length distribution from analysis of SEM images (53 samples) and the nano-impacts method (237 spikes) in the cases of: (a) surface adsorption and (b) surface adsorption and bulk absorption of H_{UPD} on palladium nanoparticles.

Last, a further comparative experiment was carried out at a potential of -0.80 V without 1.0 mM HNO_3 in the solution and small spikes with 5.5×10^{-13} C of average charge were measured (Figure 3.9), which is significantly less than 6.2×10^{-12} C of average charge from the Faradaic reductive spikes. These small spikes are likely due to capacitive changes of the double layer on the wire microelectrode caused by collision of carbon nanotube with the electrode.[43-45]

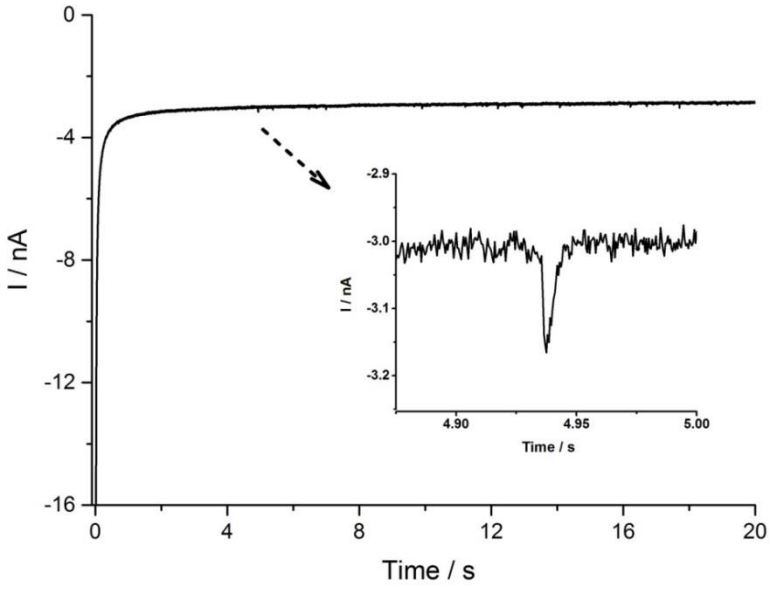

Figure 3.9: Chronoamperometric profiles of CNT-Pd in 0.20 M KNO_3 in the absence of HNO_3 at -0.80 V (vs. MSE).

3.4 Conclusions

In this chapter, individual CNTs were detected with the nano-impacts method for the first time using the production of H_{UPD} from proton reduction on ultra-small palladium nanoparticle decorated carbon nanotubes. From knowledge of the palladium nanoparticle sizes and coverage of the CNTs it was further demonstrated how the magnitude of impact charge allows an assessment of the nanotube lengths. The correspondence between electrochemical sizing and microscopy results directly shows that the ultra-small palladium

nanoparticle decorated carbon nanotube is electroactive along its entire length, evidencing the reactivity and conductivity of the CNTs and further indicating the complete H_{UPD} saturation of the ultra-small palladium nanoparticles decorated on the carbon nanotubes. Having evidenced the reactivity and conductivity of palladium nanoparticle decorated carbon nanotubes, the following chapters will sequentially explore electrocatalytic nano-impacts of single decorated carbon nanotubes in which various redox reactions such as hydrogen oxidation reaction (HOR), oxygen reduction reaction (ORR), methanol and formate oxidation reactions are catalysed, so that the fundamentals and dynamics of electrocatalytic processes can be investigated by the measurement of electrocatalytic impact current at the nanoscale.

References

[1] X. Li, C. Batchelor-McAuley, K. Tschulik, L. Shao and R. G. Compton, *ChemPhysChem*, **2015**, *16*, 2322-2325.

[2] P. Serp, M. Corrias and P. Kalck, *Appl. Catal. A*, **2003**, *253*, 337-358.

[3] D. Vairavapandian, P. Vichchulada and M. D. Lay, *Anal. Chim. Acta*, **2008**, *626*, 119-129.

[4] J. M. Schnorr and T. M. Swager, *Chem. Mater.*, **2011**, *23*, 646-657.

[5] E. Lam and J. H. T. Luong, *ACS Catal.*, **2014**, *4*, 3393-3410.

[6] C. J. Shearer, A. Cherevan and D. Eder, *Adv. Mater.*, **2014**, *26*, 2295-2318.

[7] B. Xue, P. Chen, Q. Hong, J. Lin and K. L. Tan, *J. Mater. Chem.*, **2001**, *11*, 2378-2381.

[8] S. Hermans, J. Sloan, D. S. Shephard, B. F. G. Johnson and M. L. H. Green, *Chem. Commun.*, **2002**, *0*, 276-277.

[9] J.-P. Tessonnier, L. Pesant, G. Ehret, M. J. Ledoux and C. Pham-Huu, *Appl. Catal. A*, **2005**, *288*, 203-210.

[10] G. G. Wildgoose, C. E. Banks and R. G. Compton, *Small*, **2006**, *2*, 182-193.

[11] V. J. González, C. Martín-Alberca, G. Montalvo, C. García-Ruiz, J. Baselga, M. Terrones and O. Martin, *Carbon*, **2014**, *78*, 10-18.

[12] M. Tavakkoli, T. Kallio, O. Reynaud, A. G. Nasibulin, C. Johans, J. Sainio, H. Jiang, E. I. Kauppinen and K. Laasonen, *Angew. Chem. Int. Ed.*, **2015**, *54*, 4535-4538.

[13] J. Kong, M. G. Chapline and H. Dai, *Adv. Mater.*, **2001**, *13*, 1384-1386.

[14] S. Banerjee, K. Dasgupta, A. Kumar, P. Ruz, B. Vishwanadh, J. B. Joshi and V. Sudarsan, *Int. J. Hydrogen Energy*, **2015**, *40*, 3268-3276.

[15] S. G. Penn, L. He and M. J. Natan, *Curr. Opin. Chem. Biol.*, **2003**, *7*, 609-615.

[16] H.-F. Cui, J.-S. Ye, W.-D. Zhang, J. Wang and F.-S. Sheu, *J. Electroanal. Chem.*, **2005**, *577*, 295-302.

[17] D.-J. Guo and H.-L. Li, *J. Colloid Interface Sci.*, **2005**, *286*, 274-279.

[18] Z. He, J. Chen, D. Liu, H. Zhou and Y. Kuang, *Diamond Relat. Mater.*, **2004**, *13*, 1764-1770.

[19] J. Qu, Y. Shen, X. Qu and S. Dong, *Chem. Commun.*, **2004**, DOI: 10.1039/B311038A, 34-35.

[20] G. Che, B. B. Lakshmi, E. R. Fisher and C. R. Martin, *Nature*, **1998**, *393*, 346-349.

[21] J. Tuček, K. C. Kemp, K. S. Kim and R. Zbořil, *ACS Nano*, **2014**, *8*, 7571-7612.

[22] M. Carmo, V. A. Paganin, J. M. Rosolen and E. R. Gonzalez, *J. Power Sources*, **2005**, *142*, 169-176.

[23] B. H. Kim, M. J. Hackett, J. Park and T. Hyeon, *Chem. Mater.*, **2014**, *26*, 59-71.

[24] C. Harding, V. Habibpour, S. Kunz, A. N.-S. Farnbacher, U. Heiz, B. Yoon and U. Landman, *J. Am. Chem. Soc.*, **2009**, *131*, 538-548.

[25] W. Chen and S. Chen, *Angew. Chem. Int. Ed.*, **2009**, *48*, 4386-4389.

[26] H. Qian, M. Zhu, Z. Wu and R. Jin, *Acc. Chem. Res.*, **2012**, *45*, 1470-1479.

[27] X. Xiao and A. J. Bard, *J. Am. Chem. Soc.*, **2007**, *129*, 9610-9612.

[28] A. J. Bard, H. Zhou and S. J. Kwon, *Isr. J. Chem.*, **2010**, *50*, 267-276.

[29] J. M. Kahk, N. V. Rees, J. Pillay, R. Tshikhudo, S. Vilakazi and R. G. Compton, *Nano Today*, **2012**, *7*, 174-179.

[30] Z. Guo, S. J. Percival and B. Zhang, *J. Am. Chem. Soc.*, **2014**, *136*, 8879-8882.

[31] L. S. Y. Ly, C. Batchelor-McAuley, K. Tschulik, E. Kätelhön and R. G. Compton, *J. Phys. Chem. C*, **2014**, *118*, 17756-17763.

[32] A. R. Jung, S. Lee, J. W. Joo, C. Shin, H. Bae, S. G. Moon and S. J. Kwon, *J. Am. Chem. Soc.*, **2015**, *137*, 1762-1765.

[33] K. L. Wustholz, A.-I. Henry, J. M. McMahon, R. G. Freeman, N. Valley, M. E. Piotti, M. J. Natan, G. C. Schatz and R. P. V. Duyne, *J. Am. Chem. Soc.*, **2010**, *132*, 10903-10910.

[34] E. J. F. Dickinson and R. G. Compton, *J. Electroanal. Chem.*, **2011**, *661*, 198-212.

[35] M. C. Henstridge, K. R. Ward and R. G. Compton, *J. Electroanal. Chem.*, **2014**, *712*, 14-18.

[36] J. Ellison, C. Batchelor-McAuley, K. Tschulik and R. G. Compton, *Sens. Actuators, B*, **2014**, *200*, 47-52.

[37] J. Ellison, K. Tschulik, E. J. E. Stuart, K. Jurkschat, D. Omanović, M. Uhlemann, A. Crossley and R. G. Compton, *ChemistryOpen*, **2013**, *2*, 69-75.

[38] C. Gabrielli, P. P. Grand, A. Lasia and H. Perrot, *J. Electrochem. Soc.*, **2004**, *151*, A1937-A1942.

[39] G. Jerkiewicz, *Electrocatalysis*, **2010**, *1*, 179-199.

[40] L.-J. Wan, T. Suzuki, K. Sashikata, J. Okada, J. Inukai and K. Itaya, *J. Electroanal. Chem.*, **2000**, *484*, 189-193.

[41] L. L. Jewell and B. H. Davis, *Appl. Catal. A*, **2006**, *310*, 1-15.

[42] C. Batchelor-McAuley, C. E. Banks, A. O. Simm, T. G. J. Jones and R. G. Compton, *ChemPhysChem*, **2006**, *7*, 1081-1085.

[43] N. V. Rees, C. E. Banks and R. G. Compton, *J. Phys. Chem. B*, **2004**, *108*, 18391-18394.

[44] C. E. Banks, N. V. Rees and R. G. Compton, *J. Phys. Chem. B*, **2002**, *106*, 5810-5813.

[45] J. Poon, C. Batchelor-McAuley, K. Tschulik and R. G. Compton, *Chem. Sci.*, **2015**, *6*, 2869-2876.

Chapter 4

Single Nanoparticle Voltammetry: Contact Modulation of the Mediated Current

As a paradigm electrocatalytic reaction, the hydrogen oxidation is first investigated on individual palladium coated carbon nanotubes via the electrocatalytic nano-impact method. The cyclic voltammetric responses of *individual* palladium coated carbon nanotubes are reported. Upon impact - from the solution phase - with the electrified interface, the nanoparticles act as individual nanoelectrodes catalyzing the hydrogen oxidation reaction. At high overpotentials the current is shown to reach a quasi-steady-state diffusion limit, allowing determination of the tube length. The electrochemical response of the individual nanotubes also reveals the system to be modulated by the electrical contact between the electrode and carbon nanotube. This modulation presents itself as fluctuations in the recorded Faradaic current.

The work has been published in *Angewandte Chemie International Edition*[1] and was performed in collaboration with Dr. Christopher Batchelor-McAuley, Mr. Samuel A. I. Whitby, Dr. Kristina Tschulik and Prof. Dr. Lidong Shao. Dr. Christopher Batchelor-McAuley and Dr. Kristina Tschulik helped with the interpretation of the experimental results. Mr. Samuel A. I. Whitby is recognised for his contribution in collecting some of the experimental results. Prof. Dr. Lidong Shao carried out the synthesis, transmission electron microscopy and energy-dispersive X-ray spectroscopy for the palladium decorated carbon nanotubes. Dr. Kristina Tschulik conducted the scanning electron microscopy analysis.

4.1 Introduction

Electrochemical reactions can be monitored at single nanoparticles impacting at an inert electrode.[2-7] One distinct aim of such investigations is to facilitate insight into the structure-activity relationship of specific nanoparticle systems.[8] Almost invariably, these mediated nanoparticle studies are performed using a single potential held upon the substrate electrode. However, extraction of physically significant kinetic and thermodynamic information from a single electrochemical potential is not feasible and repeat experiments performed over a range of potentials to yield statistically useful information must be undertaken.[9] Moreover, data analysis of the resulting currents assumes the process to *not* be influenced by the properties of the electrical contact between the 'inert' electrode and the nanoparticle. Previous studies of the electrochemistry of single nanotubes have required the employment of complex fabrication techniques.[10] Conversely, in this chapter the hydrogen oxidation (HOR) is studied on individually impacting nitrogen-doped multi-walled carbon nanotube supported palladium nanoparticles (N-CNT-Pd) via cyclic voltammetry (CV) enabling the non-destructive sizing of single decorated CNTs. These studies clearly demonstrate that, for this experimental case, although at high overpotentials diffusion limited currents are obtained, the mediated electrochemical process is modulated by the contact between the electrode and the nanoparticle. Consequently, extraction of physically significant data regarding the kinetics of the electrochemical process will require greater insight into properties of the electrical contact between the nanoparticle and the inert substrate.

4.2 Experimental section

4.2.1 Chemicals

PR24-LHT carbon nanotubes were purchased from Pyrograf Products Inc. (Ohio, USA). Palladium nitrate solution (10 wt% $Pd(NO_3)_2$ in 10 wt% HNO_3) and potassium nitrate (KNO_3) were acquired from Sigma-Aldrich and used as received without further purification. Hydrogen (≥99.98% H_2) and nitrogen were supplied from BOC, Surrey, U.K. All solutions were made up with deionised water of resistivity not less than 18.2 MΩ cm (Millipore) at 298 K and degassed with nitrogen before use.

4.2.2 Preparation of nitrogen doped multi-walled carbon nanotubes decorated with palladium nanoparticles (N-CNT-Pd)

(We thank Prof. Dr. L. Shao for preparing the palladium nanoparticle decorated carbon nanotubes and characterizing it with the TEM technique)

N-CNT-Pd was prepared by the following route: functionalization was first carried out on carbon nanotubes (CNTs) by oxidation in HNO_3. Gaseous NH_3 was then flowed over oxidized CNTs (O-CNTs) in a tubular quartz reactor at 600°C for 4 h to introduce nitrogen-containing functional groups on the CNTs (N-CNTs). Palladium ions were added to a solution of functionalized CNTs for coordination with functionalities as anchoring sites. Appropriate hydrolysis treatment was applied to the impregnated materials to crystallize the precursors to achieve a 2.4 wt% loading (measured by inductively coupled plasma (ICP)) of Pd supported on N-CNTs (N-CNT-Pd) with a high dispersion scale.

4.2.3 Characterization of N-CNT-Pd

The prepared N-CNT-Pds were characterized with Transmission Electron Microscopy (TEM), Energy-dispersive X-ray Spectroscopy (EDX) mapping and Scanning Electron Microscopy (SEM) respectively. A FEI aberration-corrected Titan 80-300 TEM was employed to conduct structural investigations in TEM mode, and the typical TEM images are shown in Figure 1(A). SEM Imaging of N-CNT-Pd was conducted with a Leo Gemini II Field Emission Gun Scanning Electron Microscope (Zeiss, Germany) using a detector in in-lens geometry at an acceleration voltage of 5 kV. A suspension of N-CNT-Pd was briefly sonicated in water and then drop cast on a sample holder prior to SEM analysis. The software ImageJ (The National Institute of Health, USA) was employed to analyze the SEM images and determine the size distribution of the N-CNT-Pds.

4.2.4 Cyclic voltammetry (CV) of hydrogen oxidation on the dropcast N-CNT-Pds

A suspension of 4.6×10^{-12} M N-CNT-Pd was prepared by adding 1.2 mg of CNT-Pd to 5 mL chloroform. The suspension was then sonicated for 1 min in a Fisher Scientific FB15050 ultrasonic bath to get a well dispersed solution. A glassy carbon (GC) electrode (diameter: 3.0 mm) was polished with three grades of diamond spray (3, 1 and 0.1 microns) and sonicated in water followed by drying with N_2. 20 μL suspension of N-CNT-Pd was then drop-casted on the GC electrode and left to dry under a N_2 atmosphere. Subsequent cyclic voltammetry was carried out at 298 K in a double Faraday cage with three electrode system using an Autolab potentiostat (Metrohm-Autolab BV, Netherlands). The as-prepared GC electrode was used as the working electrode, an Ag/AgCl electrode (+0.255 V vs. SHE) as the reference electrode and a platinum foil as the counter electrode. 5 mL of aqueous solution containing 0.20 M

KNO_3 was bubbled with H_2 for 10 min to make a H_2-saturated solution before the measurements, and an atmosphere of H_2 was maintained during the experiment. Analogous experiments were also carried out in the same solution but H_2 replaced by N_2.

4.2.5 Voltammetry of hydrogen oxidation on single N-CNT-Pd: chronoamperometry and CV

The voltammetric measurements of hydrogen oxidation on single N-CNT-Pd were conducted with the methods of chronoamperometry and CV. A carbon fibre micro-wire electrode of 7 μm diameter and 1 mm in length was used as the working electrode, together with the same reference electrode and counter electrode as above. The fabrication method of carbon fibre micro wire electrodes has been reported previously.[11] 5 mL of aqueous solution with 0.20 M KNO_3 was bubbled with H_2 for 10 min to get a H_2-saturated solution, and an atmosphere of H_2 was maintained during the experiments. Then a known concentration of solution dispersed N-CNT-Pd was added, following by immediate chronoamperometric or CV scans. The control experiments were carried out in the same solution but H_2 replaced by N_2.

4.3 Results and discussion

4.3.1 Characterization of N-CNT-Pd

The N-CNT-Pds were characterized with TEM (Figure 4.1a, 4.2a and 4.2c), SEM (Figure 4.1b) and EDX mapping (Figure 4.1c) respectively. Tube shaped nanostructures are observed in both the TEM (Figure 4.1a and 4.2a) and SEM images (Figure 4.1b), and highly dispersed spherical Pd nanoparticles on the surface of the nanotube are shown in the TEM image. The diameter distribution of Pd nanoparticles on the nanotube surface is shown in Figure 4.2 with an average diameter of the Pd nanoparticles of 1.37 ± 0.30 nm (43 samples). Typical SEM

images were analysed. The corresponding length and width distribution of N-CNT-Pds are displayed in the Figure 4.3, giving the mean length and width of N-CNT-Pd to be 4.9 ± 4.0 μm (37 samples) and 128.6 ± 58.0 nm (28 samples) respectively. In Figure 4.1c, the EDX maps evidence the presence of the elements C, N, O, Pd on the N-CNT-Pd.

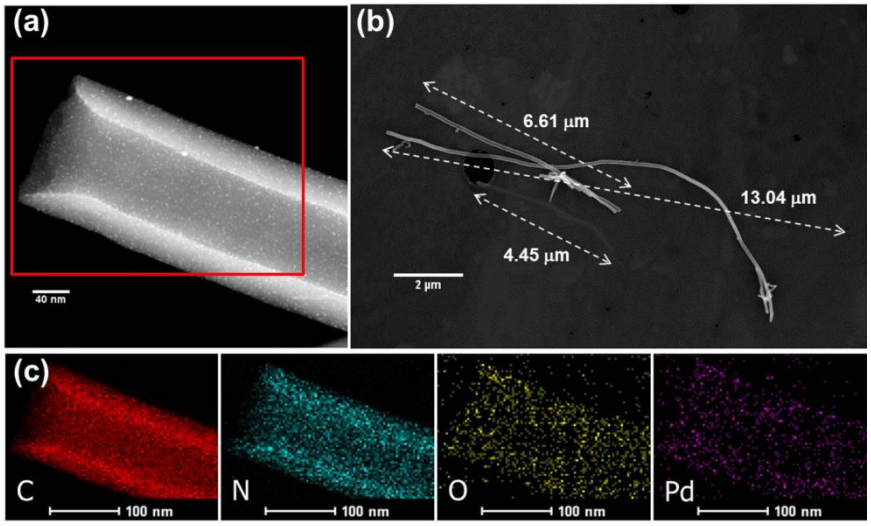

Figure 4.1: (a) TEM, (b) SEM images and (c) EDX maps of N-CNT-Pd.

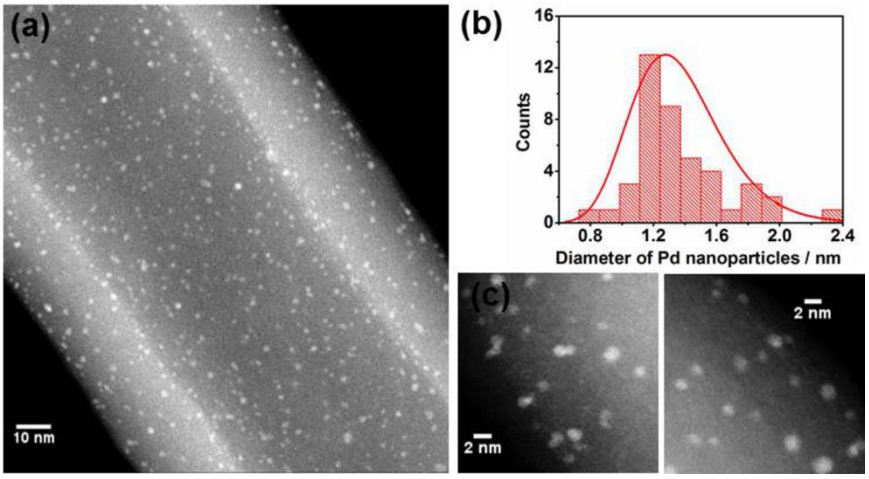

Figure 4.2: (a), (c) TEM images of the N-CNT-Pds and (b) the diameter distribution of the Pd nanoparticles in the image (c), giving the mean diameter of the Pd nanoparticles is 1.37 ± 0.30 nm (43 samples).

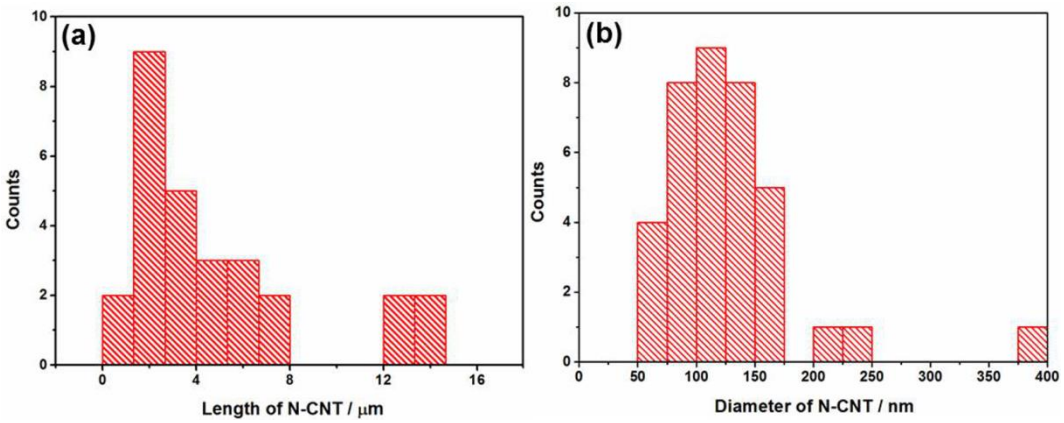

Figure 4.3: The length (a) and width (b) distribution of the N-CNT-Pds from the SEM analysis, giving the mean length and width of the N-CNT-Pds are 4.9 ± 4.0 μm (37 samples) and 128.6 ± 58.0 nm (28 samples) respectively.

4.3.2 CV of hydrogen oxidation on the dropcast N-CNT-Pds

First, the oxidation of hydrogen at the N-CNT-Pd was studied via drop-casting the material onto a GC electrode. As shown in Figure 4.4, in the potential window of study and in a hydrogen saturated solution, 0.77 mM (Henry's law constant: K_{H_2} = 1292 Pa dm^3 mol^{-1}),[12] the bare GC electrode shows no voltammetric feature corresponding to the HOR. A 20 μL suspension of N-CNT-Pd (4.6 × 10^{-12} M) was then drop-cast onto the GC electrode and left to dry under a N_2 atmosphere. Assuming a homogeneous coverage over the surface this amount of material would constitute ~5 layers of carbon nanotubes on the surface. The CV response of the N-CNT-Pds modified electrode was recorded in the presence (blue line) and absence (red line) of saturated hydrogen. The voltammogram shows a quasi-irreversible peak ($E_{mid\text{-}point}$ = -0.348 V vs. Ag/AgCl) for hydrogen oxidation in the presence of saturated hydrogen at the N-CNT-Pd modified electrode. The minimized reductive peak likely reflects the *apparently* sluggish electron transfer kinetics of the redox reaction. The expected half-wave potential for *reversible* hydrogen oxidation in this system can be estimated according to the following expression [13]:

$$exp(\theta_{1/2}) = (\frac{2c^*_{H_2}}{c^\circ})^{1/2} \frac{D_{H_2}}{D_{H^+}}$$

where $\theta_{1/2}$ is the dimensionless half-wave potential of hydrogen oxidation, $c^*_{H_2}$ is the hydrogen bulk concentration, c° is the standard state concentration (equal to 1 M), and D_{H_2} and D_{H^+} are diffusion coefficients (m^2 s^{-1}) for protons and hydrogen gas. The half-wave potential ($\theta_{1/2}$) for hydrogen oxidation is theoretically predicted to occur at -0.194 V vs SHE.[13-15] Therefore, a value of -0.449 V (vs. Ag/AgCl) is estimated for the half-wave potential of hydrogen oxidation in the present work and is marked on the voltammogram in Figure 4.4 (green dashed line). The characteristic potential for a reversible CV is the mid-point potential; however, for the present experimental case the analytically determined half-wave potential provides a close approximation to the predicted reversible mid-point potential,[16] demonstrating that the characteristic oxidative wave observed at the N-CNT-Pds modified electrode in the presence of H_2 results from the oxidation of hydrogen.

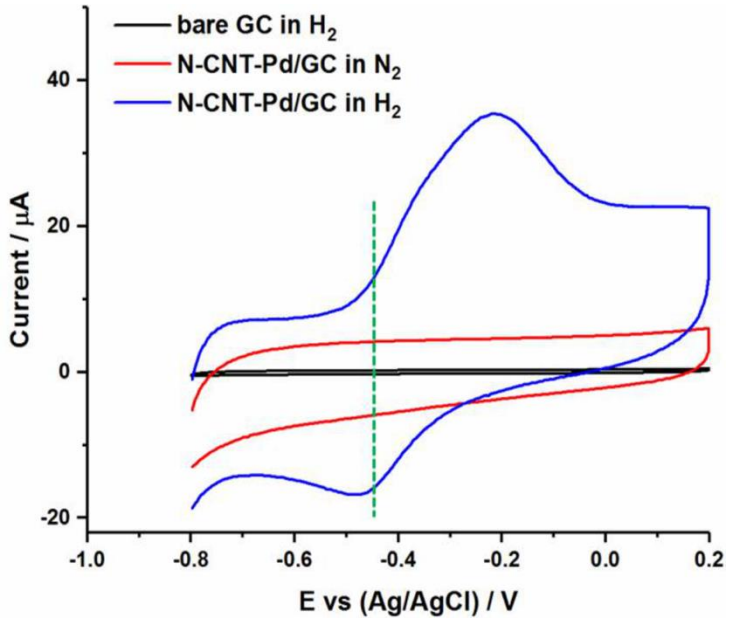

Figure 4.4: Voltammogram of bare GC electrode (d = 3.0 mm) in H_2-saturated KNO_3 (0.20 M) solution (black line); voltammogram of N-CNT-Pd modified GC electrode in 0.20 M KNO_3 solution with (blue line) and without (red line) H_2, 50 mVs^{-1}. Green dashed line represents the reversible half-wave potential ($E_{1/2}$) for HOR (-0.194 V vs SHE).

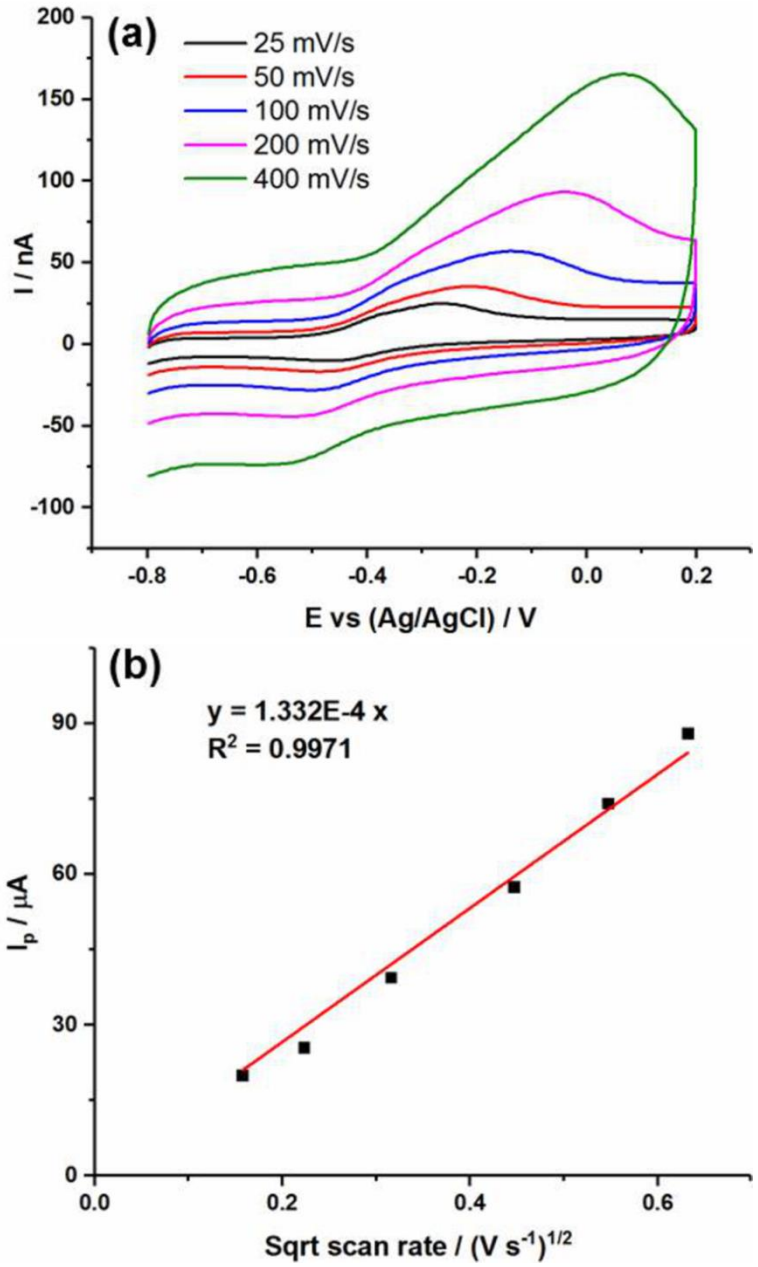

Figure 4.5: (a) CVs of the GC electrode modified with N-CNT-Pds in hydrogen-saturated 0.2 M KNO_3 at different scan rates: 25, 50, 100, 200, 400 mV/s; (b) Plot of oxidative peak current and square root of scan rate.

As shown in Figure 4.5a, CV of the hydrogen oxidation at the dropcast N-CNT-Pds was further investigated at varying scan rate ranging from 25-400 mV/s. The oxidative peak current as a function of scan rate is shown in the Figure 4.5b, where its magnitude was found to scale linearly with the square-root of scan rate. The peak potential is also found to be a

function of scan rate (Figure 4.6). All these features confirm that hydrogen oxidation on the dropcast N-CNT-Pds is a characteristic diffusion controled process.

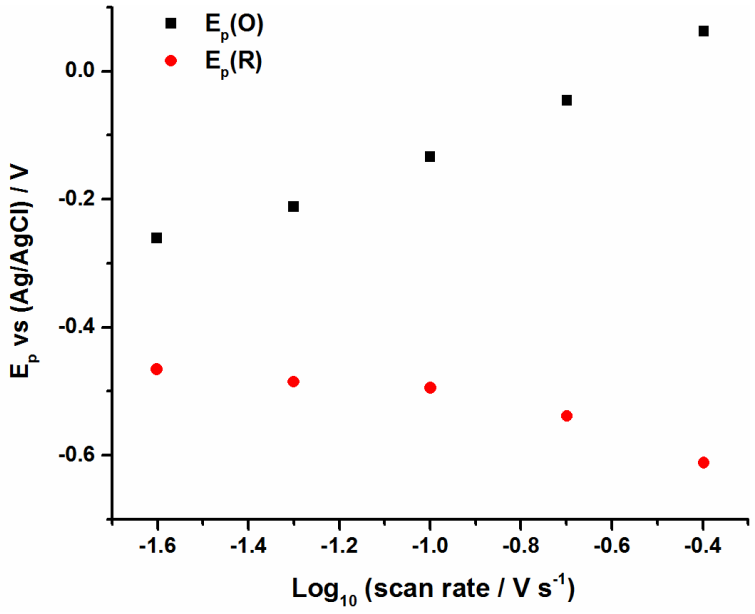

Figure 4.6: Peak potentials of the GC electrode modified with N-CNT-Pds in hydrogen-saturated 0.2 M KNO_3 at different scan rates: 25, 50, 100, 200, 400 mV/s.

Moreover, Tafel analysis (Figure 4.7) gives the value of the transfer coefficient based on:

$$\beta = Tafel\ Slope \times \frac{R\,T}{F}$$

where Tafel slope in Figure 4.7 is 11.75, R is the gas constant (8.314 J mol^{-1} K^{-1}), T is the experimental temperature (298 K) and F is Faraday's constant (96,485 C mol^{-1}). Therefore, the transfer coefficient β is calculated to be 0.30.

The Randles-Sevcik Equation for this irreversible hydrogen oxidation process at 298 K is:

$$I_p = 2.99 \times 10^5\, n \sqrt{\beta}\, D^{1/2}\, [C]\, A\, v^{1/2}$$

where I_p is the peak current, v is the voltage scan rate, $I_p/v^{1/2}$ is given by the slope in Figure 4.5 which equals to 1.33×10^{-4}, n is 2 for this experimental case, β is the transfer coefficient, C is the bulk concentration of H_2 (0.77 mol m^{-3}) and A is the area of the GC electrode (6.975

$\times 10^{-6}$ m^2). Thus, the diffusion coefficient (D) of H_2 is calculated to be 5.72×10^{-9} m^2 s^{-1}, this is in close agreement with the reported literature value of 5.0×10^{-9} m^2 s^{-1}.[17]

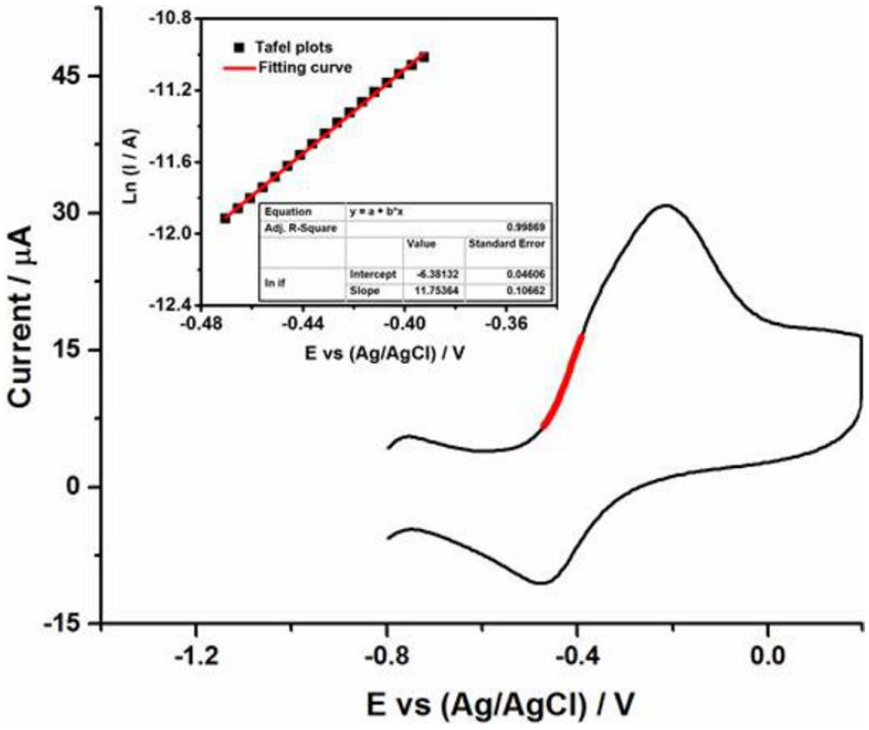

Figure 4.7: CV (blank subtracted) of the GC electrode modified with N-CNT-Pds in hydrogen-saturated 0.2 M KNO_3 at 50 mV/s. Inset: Tafel plot of the highlighted part of the CV.

4.3.3 Chronoamperometry of hydrogen oxidation on single N-CNT-Pd

Having evidenced the ability of the N-CNT-Pd to effectively catalyse the HOR, the work now turns to focus upon the detection of individual impacting carbon nanotubes. A clean carbon fibre microwire (length: ~1 mm; diameter 7 μm) in a H_2-saturated solution containing 0.2 M KNO_3 and 7.0×10^{-14} M N-CNT-Pd. A potential of 0.1 V (vs. Ag/AgCl) was applied to the microwire and the resulting current recorded. In the absence of N-CNT-Pd within the solution the chronoamperometric response showed a monotonic decrease in the current corresponding the capacitative charging of the electrode. In the presence of the carbon

nanotubes and after ~10 chronoamperometric scans had been run clear steps in the current were recorded (Figure 4.8a, b, c, d). This increased current is ascribed to being due to catalysis of the hydrogen oxidation reaction at the carbon fibre surface due to arrival of N-CNT-Pd. Moreover, the sharp onsets (as a function of time) of the current features are strongly indicative of the arrival of single entities at the electrode surface. The transport of the carbon nanotubes from solution to the carbon fibre electrode is taken to occur solely by virtue of Brownian motion, such that, the N-CNT-Pds randomly and stochastically collide with the electrified interface. It was found that once in electrical contact with the electrode, the N-CNT-Pds were relatively stable and remained immobilized for ca. tens of seconds. After an initial impact event repeat chronoamperograms can be recorded exhibiting the catalytic current. Figure 4.8e and f show two chronoamperometric profiles in which the current is observed to step-off, indicating the loss of the catalytic material from the surface.

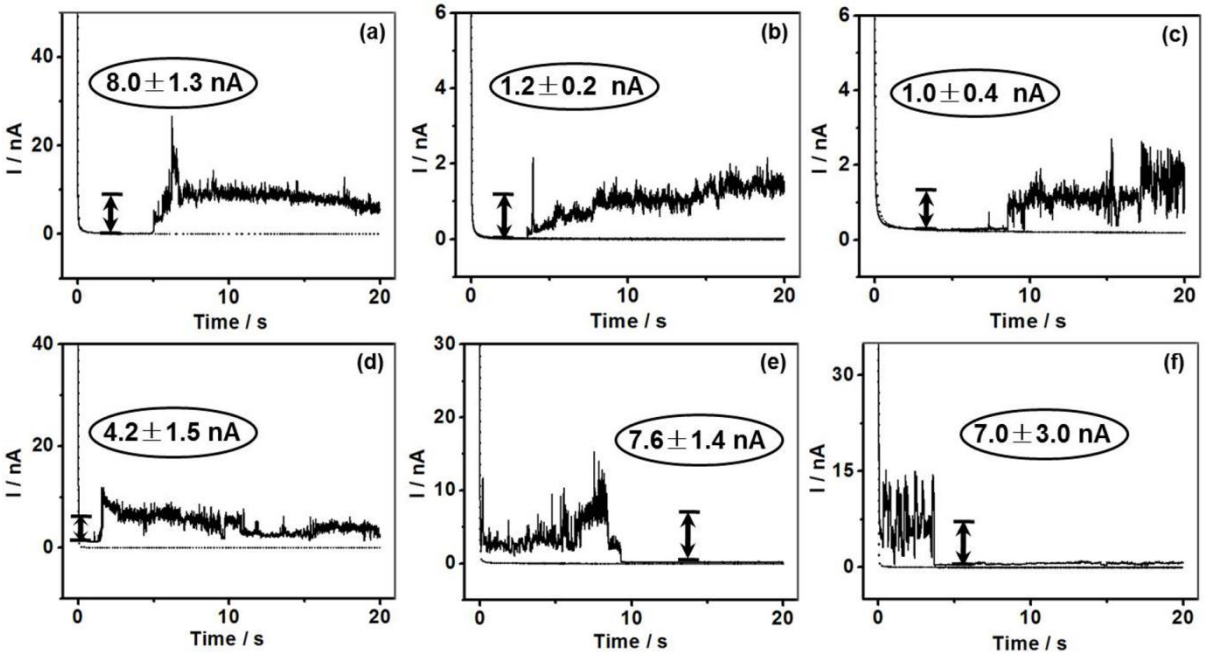

Figure 4.8: Chronoamperometric profiles showing catalytic oxidative Faradaic steps of N-CNT-Pd in 0.77 mM H_2, 0.2 M KNO_3 at 0.1 V (vs. Ag/AgCl). a, b, c and d show the collision of N-CNT-Pd with the wire electrode, while e and f show the falling off of N-CNT-Pd from the wire electrode.

4.3.4 CV of hydrogen oxidation on single N-CNT-Pd

Due to the long residence times (immobilization) of the N-CNT-Pd at the carbon microwire electrode, as evidenced by the duration of the Faradaic 'steps' observed on the chronoamperograms (Figure 4.8), it is possible – after the arrival of the N-CNT-Pd – to experimentally record a cyclic voltammogram at individual CNTs. A known concentration of N-CNT-Pd suspension was added into a H_2-saturated solution containing 0.2 M KNO_3, followed immediately by CV scanning. The CV signals of hydrogen oxidation caused by the collision and immobilization of the N-CNT-Pd was normally observed after a few scans. Figure 4.9 shows six examples (from a total of 30 recorded events) of cyclic voltammograms measured for individual impact events. The scale bars give an indication of the magnitude of the Faradaic current above the background capacitative signal.

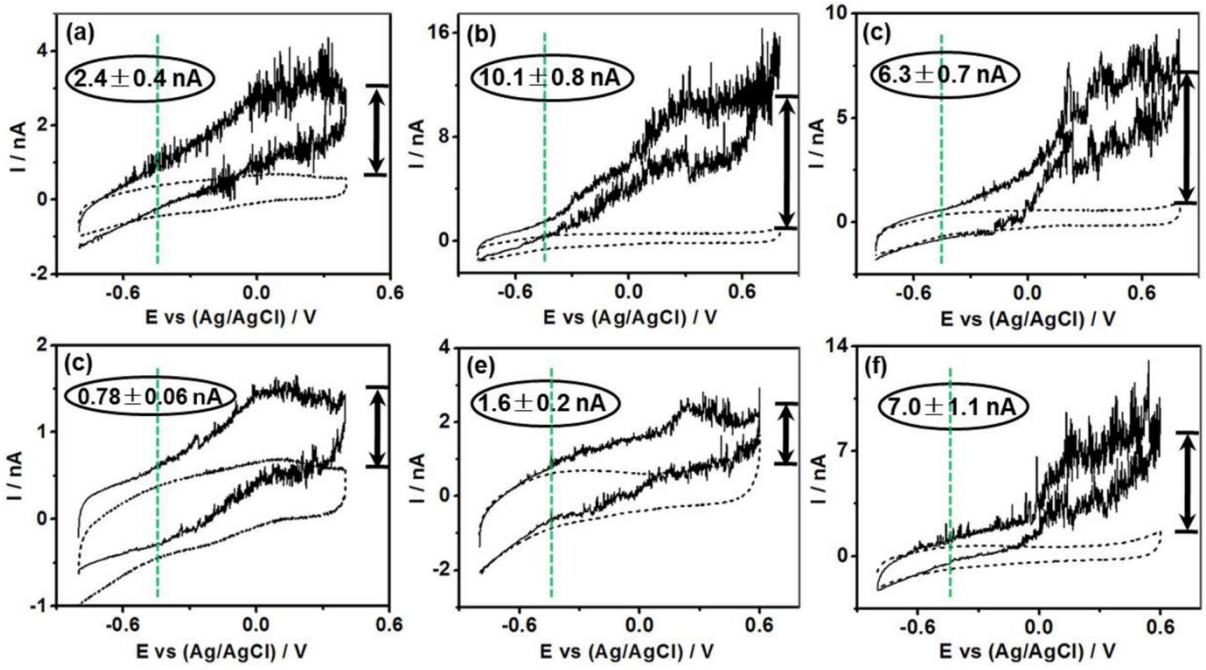

Figure 4.9: Cyclic voltammetric profiles of H_2 (0.77 mM) oxidation in 0.2 M KNO_3 of an immobilised N-CNT-Pd on the carbon fibre micro-wire electrode. Green dashed line depicts the analytically calculated half-wave potential for HOR. Scan rate: 50 mV s^{-1}.

4.3.4 Length comparison: SEM vs single nanotube voltammetry

Modelling the carbon nanotubes as cylindrical electrodes allows the cyclic voltammetric responses to be readily quantitatively analysed.[18] DigiSim was used to simulate the voltammetric response of a fixed carbon nanotube radius of 64 nm by assuming one electron transfer ($a + e^- = b$) and with the concentration of the reactant doubled ([b] = 0.00154 mol L^{-1}), allowing it to be concluded that for each micron in nanotube length ($l = 1 \times 10^{-6}$ m) the expected current for an individual tube is 0.55 nA. Overlay of the experimental (black solid line) and simulated (red dashed line, l = 12 µm) voltammograms is shown in the Figure 4.10.

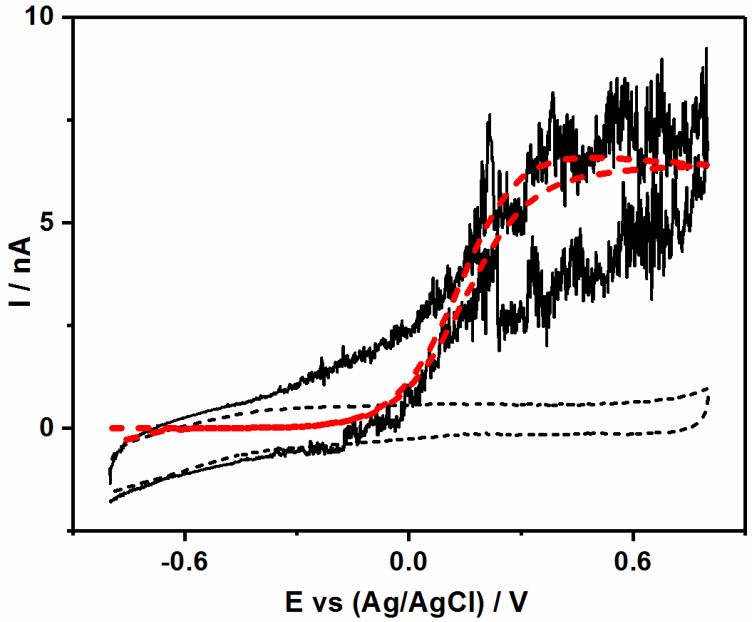

Figure 4.10: Overlay of the experimental cyclic voltammetric profiles (black solid line) of HOR at single N-CNT-Pd and the simulated voltammetric response (red dashed line) for the HOR at a single carbon nanotube of length 12 µm. Black dot line is the blank CV at the wire electrode in the absence of the CNT. Scan rate: 50 mV s^{-1}.

Due to the small Pd interparticle distance on the nanotube surface (cf. the diffusion layer thickness), under diffusion limited conditions the reaction rate will not be sensitive to the surface coverage of the palladium on the carbon nanotubes. Consequently, comparison of the

quasi-steady-state currents measured from cyclic voltammetry of the impacted N-CNT-Pd allows assessment of the nanotube lengths. These electrochemically measured lengths were compared to the data obtained from SEM and the corresponding size distributions are shown in Figure 4.11. The excellent correspondence between the SEM and electrochemical sizing allows the conclusion that the observed impacts are associated with the arrival and immobilization of *individual* N-CNT-Pds at the carbon fibre electrode surface.

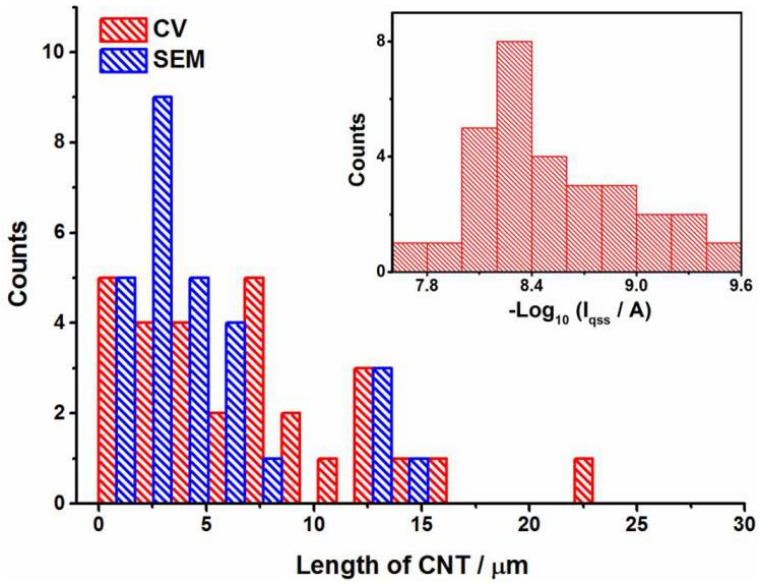

Figure 4.11: Comparison of length distribution of N-CNT-Pd from the CV method (30 samples) and SEM analysis (37 samples). Inset: I_{qss} distribution from 30 CV profiles of single immobilised N-CNT-Pd in 0.77 mM H_2, 0.2 M KNO_3.

4.4 Conclusions

In this chapter, we studied the hydrogen oxidation on single decorated carbon nanotube with the nano-impact method. A facile procedure which enables rapid and easier gathering of single nanoparticle voltammetry was established. Subsequently in the following chapters the 'nano-impacts' method is used to explore the fundamentals of the oxygen reduction reaction

(Chapter 5), the methanol oxidation and formic acid oxidation (Chapter 6) which are at the heart of much energy technology of current interest for example in fuel cells and batteries.

More significantly, it is found that both the chronoamperometic and voltammetric profiles for the single carbon nanotubes exhibit distinct fluctuations in the mediated Faradaic signal. The CVs of the individual tubes evidence that the noise in the current is intimately associated with the Faradaic charge transfer and is *not* capacitative in origin. Due to the magnitude of the currents involved it is unlikely that these fluctuations are due to shot noise associated with the discrete nature of the charge carrier (hydrogen in the present case).[19] Second, the use of multi-walled carbon nanotubes renders it unlikely that the fluctuations arise due to conduction along the length of the tube.[20] Consequently, it is concluded that the electrochemical response reflects the modulation of the mediated current by the contact between the nanotube and electrode surface. This modulation will be presented as a variable and uncompensated resistance on the system, which will serve to distort the voltammetric response and lead to the measurement of apparently slower electron transfer kinetics.

By recording the voltammetry of single carbon nanotubes the stochastic detection and sizing of the material can be readily obtained from the diffusion limited current. However, extraction of meaningful kinetic data will require greater insight into the nanotube/electrode contact. Finally, it is highlighted that, feasibly, the mechanism causing the Faradaic fluctuations may be operative in a range of experimental reports employing drop casted electrodes; the direct observation of the phenomena is only attainable in the present case due to the study of individual carbon nanotubes. Further investigations on the contact of the carbon nanotubes with the electrode are presented in detail in Chapter 7.

References

[1] X. Li, C. Batchelor-McAuley, S. A. I. Whitby, K. Tschulik, L. Shao and R. G. Compton, *Angew. Chem. Int. Ed.*, **2016**, *55*, 4296-4299.

[2] A. J. Bard, H. Zhou and S. J. Kwon, *Isr. J. Chem.*, **2010**, *50*, 267-276.

[3] X. Xiao and A. J. Bard, *J. Am. Chem. Soc.*, **2007**, *129*, 9610-9612.

[4] L. S. Y. Ly, C. Batchelor-McAuley, K. Tschulik, E. Kätelhön and R. G. Compton, *J. Phys. Chem. C*, **2014**, *118*, 17756-17763.

[5] A. R. Jung, S. Lee, J. W. Joo, C. Shin, H. Bae, S. G. Moon and S. J. Kwon, *J. Am. Chem. Soc.*, **2015**, *137*, 1762-1765.

[6] Z. Guo, S. J. Percival and B. Zhang, *J. Am. Chem. Soc.*, **2014**, *136*, 8879-8882.

[7] H. Zhou, J. H. Park, F.-R. F. Fan and A. J. Bard, *J. Am. Chem. Soc.*, **2012**, *134*, 13212-13215.

[8] S. E. F. Kleijn, S. C. S. Lai, M. T. M. Koper and P. R. Unwin, *Angew. Chem. Int. Edit.*, **2014**, *53*, 3558-3586.

[9] M. Kang, D. Perry, Y.-R. Kim, A. W. Colburn, R. A. Lazenby and P. R. Unwin, *J. Am. Chem. Soc.*, **2015**, *137*, 10902-10905.

[10] M. Pumera, *Chem. Eur. J.*, **2009**, *15*, 4970-4978.

[11] J. Ellison, C. Batchelor-McAuley, K. Tschulik and R. G. Compton, *Sens. Actuators, B*, **2014**, *200*, 47-52.

[12] E. Wilhelm, R. Battino and R. J. Wilcock, *Chem. Rev.*, **1977**, *77*, 219-262.

[13] C. Lin, X. Jiao, K. Tschulik, C. Batchelor-McAuley and R. G. Compton, *J. Phys. Chem. C*, **2015**, *119*, 16121-16130.

[14] X. Jiao, C. Batchelor-McAuley, E. Kätelhön, J. Ellison, K. Tschulik and R. G. Compton, *J. Phys. Chem. C*, **2015**, *119*, 9402-9410.

[15] C. Lin, C. Batchelor-McAuley, E. Laborda and R. G. Compton, *J. Phys. Chem. C*, **2015**, *119*, 22415-22424.

[16] H. Ito, Y. Hasegawa and Y. Ito, *Russ J Electrochem*, **2011**, *47*, 1006-1015.

[17] J. V. Macpherson and P. R. Unwin, *Anal. Chem.*, **1997**, *69*, 2063-2069.

[18] C. A. Amatore, B. Fosset, M. R. Deakin and R. M. Wightman, *J. Electroanal. Chem.*, **1987**, *225*, 33-48.

[19] E. Kätelhön, K. J. Krause, B. Wolfrum and R. G. Compton, *ChemPhysChem*, **2014**, *15*, 872-875.

[20] K. Kim, D. Jang, K. Lee, H. Kang, B. Y. Yu, J. I. Lee and G. T. Kim, *Nanotechnology*, **2010**, *21*, 335702.

Chapter 5

New Insights into Fundamental Electron Transfer from Single Nanoparticle Voltammetry

In this chapter, the reductive redox behavior of oxygen in aqueous acid solution leading first to adsorbed superoxide species at single palladium coated multiwalled carbon nanotubes (of length ca. 5 μm and width 130 nm) is reported. The small dimensions of the electroactive surface create conditions of high mass-transport permitting the resolution of electrode kinetic effects. In combination with new theoretical models it is shown that the physical location of the formed product within the double layer of the electrode profoundly influences the observed electron transfer kinetics. This *generically* important result gives new physical insights into the modelling of the many electrochemical processes involving adsorbed intermediates. The work presented here has been published in *Journal of Physical Chemistry Letters*[1] and was performed in collaboration with Ms. Chuhong Lin, Dr. Christopher Batchelor-McAuley, Dr. Eduardo Laborda and Prof. Dr. Lidong Shao. Ms. Chuhong Lin and Dr. Eduardo Laborda carried out all the simulations. Dr. Christopher Batchelor-McAuley helped with the interpretation of the experimental results. Prof. Dr. Lidong Shao performed the synthesis and characterization of the nanomaterials.

5.1 Introduction

Electron transfer at solid/liquid interfaces underpins energy transformation science and technology most notably in fuel cells, solar cells and batteries [2-4]. The rapid and successful development of the latter is vital to solving energy issues across the globe. Whilst useful advances might be made through the semi-empirical investigation of diverse materials [5, 6] it is likely crucial for the essential step changes to emerge that the fundamentals of electron transfer processes at interfaces are much better understood.

Interfacial electron transfer is inevitably coupled with mass-transport and chemical reactions. The relative low rate of diffusion especially in aqueous media, often leads to the masking of both the qualitative and quantitative details of the electron transfer mechanism and kinetics. In order to reveal the latter it is essential to maximize the rate of diffusion of reactants and products to and from the interface. A major advance was realized with the introduction of microelectrodes [7-11] where the reduction in physical size, r, of the electrode impacts the mass-transport coefficient (k_{MT} = D/r; D = diffusion coefficient of the pertinent species). Nevertheless it is clear that the use of nanoscale electrodes offers major further improvement and various possible methods for their construction have been proposed [12-14].

In the last Chapter, we established a procedure for nanoscale voltammetry:[15] an electrode is inserted in an aqueous solution containing the reactants of interest and a dilute suspension of catalytic nanoparticles introduced. Over time a single nanoparticle impacts the electrode and adheres to it for a sufficiently long time for cyclic voltammetry to be conducted on the single adsorbed entity. If the latter is electrocatalytic then voltammetry occurs exclusively on the catalytic nanoparticles and the recorded current-voltage curves give insight into the electron transfer at the nanoparticles/solution interface under mass transport conditions reflecting the single adsorbed particles. This presented technique allows the study

of new nanomaterials, not just the bulk material as commonly found for ultramicroelectrodes,[16] under very high mass transport regimes.

To seek new insights into electron transfer most generally, in this chapter we apply the 'nano-impacts' method to the reduction of oxygen at palladium in aqueous acid. We use nitrogen-doped-multiwalled carbon nanotubes, N-CNT-Pd, (length ca. 5 μm; width 130 nm) covered in Pd nanoparticles (diameter ca. 1.4 nm), as reported in previous chapter.[17] The electronic structure of multi-walled carbon nanotubes is semi-metallic and their conductivity sufficient that no significant potential drop occurs along the length of the nanotube.[18] Herein, the role of the nanotube is assumed to be effectively graphitic in nature and acts solely as a conductive substrate, facilitating electrical connection to the palladium nanoparticles.

The oxygen reduction reaction (ORR) mechanism on metal electrode surfaces is much studied[4, 19-23] but still under debate. Two common system dependent overall routes have been proposed: either a direct four electron reduction to H_2O or a series pathway via two electron transfer to form hydrogen peroxide (H_2O_2) and subsequent reduction of H_2O_2 to H_2O.[24] The ORR on a palladium surface in H_2SO_4 proceeds at least partially via a series pathway.[25-27]

5.2 Experimental section

5.2.1 Chemicals

PR24-LHT carbon nanotubes and palladium nitrate solution (10 wt% $Pd(NO_3)_2$ in 10 wt% HNO_3) were purchased from Pyrograf Products Inc. (Ohio, USA) and Sigma-Aldrich respectively. Sulfuric acid (>95%, H_2SO_4) was acquired from Fisher Scientific (UK) and used as received without further purification. Oxygen (≥99.5%, O_2) and argon (≥99.998%, Ar)

were supplied from BOC, Surrey, U.K. All solutions were prepared with deionised water of resistivity not less than 18.2 MΩ cm (Millipore) at 298 K and degassed with argon before use.

5.2.2 Synthesis and Characterization of N-CNT-Pd

Nitrogen doped carbon nanotubes decorated with palladium nanoparticles (N-CNT-Pd) were prepared by the procedure presented in the previous chapter.

Transmission Electron Microscopy (TEM) and Scanning Electron Microscopy (SEM) were used to characterize the prepared N-CNT-Pds. The typical TEM images of N-CNT-Pd shown in Figure 5.1(a) was collected from a FEI aberration-corrected Titan 80-300 TEM. SEM Imaging of N-CNT-Pd (Figure 5.1(b)) was conducted with a Leo Gemini II Field Emission Gun Scanning Electron Microscope (Zeiss, Germany). ImageJ (The National Institute of Health, USA) was employed to analyze the SEM images.

5.2.3 Cyclic voltammetry of ORR on N-CNT-Pds modified glassy carbon electrode

A glassy carbon (GC) electrode (of diameter ca. 3.0 mm) was polished with three grades of diamond spray (3.0, 1.0 and 0.1 microns) and then sonicated in water and dried with Ar. A suspension of 4.6×10^{-12} M N-CNT-Pd was prepared by adding 1.2 mg of N-CNT-Pd to 5 mL chloroform, following by sonication in a Fisher Scientific FB15050 ultrasonic bath for 1 min. 20 μL N-CNT-Pd suspension was then drop-cast on the GC electrode and left to dry under Ar atmosphere.

Cyclic voltammetry (CV) was then conducted in a double Faraday cage with an Autolab potentiostat (Metrohm-Autolab BV, Netherlands) using three electrode system at 298 K. The modified GC electrode was used as the working electrode, with a saturated calomel electrode

(SCE) as the reference electrode and a platinum foil as the counter electrode. An O_2-saturated solution was then prepared before the measurements by bubbling a 5 mL H_2SO_4 solution (0.5 M) with O_2 for 10 min, and an atmosphere of O_2 was maintained during the experiment. Two analogous experiments were also carried out with the same electrolyte: a bare GC electrode in the O_2-saturated solution and a N-CNT-Pd modified GC electrode in Ar-saturated solution.

5.2.4 Voltammetry of ORR on single N-CNT-Pd: chronoamperometry and CV

For the voltammetric measurements of ORR on single N-CNT-Pd, a carbon fibre microwire electrode (of ca. 7 μm in diameter and ca. 1 mm in length) was used as the working electrode, with the same reference electrode and counter electrode used as above. The fabrication procedure for carbon fibre microwire electrodes was reported in the literature.[28] An O_2-saturated solution was prepared by bubbling a 5 mL H_2SO_4 solution (0.5 M) with O_2 for 10 min, and then a known concentration of N-CNT-Pd suspension was added and bubbled with O_2 for 10 seconds to make a diluted and well dispersed suspension of N-CNT-Pd, followed by immediate chronoamperometric or CV scans. An atmosphere of O_2 was maintained during the experiments.

5.3 Results and discussion

5.3.1 Characterization of N-CNT-Pd

The TEM and SEM images of the N-CNT-Pds are shown in Figure 5.1. The energy-dispersive X-ray spectroscopy maps of N-CNT-Pd, the size information of the carbon nanotubes (4.9 ± 4.0 μm in length and 128.6 ± 58.0 nm in width) and the size distribution of the Pd nanoparticles (1.37 ± 0.30 nm in diameter) were reported in the previous chapter.[15]

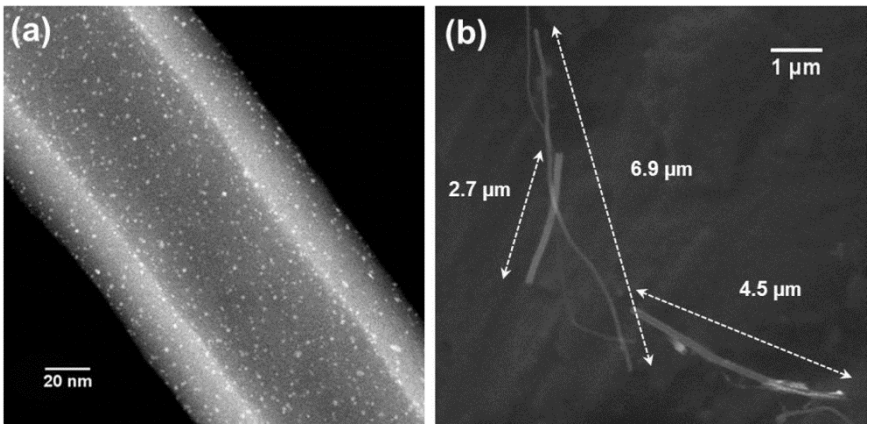

Figure 5.1: (a) TEM image (scale bar 20 nm), (b) SEM image (scale bar 1 µm) of N-CNT-Pd.

5.3.2 CV of ORR on the dropcast N-CNT-Pds

The ability of the N-CNT-Pd to catalyse the ORR was evaluated by drop-casting onto a glassy carbon (GC) macroelectrode (ca. 3.0 mm in diameter). As shown in Figure 5.2(a) (black line), no voltammetric signal from ORR was observed at the bare GC electrode in an O_2-saturated solution. Then the GC electrode was drop-cast with a 20 µL suspension of N-CNT-Pd (4.6×10^{-12} M) and dried under a N_2 atmosphere. Assuming homogeneous coverage over the electrode surface constitutes ~5 layers of carbon nanotubes on the surface. Figure 5.2(a) shows the CV profiles of the N-CNT-Pds modified GC electrode in 0.5 M H_2SO_4 saturated with Ar (red line) and with O_2 (blue line). It was concluded that N-CNT-Pd in combination with a carbon electrode allows the investigation of the O_2 reduction at single N-CNT-Pd tubes via the nano-impact method to which we turn next. The increased reductive current can be ascribed to the catalytic performance of the palladium nanoparticles decorated on the carbon nanotube surface since the nitrogen doped carbon nanotube (N-CNT) without palladium coated does not show an obvious reductive wave (Figure 5.3 red line).

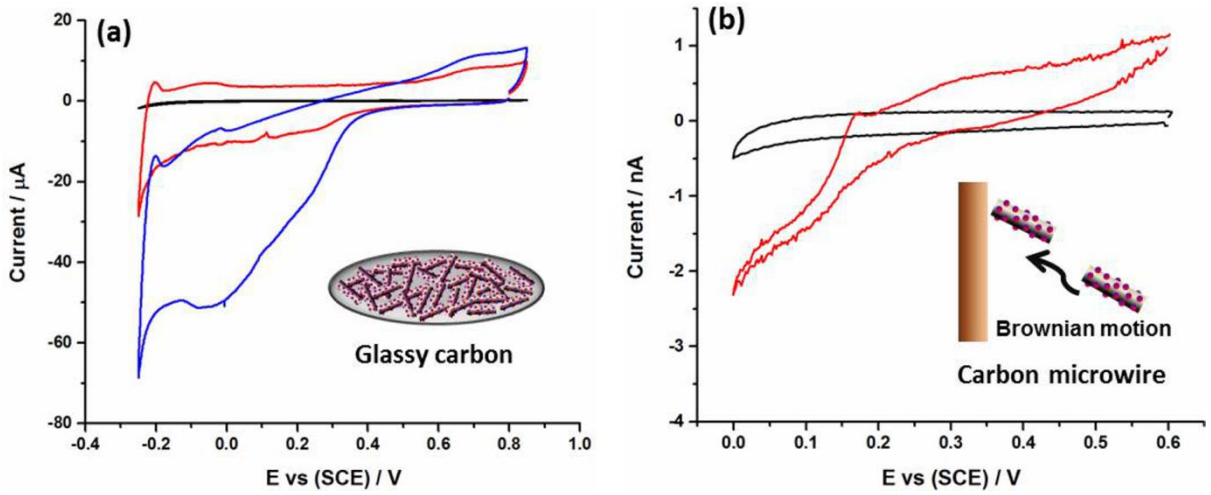

Figure 5.2: (a) Voltammogram of the bare GC electrode (d = 3.0 mm) in 0.5 M H_2SO_4 saturated with O_2 (black line); voltammogram of the N-CNT-Pd modified GC electrode in 0.5 M H_2SO_4 saturated with Ar (red line) and with O_2 (blue line), 50 mV/s. (b) Voltammogram in 0.5 M H_2SO_4 saturated with O_2 of the carbon microwire electrode before (black line) and after (red line) collision and immobilized with N-CNT-Pd.

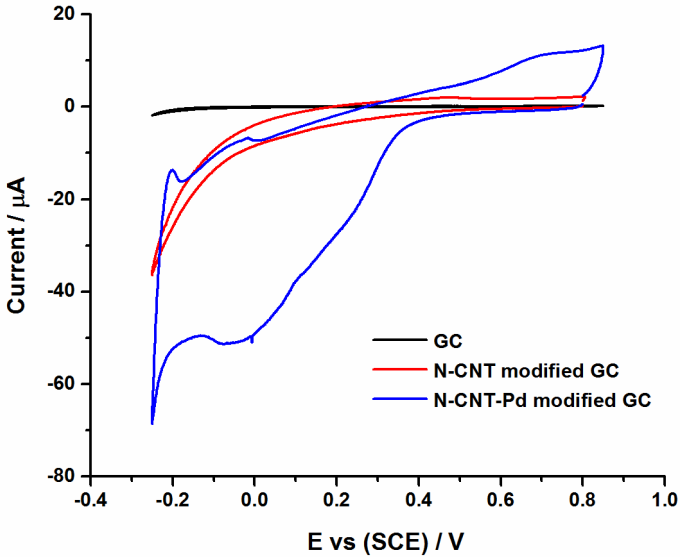

Figure 5.3: Voltammogram of the bare GC electrode (d = 3.0 mm) (black line), N-CNT modified GC electrode (red line), N-CNT-Pd modified GC electrode (blue line) in 0.5 M H_2SO_4 saturated with O_2, 50 mV/s.

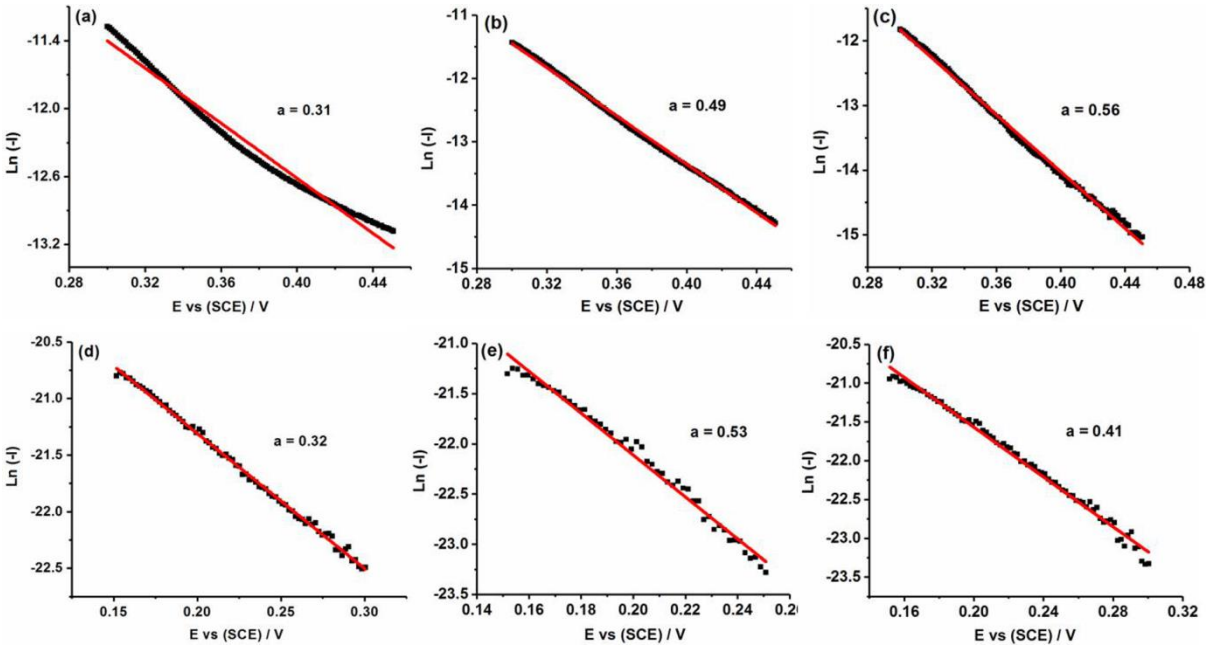

Figure 5.4: Tafel plots of (a) the raw CV of ORR on the N-CNT-Pd modified GC electrode (the blue line in Figure 5.2a), (b) the raw CV after baseline correction, (c) the raw CV after blank subtraction (the red line in Figure 5.2a as a blank); (d) the raw CV of ORR on the single N-CNT-Pd (the red line in Figure 5.2b), (e) the raw CV after baseline correction, (f) the raw CV after blank subtraction (the black line in Figure 5.2b as a blank).

As shown in Figure 5.4, the transfer coefficient was measured by plotting ln|I| for the forward sweep versus E with the data directly from CV experiments (red line in Figure 5.2b) with linear fitting to get the slopes. For more accurate measurement, two background correction strategies including baseline correction and blank subtraction are employed. The resulting value of transfer coefficient varies from 0.31 to 0.56 for the N-CNT-Pd modified GC electrode and from 0.32 to 0.53 for the single N-CNT-Pd depending on the background technique used. This transfer coefficient is consistent with the reported Tafel slopes in the literature where a value of 120 mV dec^{-1} or greater (equivalent transfer coefficient $\alpha \leq 0.49$) is reported for the ORR on Pt(111) supported Pd film electrodes.[25]

5.3.3 Chronoamperometry of ORR on single N-CNT-Pds

Chronoamperometry was carried out with a carbon fiber microwire electrode (of length ca. 1 mm and diameter ca. 7 μm) by recording the current in an O_2-saturated solution containing 0.5 M H_2SO_4 and 1.4×10^{-13} M N-CNT-Pd at a potential of 0.0 V (vs. SCE). Individual impacting single N-CNT-Pd particles were detected and two example chronoamperometric scans with clear steps are shown in Figure 5.5. The increased current as shown in Figure 5.5a is due to the catalysis of ORR at single N-CNT-Pd which collided with and became immobilized on the microwire electrode as evidenced elsewhere.[15] The carbon nanotube transport from solution to the carbon microwire electrode is by virtue of Brownian motion, leading to the random and stochastic collision of the N-CNT-Pds with the electrified interface. Once in electrical contact with the electrode, the N-CNT-Pds were relatively stable and remained immobilized for ca. tens of seconds. After an initial impact event the catalytic current is observed in subsequent chronoamperograms. Figure 5.5b shows a chronoamperometric profile in which the current is observed to step-off, indicating the departure of the catalytic material N-CNT-Pd from the electrode surface.

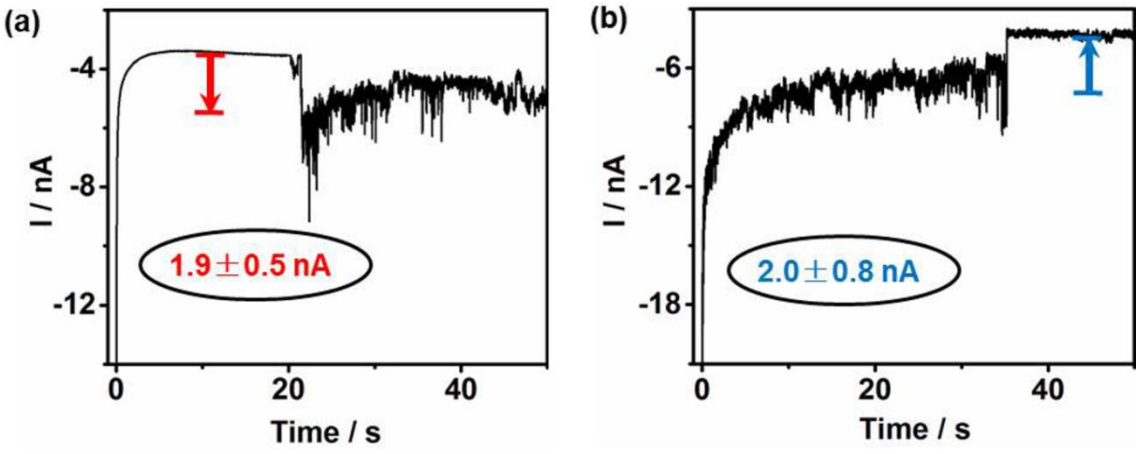

Figure 5.5: Chronoamperometric currents showing catalytic reductive Faradaic steps of N-CNT-Pd in 0.5 M H_2SO_4 saturated with O_2 at 0.0 V (vs. SCE). (a) an example of the collision of N-CNT-Pd with the carbon microwire electrode; (b) an example of the falling off of a N-CNT-Pd from the wire electrode.

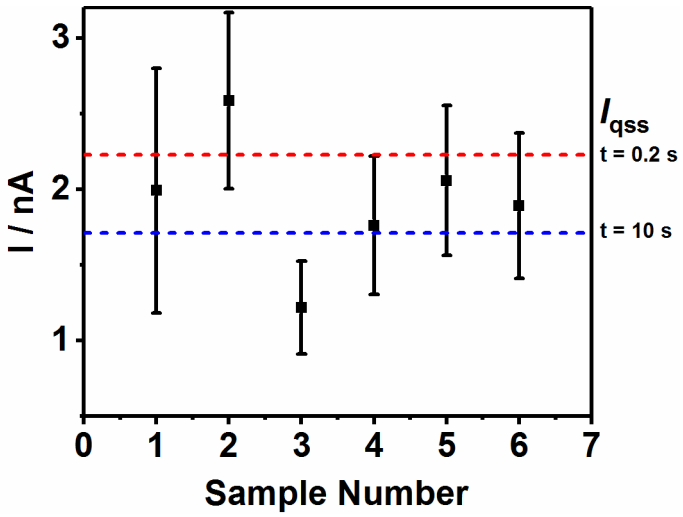

Figure 5.6: Experimental steady-state currents for ORR on the collided N-CNT-Pd, where the red and blue dashed lines represents the theoretical quasi-steady state current for a cylindrical electrode I_{qss} when t = 0.2 s and t = 10 s, where two electrons are transferred in ORR.

Figure 5.6 provides some steady-state currents measured for ORR, which are found to be close to the value of the diffusion-limited currents (the dashed lines) for a two electron transfer process. Calculation of the quasi-steady state current of chronoamperometry on a micro cylinder is carried out based on the following expression:[29]

$$i_{qss} = \frac{4\pi nFDC_0 l}{\ln(\tau)} \quad \tau = \frac{4Dt}{r^2}$$

where n is the number of electron transferred (n = 2), F is the Faraday constant (96485 C mol^{-1}), D is the diffusion coefficient of O_2 (1.96×10^{-9} m^2 s^{-1}),[30] C_0 is the concentration of O_2 (1.23 mM), l is the length of the nanotube (l = 4.9 μm), τ is the dimensionless time parameter where r is the radius of the nanotube (r = 64.3 nm). Thus, the expected quasi-steady state current for t = 0.2 s and 10 s is estimated to be 2.2 nA and 1.7 nA respectively, as shown in the red dashed line and blue dashed line in Figure 5.6. This current range, as shown in Figure 5.6, is consistent with the experimental values (black squares) which are obtained by averaging a few seconds of the steady state current on the chronoamperomograms,

indicating that the ORR on N-CNT-Pd is a two-electron transfer process and except the diffusion, other mass transport effect can be ignored in this experiment.

5.3.4 CV of ORR on single N-CNT-Pds

The current steps observed on the chronoamperograms indicate a residence time of the N-CNT-Pd long enough to permit the recording of a cyclic voltammogram at individual CNTs. Figure 5.2b shows the CV signal of ORR during the initial impact event of N-CNT-Pd which lands on the electrode within a few minutes of adding a known concentration of N-CNT-Pd suspension into an O_2-saturated solution containing 0.5 M H_2SO_4. Note that for the recorded CV profiles the sizes of the current fluctuations are variable between different adsorbed carbon nanotubes. An example of a CV with similar wave as Figure 5.2b but distinct Faradaic current fluctuations is shown in Figure 5.7. The fluctuation of such Faradaic currents observed is explained in detail in Chapter 7.[31]

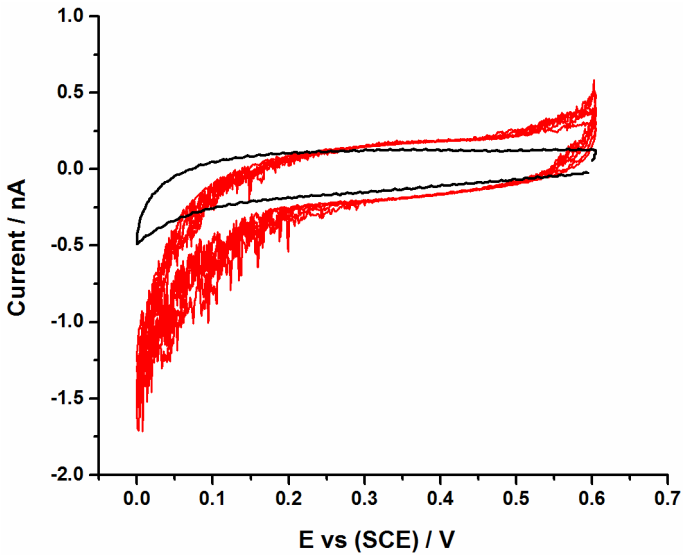

Figure 5.7: Six continuous CVs (red curves) of the carbon microwire electrode during an impact event in O_2 saturated 0.5 M H_2SO_4 with N-CNT-Pd dispersed. The black curve is the CV of the carbon microwire electrode in O_2 saturated 0.5 M H_2SO_4 in the absence of N-CNT-Pd. Scan rate: 50 mV/s.

5.3.5 Comparison: CV of ORR on single N-CNT-Pd vs on its ensembles

For the irreversible process of one electron transfer, the mass transport constant at the voltammetry peak current, m_T, of a planar macro electrode is:[32]

$$m_T = 0.496\sqrt{\alpha}\sqrt{\frac{FDv}{RT}} \tag{5.1}$$

where α is the electron transfer coefficient and 0.43 is taken as a representative value in this work for oxygen, F is the Faraday constant (96485 C mol^{-1}), D is the diffusion coefficient of O_2 (1.96×10^{-9} m^2 s^{-1}),[30] v is the voltage scan rate (0.05 V s^{-1}), R is the gas constant (8.314 J mol^{-1} K^{-1}) and T is the temperature (298 K). Therefore, the mass transport constant of a planar macro electrode, $m_{T(macro)}$, is calculated as 2×10^{-5} m s^{-1}.

While the mass transport constant, $m_{T(CNT)}$, of a single carbon nanotube as a cylindrical micro electrode at the voltammetry peak current is approximately:[33]

$$m_{T(CNT)} = \frac{D}{r_0}(0.446p + 0.335p^{0.15}), \text{ with } p = \sqrt{\frac{Fr_0^2 v}{RTD}} \tag{5.2}$$

where r_0 is the radius of the carbon nanotube (ca. 6.4×10^{-8} m) and the other parameters are as the same as the above. The mass transport constant of the carbon nanotube as a cylindrical micro electrode, is then estimated to be 4×10^{-3} m s^{-1}.

Using the Butler-Volmer equation:

$$i = FAk_0\left\{C_O e^{\left[-\frac{\alpha F\eta}{RT}\right]} - C_R e^{\left[-\frac{(1-\alpha)F\eta}{RT}\right]}\right\} \tag{5.3}$$

where A is the area of the electrode, k_0 is the standard rate constant, C_O and C_R are respectively the concentration of the species O and R at the electrode surface in O + e ↔ R

and η is the overpotential. From this the change in the overpotential due to the altered mass transport can be estimated to be:

$$\frac{m_{T(CNT)}}{m_{T(macro)}} = e^{\left[-\frac{\alpha F}{RT}\left(\eta_{(CNT)}-\eta_{(macro)}\right)\right]} \tag{5.4}$$

Therefore, the overpotential difference, shown as the potential shift in the voltammogram, can be derived from the ratio of $m_{T(CNT)}$ and $m_{T(macro)}$, giving a value of 0.32 V.

The CVs of $S_2O_8^{2-}$ reduction on the above electrodes exhibit the expected large potential shifts relating to the huge difference of the electrode size, as shown in Figure 5.8: The CV of single N-CNT-Pd does not show a clear reduction wave because of the high overpotential of $S_2O_8^{2-}$reduction on it, causing the wave to shift into the region of the solvent decomposition.

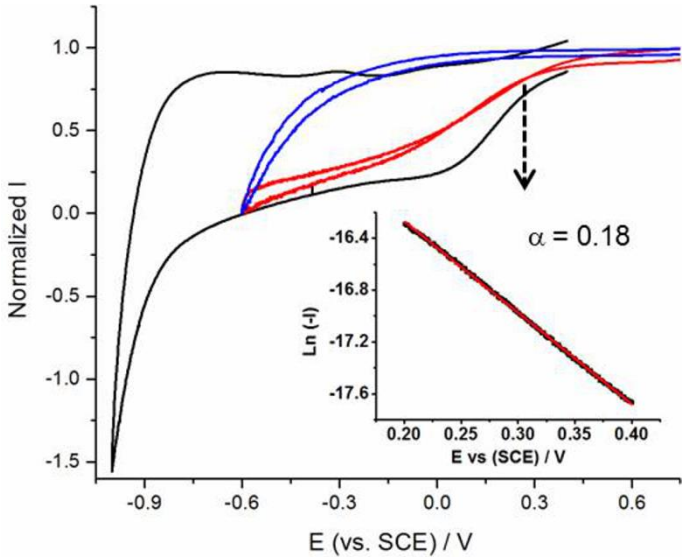

Figure 5.8: Voltammograms of $Na_2S_2O_8$ (3 mM) reduction in 0.5 M K_2SO_4 of the N-CNT-Pd modified GC electrode (black line), of a carbon microwire electrode immobilized with N-CNT-Pd ensembles by immersing in a concentrated suspension of N-CNT-Pd in advance (red line) and of a carbon microwire electrode after collision and immobilized with N-CNT-Pd (blue line). Inset: Tafel plot of the red line.

Figure 5.8 shows a comparison of the CVs of $Na_2S_2O_8$ (3 mM) reduction in 0.5 M K_2SO_4 at the N-CNT-Pd modified GC electrode (black line), at a carbon microwire electrode

immobilized with N-CNT-Pd ensembles by immersing in a concentrated suspension of N-CNT-Pd in advance (red line), and at a carbon microwire electrode after collision and immobilized with N-CNT-Pd (blue line). It is found that the overpotential shifts significantly in terms of the decreasing size of the "electrode", and the CV of single N-CNT-Pd does not even show a clear wave of reduction in the potential range of study because of the high overpotential of $S_2O_8^{2-}$ reduction on it. The Tafel plot shown in inset of Figure 5.8 gives a transfer coefficient of 0.18 for $S_2O_8^{2-}$ reduction on the N-CNT-Pd ensembles.

For the ORR experiments, comparing Figure 5.2a and Figure 5.2b, it is observed that the voltammetric waves shifts negatively about 0.1 V (the quarter-wave potential as the characteristic potential[34]: ~0.3V for modified GC electrode and ~0.2V for the single CNT) when the size of the electrode drops from millimeter scale of GC to sub-micrometer scale of the CNTs. This slight potential shift might reflect the "reversibility" of the first electron transfer step (reduction of O_2 to the superoxide ion). However, this step is usually thought to be the rate-determining step and the low transfer coefficient seen in the CV signal of ORR is commonly believed to signal "electrochemical irreversibility".[35] Under reversible conditions the apparent transfer coefficient of a one-electron transfer is one, and the wave-shape reflects a redox process under Nernstian control not any underlying electron transfer kinetics.

Over the potential range used for Tafel analysis neither transport effects nor substantial changes in k_0 between dropcast ensembles and single nanotubes are expected, therefore the observed kinetic limitation must have a more "complicated" cause. It is necessary to revisit the fundamentals of electron transfer theory in the light of these unexpected data. In particular for reactions where the product of the electron transfer is an adsorbed species, the electrical double layer is expected to have a significant effect on the kinetics of the electron transfer. A model is proposed here to study the effect of the electrical double layer on the

kinetics of the electron transfer in which solution phase oxygen is reduced to adsorbed superoxide ions.[36]

5.3.6 Theory of heterogeneous electron transfer leading to absorbed species including double layer effects

To understand the contradiction, the first electron transfer step in ORR is studied in the simulation. The Gibbs energy surface for the electrochemical reduction of a neutral species (O_2(sol)) to a negatively charged adsorbate ($O_2^{-\cdot}$ (ads)) in eq.(5.5) is calculated and hence the corresponding reaction current can be obtained. Details about the simulation can be found in the appendix of this chapter.[1]

$$X(\text{sol}) + e^- \rightleftharpoons X^{-\cdot}(\text{ads}) \tag{5.5}$$

Figure 5.9 provides an example situation for reaction (5.5). Figure 5.9a is a Gibbs energy surface at the equilibrium potential E_{eq} and the white dashed line shows the minimum energy path. The Gibbs energy surface describes both the adsorption process from X(sol) to $X^{-\cdot}$ (ads) and the change of the charge carried by the redox species. Figure 5.9b shows the minimum energy path, varying as a function of the overpotential $E - E_{eq}$.

As discussed, neither the mass transport process nor the kinetics is the rate-determining factor for ORR in experiment. It is reasonable to assume that the small value of the transfer coefficient is caused by other factors, such as the electrical double layer effect. It is found in Figure 5.9b that the charged species $X^{-\cdot}$ (ads) and the transition state (TS) are more potential-dependent than the neutral reactant X, indicating the sensitivity of these charged species to the electric field within the double layer. Furthermore, the calculated position of $X^{-\cdot}$ (ads) and TS in Figure 5.9b are significantly inside the electrical double layer, which signals the possibly dominant importance of the electrical double layer for the first electron transfer step of ORR.

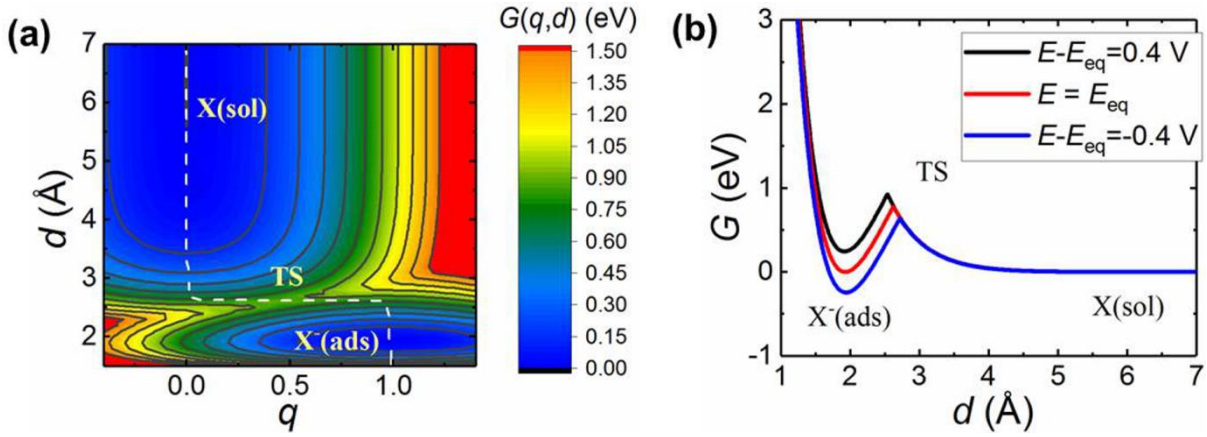

Figure 5.9: Example of the Gibbs energy surface of reaction (5.5): (a) the Gibbs energy surface at the equilibrium potential; (b) reaction paths with different overpotentials on the *d* direction. *q*, *d* are reaction coordinates. -*q* relates to the charge carried by the reacting species and *d* is the distance from the electrode surface. The Debye length (see text) κ^{-1} = 2.0 Å. Other simulating parameters are common for all the simulations in this chapter and can be found in the Appendix.

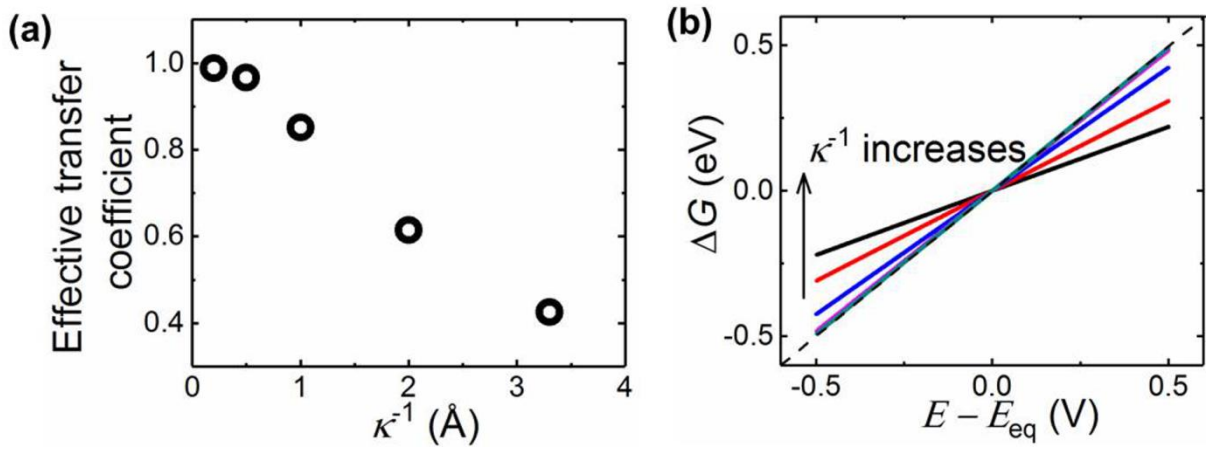

Figure 5.10: Electrochemical responses to the change of Debye length: (a) the effective transfer coefficient calculated at low overpotentials; (b) the hypothetical Gibbs energy difference between X(sol) and $X^{\cdot}$ (ads). The dashed lines represent the Nernstian condition. The Debye lengths are 0.2, 0.5, 1.0, 2.0, 3.3 Å and the standard heterogeneous rate constant k_0 is 1 m s^{-1}.

Figure 5.10 shows the response of reaction (5.5) to the change of the Debye length κ^{-1}. Figure 5.10a shows the effective transfer coefficient as a function of κ^{-1} with a fast standard heterogeneous rate constant k_0. Under reversible Nernstian condition, an ideal effective

transfer coefficient should equal 1 as the relatively large k_0 leads to reversibility of the reaction. However, it is found that even for an artificially fast k_0 (in order to achieve full electrochemical reversibility) as applied in Figure 5.10, the presence of the electrical double layer leads the effective transfer coefficient deviating from 1. Figure 5.10b shows the Gibbs energy difference $G_{X^{-}(ads)} - G_{X(sol)}$ varying as a function of the Debye length, demonstrating that the apparent "irreversibility" inferred from the transfer coefficient can be caused by the decrease of the driving force as a consequence of the interaction between the electric field within the double layer and the charged species participating in the reaction. Similar conclusions were reported that the electrical double layer can affect the driving force and the transfer coefficient based on the classical Frumkin correction which describes the modification of the Butler-Volmer equation by considering (including) the potential at the point where the charged transition state is located.[37-39] However, the charge transfer in the present model does not occur at a fixed distance to the electrode, which provides advancement on the classical Frumkin correction.

5.4 Conclusions

In this chapter, the data obtained at single nanoparticle catalysts has under conditions of extreme rates of mass transport coupled with theoretical modeling, allowed the key insight that the voltammetric characteristics of the ORR at Pd are likely dominated by double layer effects. As a consequence of the proposed model even for fast electron transfer reactions the illusion of slower kinetics is induced. The reduction of oxygen on Pd involves the initial formation of absorbed superoxide $O_2^{-\cdot}$ (ads) with fast electron transfer kinetics but with an apparent transfer coefficient of 0.3~0.5 due to double layer effects arising from the coulombic interactions of the adsorbed superoxide species inside the double layer. This work

provides a feasible and potential way to re-evaluate some of the many electrode processes, many of technological significance, which are thought to include adsorbed species.

Appendix

The ion transfer reaction explored in this chapter is given by:

$$\mathrm{X(sol)} + e^- \rightleftarrows \mathrm{X^-(ads)} \tag{5.5}$$

The change in the Gibbs energy upon the ion transfer will be modelled on the basis of the extension of the Anderson-Newns Hamiltonian presented by Schmickler *et al*[40] and modified by Voth and Koper[41] that can be written in three parts:

$$H = H_{\mathrm{sol}} + H_{\mathrm{el}} + H_{\mathrm{int}} \tag{5.6}$$

where H_{sol} corresponds to the contribution of the solvent and its interaction with the ion, H_{el} accounts for the electronic energy taking into account the interaction between the metallic and reagent's levels, and H_{int} relates to different electrostatic and non-covalent forces (see below). The solvent and electronic Hamiltonians are the same as presented by Schmickler whereas the third component is introduced to account for other forces that the ion experiences as travelling across the electrical double layer.

1. Solvent energy and solvent-reactant interaction

During the charge transfer reaction, the reorganization of solvent molecules surrounding the redox species can be divided into the contribution of fast and slow solvent modes.[42] Here, the reorganization energy related to the fast modes is symbolized as λ_{f} and that of the slow modes is λ. The fast and slow modes represent different sorts of reorientation, which are related to the solvents loosely or strongly interacting with the redox species.[43] The values

of λ_f and λ are equivalent in this model. The fast reorientation process is considered to be faster than the charge transfer rate. Therefore it does not explicitly appear in the Hamiltonian expression (5.7) but it is included in the expression of the reactant energy level ε_a as shown in eq.(5.19).[44]

The slow modes are described as a set of harmonic oscillators and the interaction between these modes and the reactant is assumed to be linear and proportional to the charge of the redox species:[40, 45, 46]

$$H_{sol} = \frac{1}{2}\sum_{v} \hbar\omega_v \left(p_v^2 + q_v^2 \right) + \left(z - n_a \right) \sum_{v} \hbar\omega_v g_v q_v \tag{5.7}$$

where v represents the different phonon modes and ω_v the frequency, p_v and q_v the dimensionless momenta and coordinates, z the charge of the oxidized state (z = 0 in reaction (5.5)), n_a occupation number of the reactant's valence orbital and g_v the coupling between the phonon and the redox centre. The reorganization energy λ is defined as:[47]

$$\lambda = \frac{1}{2}\sum_{v} \hbar\omega_v g_v^2 \tag{5.8}$$

which is assumed to be a constant anywhere in the solution. Thus, the partial desolvation of the ion as approaching the electrode surface is ignored in this chapter.

The coordinate of the slow modes (q_v in eq.(5.7)) is replaced by a single solvent coordinate $q = q_v / g_v$, which not only represents the vibration modes of the solvent molecules in the inner sphere but also refers to the charge carried by the solvent. As the charge of the surrounding solvent is opposite to that of the redox species, for the reaction in eq.(5.5), the range of q during the reaction varies between -1 and 0. In the case that inner-sphere reorganization was also significant, the definition of the reorganization energy of the redox system also includes the inner-sphere contribution.

2. Electrostatic and non-covalent interactions

In order to account for electrostatic and non-covalent interactions between the reactant and the metal electrode and the 'components' (species and electrostatic potential) of the electrical double layer, the model Hamiltonian is modified with the term H_{int}:

$$H_{\text{int}} = (1 - n_{\text{a}}) G_{\text{X\&M}} + n_{\text{a}} G_{\text{X}^{\cdot-}\&\text{M}} \tag{5.9}$$

where $G_{\text{X\&M}}$ includes the components related to the neutral reactant and $G_{\text{X}^{\cdot-}\&\text{M}}$ to the negatively charged product. The Hamiltonian is constructed as a linear switching function.[41]

The electrostatic potential in solution as a function of the distance to the electrode surface is described by the Gouy-Chapman model[48] such that the corresponding contribution to the energy of the negatively charged $X^{\cdot-}$ is calculated as:

$$G_{\text{X}^{\cdot-},\text{EDL}}(d) = -e_0 (E - E_{\text{pzc}}) \exp(-\kappa d) \tag{5.10}$$

where κ is the Debye constant, E is the applied potential on the working electrode, E_{pzc} the potential of zero charge and e_0 is the elementary charge, approximately 1.60×10^{-19} C. The Debye length κ^{-1} in the Gouy-Chapman model is related to the electrolyte concentration in solution. For a 1:1 electrolyte in water, at 298.15K, the relationship between κ^{-1} and the electrolyte concentration c_{el} is described by:[48]

$$\kappa^{-1} = 0.304 c_{\text{el}}^{-1/2} \tag{5.11}$$

Some examples are listed in Table S1. However, it is worth noting that in this simulation, the Debye length is mainly applied as a simulating parameter to describe the structure of the electrical double layer and the relationship between κ^{-1} and c_{el} cannot be quantitatively described by eq.(5.11), as the simulating system which includes a charged adsorbate on the electrode surface does not strictly fit the ideal Gouy-Chapman model. The Debye length

gives an estimation of the thickness of the double layer though the real structure is more complex especially in presence of specific adsorption.

c (mol L^{-1})	κ^{-1} (Å)
10	0.96
1	3.04
0.1	9.62
0.01	30.4

Table 5.1: The Debye length and relative electrolyte concentrations for 1:1 electrolyte in water at 298.15 K.

The potential energy functions considered in this sub-section account for any relevant interaction different from the interactions with the solvent (Section 1), the metal electronic levels (Section 3) and the electrostatic contributions (eq.(5.10)). The interactions between the X and $X^{\cdot-}$ with the metallic, solid electrode and the environment in the electrical double layer include attractive dispersion forces, electron cloud overlap repulsion, displacement/reorientation of species adsorbed on the electrode surface, etc. A detailed, "first-principles" description of the above interactions is complex. Instead, they will be introduced here through Morse-like potentials that enable us to obtain a qualitative, simple and manageable view of the system. In particular, we will assume that in the region next to the electrode the interactions of the ion are predominantly repulsive (eq.(5.12)) and those of the neutral atom can be described by a 'complete' Morse potential (eq.(5.13)):[49]

$$G_{\text{repulsive}} = D_{\text{e}} \exp\left(-a\left(d - d_0\right)\right)^2 \tag{5.12}$$

$$G_{\text{attractive}} = D_{\text{e}} \left\{ \left[1 - \exp\left(-a\left(d - d_0 \right) \right) \right]^2 - 1 \right\} \tag{5.13}$$

where D_{e} is the binding energy for the hypothetical X-metal bond, a is a constant with an approximate value of 1 Å^{-1} and d_0 is the equilibrium bond length.

The image interaction caused by the induced image charge on the electrode surface as the ion approaches the metal is also taken into consideration:[50]

$$G_{\text{X}^-,\text{im}}\left(d \right) = -\frac{1}{4\pi\varepsilon_0}\frac{{e_0}^2}{4d} \tag{5.14}$$

3. Electronic energy

Under the one-electron approximation where a single electron on the reactant is considered, the electronic Hamiltonian is given by:[51]

$$H_{\text{el}} = n_{\text{a}}\varepsilon_{\text{a}}^0 + \sum_{\text{k}} \left(\varepsilon_{\text{k}} n_{\text{k}} + V_{\text{ak}} c^{+} c \right) \tag{5.15}$$

where ε_{a}^0 is the energy of the valence level on the reactant in the absence of interactions and relative to the Fermi level of the electrode (which is taken as the zero reference value), the first sum corresponds to the energy of the k metallic levels (ε_{k}) and the third term relates to the electron exchange between the metal and the electroactive species where V_{ak} is the hopping integral that characterizes the strength of the interaction between the redox system and the electrode and c^{+} and c the creation and annihilation operators. For the case of only one electron considered in the bonding/antibonding orbital, it is not necessary to take into account the spin of this electron.

As a consequence of the interaction between the valence orbital and the metallic levels, the reactant's valence level is broadened and the corresponding density of states is:[52]

$$\rho_{\mathrm{a}}(\varepsilon)=\frac{1}{\pi}\frac{\Delta(d)}{(\varepsilon-\varepsilon_{\mathrm{a}}-\Lambda)^2+\Delta(d)^2} \tag{5.16}$$

such that its occupation probability and electronic energy are given by:

$$n_{\mathrm{a}}(q,d)=\int_{-\infty}^{+\infty} f(\varepsilon)\rho(\varepsilon)\mathrm{d}\varepsilon \tag{5.17}$$

$$G_{\mathrm{el}}=\int_{-\infty}^{+\infty}\varepsilon f(\varepsilon)\rho_{\mathrm{a}}(\varepsilon-\varepsilon_{\mathrm{a}})\,d\varepsilon \tag{5.18}$$

where $f(\varepsilon)$ is the Fermi-Dirac distribution function. Λ and Δ are chemisorption functions; thus, the original energy level is shifted by Λ and broadened by Δ due to the interaction with the electrons in the metal electrode. It is important to note that $\varepsilon_{\mathrm{a}}(q,d)$ corresponds to the 'effective' energy of the valence level relative to the Fermi level and after considering the different interactions with the solvent, the metal electrode and the electrical double layer as discussed in previous sections:

$$\varepsilon_{\mathrm{a}}(q,d)=\varepsilon_{\mathrm{a}}^{0}+\lambda_{\mathrm{f}}q_{\mathrm{X(sol)}}^{2}-2\lambda q-G_{\mathrm{X\&M}}(d)+G_{\mathrm{X^-\&M}} \tag{5.19}$$

Given that the Fermi level is taken as reference, $\varepsilon_{\mathrm{a}}^{0}$ is dependent on the applied potential:

$$\varepsilon_{\mathrm{a}}^{0}=\varepsilon_{\mathrm{a,eq}}+e_0\eta \tag{5.20}$$

where η is the overpotential. Also note that the interaction of the hydrated species X with the fast solvent modes is also included in the expression of the 'effective' electronic energy. However, as the charge carried by the reactant in the present process X is actually 0, the solvation energy $\lambda_{\mathrm{f}}q_{\mathrm{X(sol)}}^{2}$ is effectively zero.

Within the wide-band approximation, the energy broadening parameter Δ is assumed to be independent of the energy level ε. On the other hand, Δ depends on the distance to the electrode surface and it shows an approximately exponential decay:[53]

$$\Delta(d) = \Delta_0 \exp(-\beta d) \tag{5.21}$$

where Δ_0 is the energy broadening at the electrode surface, β is a constant approximately 1 Å^{-1} and z is the position of the centre of the reactant from the electrode surface. Also, in order to get the analytical expression for the electronic energy, a step distribution function is applied instead of the Fermi-Dirac one:

$$f(\varepsilon) = \begin{cases} 1, & \varepsilon_C \le \varepsilon \le \varepsilon_F \\ 0, & \varepsilon > \varepsilon_F \end{cases} \tag{5.22}$$

where ε_C is the bottom of the conduction band and ε_F is the Fermi level.

Under the approximations above mentioned, the following expression is obtained for the electronic energy:

$$G_{el} = n_a(q,d)\varepsilon_a(q,d) + \frac{\Delta(d)}{2\pi} \ln\left(\frac{\varepsilon_a(q,d)^2 + \Delta(d)^2}{\left(\varepsilon_a(q,d) - \varepsilon_C\right)^2 + \Delta(d)^2} \right) \tag{5.23}$$

4. Gibbs energy expression for the whole reaction system

As can be concluded from that discussed in the previous sections, the Gibbs energy for the whole electrochemical system can be expressed as:

$$G_{tot}(q,d) = G_{sol}(q,d) + G_{el}(q,d) + \{1 - n_a(q,d)\} G_{X^- \&M}(d) + n_a(q,d) G_{X\&M}(d) \tag{5.24}$$

Each energy term is given by:

$$G_{X^- \&M}(d) = D_e \left[1 - \exp(-a(d - d_0))\right]^2 - e_0 (E - E_{pzc}) \exp(-\kappa d) + G_{im}(d) \tag{5.25}$$

$$G_{\mathrm{X\&M}}(d) = D_e \exp\left(-2a\left(d - d_0\right)\right) \tag{5.26}$$

$$G_{\mathrm{sol}} = \lambda q^2 - n_{\mathrm{a}}(q,d) \cdot 2\lambda q \tag{5.27}$$

$$G_{\mathrm{el}} = n_{\mathrm{a}}(q,d)\varepsilon_{\mathrm{a}}(q,d) + \frac{\Delta(d)}{2\pi} \ln\left(\frac{\varepsilon_{\mathrm{a}}(q,d)^2 + \Delta(d)^2}{\left(\varepsilon_{\mathrm{a}}(q,d) - \varepsilon_{\mathrm{C}}\right)^2 + \Delta(d)^2} \right) \tag{5.28}$$

The self-consistent orbital energy for the reactant X(sol) is:

$$\varepsilon_{\mathrm{a}}(q,d) = e_0\eta - 2\lambda q - G_{\mathrm{X\&M}}(d) + G_{\mathrm{X^{-}\&M}}(d) \tag{5.29}$$

5. Numerical simulation of the cyclic voltammetry

Gibbs energy surfaces are calculated from eq.(5.24) and the corresponding minimum energy path is determined. On the minimum energy path, there can be one or more local extreme points, which characterize the initial, final and stable intermediate states. The activation energies for the reductive and oxidative processes are calculated from the minimum energy path by:

$$\Delta G_{\mathrm{red}}^{\mathrm{act}} = G_{\mathrm{TS}} - G_{\mathrm{X(sol)}} \tag{5.30}$$

$$\Delta G_{\mathrm{ox}}^{\mathrm{act}} = G_{\mathrm{TS}} - G_{\mathrm{X^{-}(ads)}} \tag{5.31}$$

where G_{TS} is the energy of the transition state, corresponding to the saddle point on the energy surface. $G_{\mathrm{X(sol)}}$ and $G_{\mathrm{X^{-}(ads)}}$ are local energy minima corresponding to the initial state (the reactant) and the finial state (the adsorbate), respectively.

The reaction rate constants are calculated by the following equations:

$$k_{\mathrm{ox/red}} = k_0 \exp\left(-\frac{\Delta G_{\mathrm{ox/red}}^{\mathrm{act}}}{k_{\mathrm{B}}T} \right) \tag{5.32}$$

where k_0 is the pre-exponential term, which is considered as a constant under room temperature. k_B is the Boltzmann constant and T is the absolute temperature. The equilibrium potential E_{eq} is defined as the potential where the reaction rates of the reduction and oxidation processes are equal. Therefore, the activation energies under different applied potentials are defined as:

$$\Delta G_{ox/red}^{act}\left(E-E_{eq}\right)=\Delta G_{ox/red}^{act}\left(E\right)-\Delta G_{ox/red}^{act}\left(E_{eq}\right) \tag{5.33}$$

where $E - E_{eq}$ is the overpotential η.

For the ion transfer reaction, the reaction rate at electrode surface can be described as:

$$j_{X(sol)}=-k_{red}c_{X(sol)}\left(1-\Gamma_{X^{-\cdot}(ads)}\right)+k_{ox}\Gamma_{X^{-\cdot}(ads)} \tag{5.34}$$

$$\frac{\partial\Gamma_{X^{-\cdot}(ads)}}{\partial t}=k_{red}c_{X(sol)}\left(1-\Gamma_{X^{-\cdot}(ads)}\right)-k_{ox}\Gamma_{X^{-\cdot}(ads)} \tag{5.35}$$

where t is the time upon which the perturbation is applied and $\Gamma_{X^{-\cdot}(ads)}$ is the surface coverage of the adsorbed $X^{-\cdot}$ (ads). Here only a monolayer adsorption is considered on the electrode surface. The mass transport of X(sol) in the solution is described by Fick's second law for linear diffusion:

$$\frac{\partial c}{\partial t}=D\frac{\partial^2 c}{\partial z^2} \tag{5.36}$$

where z is the coordinate perpendicular to the electrode surface.

The resulting problem was solved numerically by means of the Newton-Raphson method and according to the alternating direction implicit (ADI) method, the details of which can be found elsewhere.[54] The simulation was written in C++ and simulations were performed

using an Intel(R) Xeon(R) 3.60G CPU and the runtime being approximately 10 minutes *per* voltammogram.

References

[1] X. Li, C. Lin, C. Batchelor-McAuley, E. Laborda, L. Shao and R. G. Compton, *J. Phys. Chem. Lett.*, **2016**, *7*, 1554-1558.

[2] J. Liu, Y. Liu, N. Liu, Y. Han, X. Zhang, H. Huang, Y. Lifshitz, S.-T. Lee, J. Zhong and Z. Kang, *Science*, **2015**, *347*, 970-974.

[3] J. Suntivich, K. J. May, H. A. Gasteiger, J. B. Goodenough and Y. Shao-Horn, *Science*, **2011**, *334*, 1383-1385.

[4] B. C. H. Steele and A. Heinzel, *Nature*, **2001**, *414*, 345-352.

[5] A. Chen and C. Ostrom, *Chem. Rev.*, **2015**, *115*, 11999-12044.

[6] A. Chen and P. Holt-Hindle, *Chem. Rev.*, **2010**, *110*, 3767-3804.

[7] M. A. Dayton, J. C. Brown, K. J. Stutts and R. M. Wightman, *Anal. Chem.*, **1980**, *52*, 946-950.

[8] K. Aoki and J. Osteryoung, *J. Electroanal. Chem.*, **1981**, *122*, 19-35.

[9] M. Kakihana, H. Ikeuchi, G. P. Satô and K. Tokuda, *J. Electroanal. Chem. Interfacial Electrochem.*, **1981**, *117*, 201-211.

[10] C. A. Amatore, M. R. Deakin and M. Wightman, *J. Electroanal. Chem. Interfacial Electrochem.*, **1986**, *206*, 23-36.

[11] M. R. Deakin, R. M. Wightman and C. A. Amatore, *J. Electroanal. Chem. Interfacial Electrochem.*, **1986**, *215*, 49-61.

[12] I. Heller, J. Kong, H. A. Heering, K. A. Williams, S. G. Lemay and C. Dekker, *Nano Lett.*, **2005**, *5*, 137-142.

[13] D.-H. Woo, H. Kang and S.-M. Park, *Anal. Chem.*, **2003**, *75*, 6732-6736.

[14] C. Wang, Y. Chen, F. Wang and X. Hu, *Electrochim. Acta*, **2005**, *50*, 5588-5593.

[15] X. Li, C. Batchelor-McAuley, S. A. I. Whitby, K. Tschulik, L. Shao and R. G. Compton, *Angew. Chem. Int. Ed.*, **2015**, DOI: 10.1002/anie.201509017, n/a-n/a.

[16] J. Heinze, *Angew. Chem., Int. Ed. Engl.*, **1993**, *32*, 1268-1288.

[17] Z. Xin, J. Wang, X. Huang, Y. Yao and L. Shao, *J. Electrochem. Soc.*, **2015**, *162*, H898-H902.

[18] K. Kanghyun, J. Doyoung, L. Kangho, K. Haeyong, Y. Byung Yong, L. Jung Il and K. Gyu Tae, *Nanotechnology*, **2010**, *21*, 335702.

[19] B. Šljukić, C. E. Banks and R. G. Compton, *J. Iran. Chem. Soc.*, **2005**, *2*, 1-25.

[20] P. G. Bruce, S. A. Freunberger, L. J. Hardwick and J. M. Tarascon, *Nat. Mater.*, **2012**, *11*, 19-29.

[21] P. Hartmann, C. L. Bender, M. Vračar, A. K. Dürr, A. Garsuch, J. Janek and P. Adelhelm, *Nat. Mater.*, **2013**, *12*, 228-232.

[22] Y. Nie, L. Li and Z. Wei, *Chem. Soc. Rev.*, **2015**, *44*, 2168-2201.

[23] I. Katsounaros, W. B. Schneider, J. C. Meier, U. Benedikt, P. U. Biedermann, A. Cuesta, A. A. Auer and K. J. J. Mayrhofer, *Phys. Chem. Chem. Phys.*, **2013**, *15*, 8058-8068.

[24] A. Damjanovic, M. A. Genshaw and J. O. Bockris, *J. Chem. Phys.*, **1966**, *45*, 4057-4059.

[25] V. Climent, N. M. Marković and P. N. Ross, *J. Phys. Chem. B*, **2000**, *104*, 3116-3120.

[26] M. Gara, E. Laborda, P. Holdway, A. Crossley, C. J. V. Jones and R. G. Compton, *Phys. Chem. Chem. Phys.*, **2013**, *15*, 19487-19495.

[27] A. Schneider, L. Colmenares, Y. E. Seidel, Z. Jusys, B. Wickman, B. Kasemo and R. J. Behm, *Phys. Chem. Chem. Phys.*, **2008**, *10*, 1931-1943.

[28] J. Ellison, C. Batchelor-McAuley, K. Tschulik and R. G. Compton, *Sens. Actuators, B*, **2014**, *200*, 47-52.

[29] A. Szabo, D. K. Cope, D. E. Tallman, P. M. Kovach and R. M. Wightman, *J. Electroanal. Chem. Interfacial Electrochem.*, **1987**, *217*, 417-423.

[30] P. Han and D. M. Bartels, *J. Phys. Chem.*, **1996**, *100*, 5597-5602.

[31] H. Hodson, X. Li, C. Batchelor-McAuley, L. Shao and R. G. Compton, *J. Phys. Chem. C*, **2016**, *120*, 6281-6286.

[32] R. G. Compton and C. E. Banks, *Understanding Voltammetry, 2nd edn.*, Imperial College Press, London, **2011**.

[33] K. Aoki, K. Honda, K. Tokuda and H. Matsuda, *J. Electroanal. Chem. Interfacial Electrochem.*, **1985**, *182*, 267-279.

[34] L. Meites, P. Zuman and H. W. Nurnberg, *Pure Appl. Chem.*, **1985**, *57*, 1491.

[35] S. Fletcher, *J. Solid State Electrochem.*, **2008**, *13*, 537-549.

[36] M. H. Shao, P. Liu and R. R. Adzic, *J. Am. Chem. Soc.*, **2006**, *128*, 7408-7409.

[37] A. N. Frumkin, O. A. Petry and N. V. Nikolaeva-Fedorovich, *Electrochim. Acta*, **1963**, *8*, 177-192.

[38] C. P. Smith and H. S. White, *Anal. Chem.*, **1992**, *64*, 2398-2405.

[39] M. Soestbergen, *Russ J Electrochem*, **2012**, *48*, 570-579.

[40] W. Schmickler, *J. Electroanal. Chem.*, **1986**, *204*, 31-43.

[41] M. T. M. Koper and G. A. Voth, *Chem. Phys. Lett.*, **1998**, *282*, 100-106.

[42] R. A. Marcus, *Annu. Rev. Phys. Chem.*, **1964**, *15*, 155-196.

[43] A. Declemy, C. Rulliere and P. Kottis, *Laser Chem.*, **1990**, *10*, 413-429.

[44] W. Schmickler, *Chem. Phys. Lett.*, **1995**, *237*, 152-160.

[45] R. A. Marcus, *J. Chem. Phys.*, **1965**, *43*, 679-701.

[46] N. S. Hush, *J. Chem. Phys.*, **1958**, *28*, 962-972.

[47] E. Santos, M. T. M. Koper and W. Schmickler, *Chem. Phys.*, **2008**, *344*, 195-201.

[48] A. J. Bard and L. R. Faulkner, *Electrochemical Methods: Fundamentals and Applications*, Wiley, **2000**.

[49] J. M. Savéant, *Acc. Chem. Res.*, **1993**, *26*, X1-460.

[50] J. O. M. Bockris, A. K. N. Reddy and M. E. Gamboa-Aldeco, *Modern Electrochemistry 2A: Fundamentals of Electrodics*, Springer US, **2000**.

[51] D. M. Newns, *Phys. Rev.*, **1969**, *178*, 1123-1135.

[52] P. W. Anderson, *Phys. Rev.*, **1961**, *124*, 41-53.

[53] M. T. M. Koper and G. A. Voth, *J. Chem. Phys.*, **1998**, *109*, 1991-2001.

[54] R. G. Compton, E. Laborda and K. R. Ward, *Understanding Voltammetry: Simulation of Electrode Processes*, Imperial College Press, **2013**.

Chapter 6

Improving Formate and Methanol Fuels: The Catalytic Activity of Single Pd Coated Carbon Nanotubes

In this chapter, the oxidation of formate and of methanol on nitrogen doped carbon nanotubes decorated with palladium nanoparticles are studied at both the single nanotube and ensemble levels. Significant voltammetric differences were seen. In particular, Pd oxide formation as a competitive reaction with formate or methanol oxidation is significantly inhibited at high overpotentials under the high mass transport conditions associated with single particle materials in comparison with that seen with ensembles where slower diffusion prevails. Higher electro-oxidation efficiency for the organic fuels is achieved. The work has been published in *ACS Catalysis*[1] and was carried out in collaboration with Miss Hannah Hodson, Dr. Christopher Batchelor-McAuley and Prof. Dr. Lidong Shao. Miss Hannah Hodson collected some experimental data. Dr. Christopher Batchelor-McAuley helped with the interpretation of the experimental results. Prof. Dr. Lidong Shao performed the synthesis and characterization for the carbon nanotubes.

6.1 Introduction

Increased interest in alternative fuel sources has led to the separate application of both formate and methanol in fuel cells. Their use as power sources is appealing due to their high energy density, ease of transportation and storage in contrast to hydrogen fuel cells.[2-6] Pd-based materials have been intensively studied as superior and cost-effective electro-catalysts in the oxidation of both formate and methanol.[7] For formate oxidation, it has been suggested that Pd-based catalysts have a better performance when compared with Pt as the catalytic reactions on Pd follow a direct pathway and no poisoning intermediates are produced.[8, 9] Pd-based materials are also considered to be better catalysts in alkaline media for methanol oxidation than Pt-based materials owing to their improved kinetics and, again, lower poisoning from adsorbed intermediates.[10] However, the instability of the Pd-based catalysts can lead to relatively low energy transformation efficiency.[11, 12] Improving the electro-catalytic stability remains a critical obstacle in the development of Pd-based electrocatalysts in both formate and methanol fuel cells, and the fundamental understanding of Pd deactivation due to its high surface sensitivity is still incomplete.[7, 13]

The electro-catalytic behaviour of newly produced materials are commonly assessed by dropcasting the catalysts onto electrode surfaces and then performing electrochemical tests to analyse their performance. However, the interpretation of such a multilayered, porous drop-cast surface is complex and hard to analyse.[14-20] Moreover, the most commonly used type of electrode in these studies is macro-electrodes at which the mechanism and kinetics can be masked by the limited, slow mass transport conditions.

In this chapter, we report the development of an improved electrode modification method by modifying a carbon microwire electrode in-situ with well-separated individual catalyst entities. This modification is achieved by inserting the wire electrode in a very dilute suspension of the nitrogen doped carbon nanotubes decorated with palladium nanoparticles

(N-CNT-Pd). Also present in the solution is the redox species of interest (formate or methanol). Over a period of time individual catalyst entities (N-CNT-Pd) continuously and randomly collide with the wire electrode due to their Brownian motion. Some of the N-CNT-Pd become immobilised on the electrode surface forming a layer of low coverage. After immobilisation the voltammetric response of the modified electrode is recorded in the same solution. In addition to these surface modification studies, a single particle electrochemical method based on "nano-impacts" was applied. This technique relies on the random collision of individual nanoparticles with a potentiostated electrode where control of the potential leads to mediated electron transfer on the surface of impacting nanoparticle.[1, 21-27] The current amplification from mediated electron transfer is analysed and can be applied to the fundamental mechanisms and dynamics of electrochemical processes at the single entity level.[28] In this chapter, formate oxidation on individual impacting N-CNT-Pd was studied with the nano-impact method. The above methods including both in-situ modification and the nano-impact experiments lead to the spatial isolation of the catalyst particles on the electrode surface creating high mass transport conditions for the oxidation processes, which provide new insights into the electro-catalytic mechanisms of formate and methanol oxidation on palladium, and how this is influenced by mass transport.

6.2 Experimental section

6.2.1 Chemicals

Sodium formate (≥98%), methanol (99.99 %), $NaClO_4$ and NaOH were received from Sigma-Aldrich. Nitrogen gas (N_2) was supplied from BOC, Surrey, U.K. All solutions were prepared with deionised water of resistivity not less than 18.2 MΩ cm (25^{o}C, Millipore).

Preparation and characterization of nitrogen doped carbon nanotubes decorated with palladium nanoparticles (N-CNT-Pd) are shown in previous chapters.[28, 29]

6.2.2 Cyclic voltammetry of formate and methanol oxidation on N-CNT-Pds modified glassy carbon electrode

A suspension of N-CNT-Pd (9.2×10^{-12} M) was prepared by adding 2.4 mg of N-CNT-Pd to 5 mL chloroform, following by sonication in a Fisher Scientific FB15050 ultrasonic bath for 1 min. A glassy carbon (GC) macro-electrode (d = 3.0 mm) was polished with three grades of diamond spray (3.0, 1.0 and 0.1 μm) and then sonicated in water and left to dry under N_2 atmosphere. The as-prepared N-CNT-Pd suspension was then drop-cast on the GC electrode and dried under N_2 atmosphere.

Electrochemical measurements were conducted in a double Faraday cage with an Autolab potentiostat (Metrohm-Autolab BV, Netherlands) using three electrode system at 298 K. For the drop-cast experiments, the modified GC electrode was used as the working electrode, with a platinum foil and a saturated calomel electrode (SCE) as the counter electrode and the reference electrode respectively. Before the measurements a solution containing 5 M formate and 5 M $NaClO_4$ (or 10 M methanol and 1 M NaOH) was bubbled with N_2 for 10 min to remove dissolved O_2, and atmosphere of N_2 was maintained during the experiment. Two control experiments were carried out: an unmodified GC electrode in 5 M formate + 5 M $NaClO_4$ (or 10 M methanol + 1 M NaOH) and a modified GC electrode in 5M $NaClO_4$ (or 1 M NaOH).

6.2.3 CV of formate and methanol oxidation on the carbon microwire electrode in-situ modified with N-CNT-Pd and the nano-impact experiments

In the in-situ modification experiments, the working electrode was carbon fibre microwire electrodes (of ca. 7 μm in diameter and ca. 1 mm in length) which were fabricated according to the procedure introduced in the literature.[30] Formate or methanol solution was degassed with N_2 for 10 min, and then a known concentration of N-CNT-Pd suspension was added and bubbled with N_2 for 30 seconds to make a well dispersed and diluted suspension of N-CNT-Pd. CV was recorded immediately after a clean carbon microwire electrode was inserted in the suspension containing formate or methanol and after the electrode was in-situ modified in the same solution for certain time. The nano-impact experiments were conducted by scanning chronoamperometry immediately after a clean carbon microwire electrode was inserted in the above solutions. For counting and analysis of the current spikes, the software called "SignalCounter" was used.[31]

6.3 Results and discussion

We first investigate the cyclic voltammetry (CV) of formate and methanol oxidation on glassy carbon (GC) electrodes dropcast with N-CNT-Pd to evidence the catalytic ability of the N-CNT-Pd towards these oxidation processes. Mechanistic considerations are made. Second we measure and analyse the CV of first formate and second methanol oxidation on carbon microwire electrodes which have been modified in-situ with individual spatially well-separated N-CNT-Pd tubes via their random collision and immobilization on the wire electrode. Third nano-impact experiments are conducted by recording chronoamperometry at

a carbon microwire electrode in an aqueous suspension of N-CNT-Pd in the presence of formate. Current spikes in the chronoamperograms resulting from formate oxidation on *individual* (single) impacting N-CNT-Pd are detected and analysed. Similar experiments are attempted for the oxidation of methanol. Finally, the results from all the experiments are compared and chemical mechanisms inferred and discussed.

6.3.1 Cyclic voltammetry of drop-cast Pd nanoparticle decorated carbon nanotubes

The cyclic voltammetric responses of formate and methanol oxidation were separately investigated on N-CNT-Pd modified GC electrodes (of ca. 3.0 mm in diameter). To study the formate oxidation, an *unmodified* GC electrode was first voltammetrically scanned in an aqueous solution containing 5 M $NaClO_4$ and 5 M formate. No voltammetric signal was observed, as shown in Figure 6.1a (dotted line). Subsequently 0.96 µg N-CNT-Pd was drop-cast onto the GC electrode and left to dry under a N_2 atmosphere. The amount of N-CNT-Pd dropcast in the experiment corresponds to a coverage of ~1 monolayer assuming the CNTs are perfectly tessellated on the electrode surface (see section 1 and 2 of the appendix of this chapter). In reality a tangled, irregular multilayer is likely formed. Figure 6.1a shows the CV of the above modified GC electrode in 5 M $NaClO_4$ in the absence (dashed line) and presence (solid line) of 5 M formate respectively. The CV of the modified GC electrode in the formate solution shows a clear formate oxidation peak at -0.08 V vs. SCE and a back anodic peak at around -0.02 V vs. SCE (solid line). No oxidation feature was observed in the absence of formate (dashed line). The formate oxidation is known to be highly surface sensitive and at high overpotentials it is inhibited by the formation of a palladium oxide layer.[7, 12] It has been suggested that on the reverse scan the reduction of the oxide layer leads to the recommencement of the electrochemical process.[12]

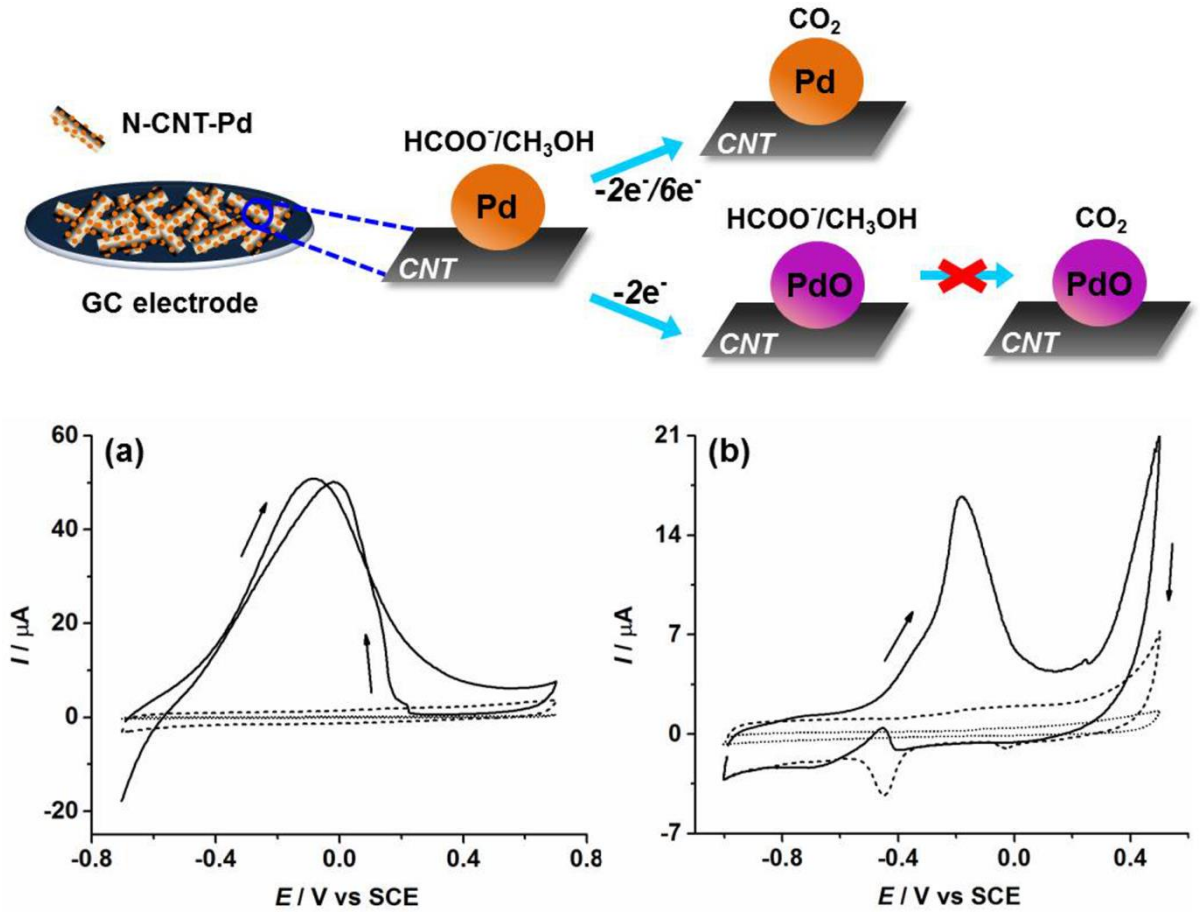

Figure 6.1: (a) Voltammograms of a GC electrode (d = 3.0 mm) modified with 0.96 µg of N-CNT-Pd recorded in 5 M $NaClO_4$ (aq) in the absence (dashed line) and presence (solid line) of 5 M formate. Also shown is the voltammetic response of the bare GC electrode in 5 M $NaClO_4$ + 5 M formate (dotted line). Scan rate: 50 mV s^{-1}. (b) Voltammograms of a GC electrode (d = 3.0 mm) modified with 1.20 µg of N-CNT-Pd in 1 M NaOH (aq) in the absence (dashed line) and presence (solid line) of 10 M methanol. Also shown is the voltammetric response of the bare GC electrode in 1 M NaOH + 10 M methanol (dotted line). Scan rate: 50 mV s^{-1}.

In order to characterize the palladium oxidation process, the voltammetric response of a bulk palladium microelectrode (radius = 5.4 µm) was recorded in the absence of formate. The CV (black line in Figure 6.2a) in 5 M $NaClO_4$ shows a pair of asymmetric redox peaks for Pd oxide formation and reduction: a broad Pd oxidation wave on the forward scan and a sharp peak for Pd oxide reduction on the backward scan. The reduction of the Pd oxide is found to

occur at ~0.0 V vs. SCE. This potential is comparable to the peak potential of formate oxidation (-0.08 V vs. SCE) as recorded on the dropcast N-CNT-Pd (solid line in Figure 6.1a). On the reverse scan of the voltammetry of formate oxidation at a dropcast N-CNT-Pd electrode, a sharp increase of the oxidation current is observed (solid line in Figure 6.1a). This sharp increase in current is found to occur at the potentials of Pd oxide reduction where Pd active sites are released.[12] This observation further evidences that the decrease of the oxidation current on the forward scan is caused, at least in part, by the formation of a Pd oxide layer.

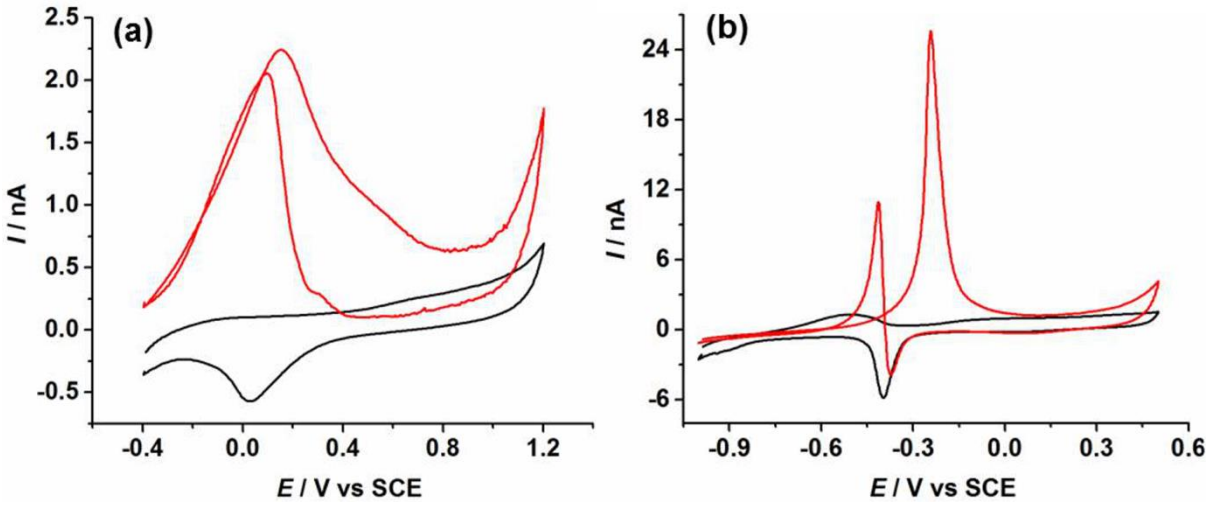

Figure 6.2: (a) Voltammograms of Pd microelectrode (r = 5.4 μm) in 5 M $NaClO_4$ in the absence (black line) and presence (red line) of 0.5 M formate. Scan rate: 50 mV s^{-1}. (b) Voltammograms of Pd microelectrode (r = 5.4 μm) in 1 M NaOH in the absence (black line) and presence (red line) of 0.5 M methanol. Scan rate: 50 mV s^{-1}.

We next consider the oxidation of methanol at a N-CNT-Pd modified GC electrode and at the Pd microelectrode. Voltammograms are shown in Figure 6.1b and Figure 6.2b respectively. The results for methanol oxidation mirror those found for formate. An anodic peak was observed at -0.18 V vs. SCE on the modified GC electrode in 1 M NaOH

containing 10 M methanol (solid line in Figure 6.1b), and a small oxidation peak on the backward scan at around -0.45 V vs. SCE. In the absence of methanol, the voltammetric response of both the dropcast N-CNT-Pd (dashed line in Figure 6.1b) and the Pd microelectrode (black line in Figure 6.2b) demonstrate that Pd oxide reduction occurs near -0.4 V vs. SCE in 0.1 M NaOH. This value of -0.4 V is more negative than the peak potential for methanol oxidation (-0.18 V vs. SCE) on the dropcast N-CNT-Pd (solid line in Figure 6.1b). Hence, a significant surface coverage of Pd oxide has probably formed before the methanol oxidation peak current, and the further deactivation of the Pd active sites lead to the significant inhibition towards methanol oxidation.[11] Moreover, the methanol oxidation is significantly less favourable at the relatively negative potentials for Pd oxide reduction, hence a much smaller back anodic peak (solid line in Figure 6.1b) is observed as compared to that found with the formate oxidation (solid line in Figure 6.1a). The measured back peaks in the two cases are independent of the potential limit (beyond a minimum threshold value). It should be noted that the increased current at high potentials (> 0.3 V vs. SCE) in Figure 6.1b (solid line) corresponds to further methanol oxidation on the background carbon of the nanotube and also the oxidation of the solvent.

Formate oxidation on palladium is reported to result in the formation of carbon dioxide via a direct two-electron transfer pathway,[8, 9] while methanol oxidation is reported to undergo a six-electron transfer process at low overpotentials.[32] For a microdisc electrode, the equation for the expected diffusion limited current is:[33]

$$I_{lim} = 4nFDCr_e$$

where n is the number of electrons transfered, F is the Faraday constant (96485 C mol^{-1}), D is the diffusion coefficient (6.5 × 10^{-11} m^2 s^{-1} for formate[34] and 4 × 10^{-10} m^2 s^{-1} for methanol[35]), C is the concentration of formate or methanol, and r_e is the electrode radius.

Therefore, for 0.5 M formate or methanol, the theoretical diffusion limited current at a Pd microelectrode with radius of 5.4 μm can be estimated as 1.4×10^{-7} A and 2.5×10^{-6} A respectively. However, the experimentally measured oxidative peak currents of 0.5 M formate (2.2×10^{-9} A) and 0.5 M methanol (2.6×10^{-8} A) at a Pd microelectrode (r = 5.4 μm) (red lines in Figure 6.2) are much smaller than the hypothetical diffusion limited values, evidencing that both the formate and methanol oxidation on Pd are surface reaction rate limited processes, rather than transport controlled.

It is worth mentioning that the modified GC electrode showed a slightly higher peak current of formate oxidation (8.3×10^{-5} A) in the solution without the supporting electrolyte $NaClO_4$ (see Figure 6.3), indicating that the extremely high concentration of formate used is able to be self-supporting during the measurement, and suggests that some Pd active sites *may* be blocked by ClO_4^{2-}. Aqueous 5 M formate solution was used in the following experiments.

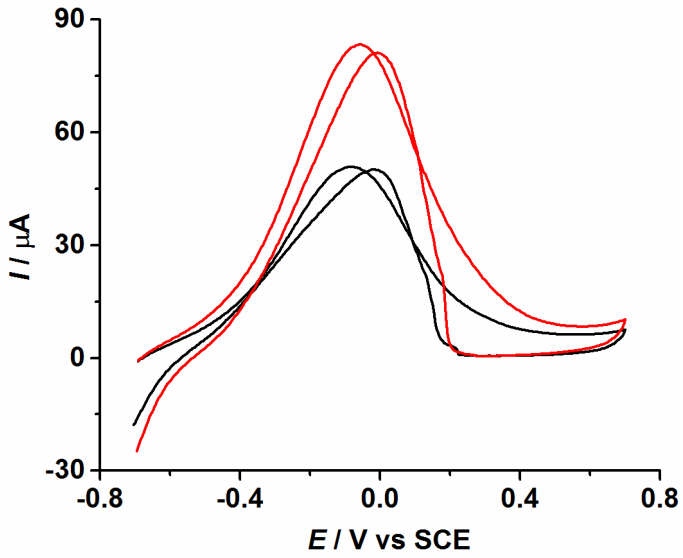

Figure 6.3: Voltammograms of a GC electrode (d = 3.0 mm) modified with 0.96 μg of N-CNT-Pd recording in 5 M formate (aq) in the absence (red line) and presence (black line) of 5 M $NaClO_4$. Scan rate: 50 mV s^{-1}.

6.3.2 CV of a carbon microwire electrode in-situ modified with a dilute coverage of individual N-CNT-Pds

The previous section reported the voltammetric response of a multilayered, porous drop-cast surface. The interpretation of such layer is complex and is hard to analyse.[14-17] In order to study the formate oxidation on adsorbed but spatially well separated individual N-CNT-Pds, a carbon microwire electrode (l = ~1 mm; d = ~7 μm) was first treated with an in-situ modification method by dipping the wire electrode in a suspension of N-CNT-Pd (0.65 pM) containing formate (5 M) for 0.5 h, followed by a CV sweep. During the modification process, about one hundred individual N-CNT-Pds (see section 1 and 3 of the appendix of this chapter) collided with and became immobilized on the microwire electrode, giving an electrode modified with enough N-CNT-Pd to give a clear formate oxidation signal in CV. For the wire electrode used, one monolayer of N-CNT-Pds, assuming the CNTs are perfectly tessellated on the electrode surface, would be 3.4×10^4 CNTs (see section 1 of the appendix of this chapter). Therefore only 0.3% of surface area is covered by one hundred N-CNT-Pds, which gives large spatial separation of N-CNT-Pds on the wire electrode surface. No voltammetric response was detected when CV was recorded immediately after the wire electrode was dipped in the suspension of N-CNT-Pd (dashed lines in Figure 6.4a). After in-situ modification in the formate solution dispersed with N-CNT-Pd for 0.5 h, the wire electrode showed a Faradaic current resulting from formate oxidation in the CV (solid lines in Figure 6.4a). Similar experiments were conducted to study methanol oxidation in 1 M NaOH containing 10 M methanol. It was observed that methanol oxidation signal was also shown in the CV at the wire electrode after one hour of in-situ modification in the suspension of N-CNT-Pd containing methanol (solid lines in Figure 6.4b).

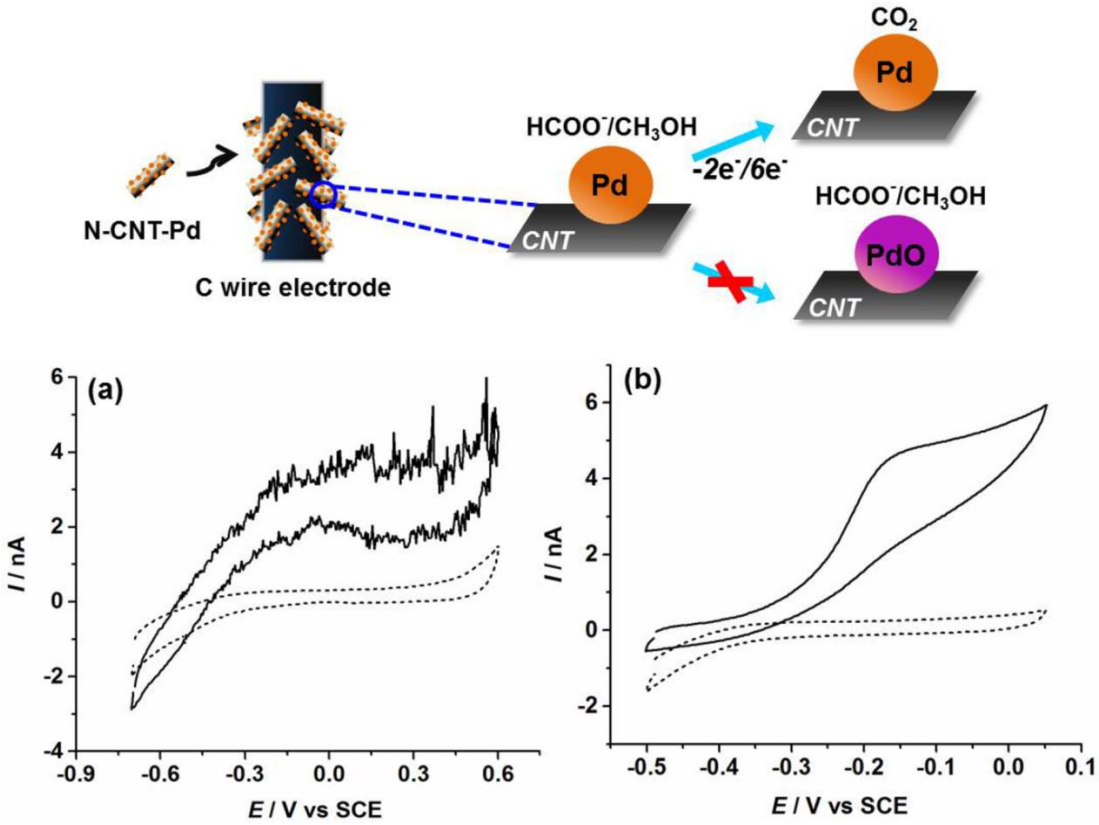

Figure 6.4: (a) CV recorded immediately after a carbon microwire electrode (l = ~1 mm; d = ~7 µm) was inserted in a 0.65 pM suspesion of N-CNT-Pd containing 5 M formate (dashed line) and after the electrode was in-situ modified in the same solution for 30 mins (solid line). Scan rate: 50 mV s^{-1}. (b) CV recorded immediately after a carbon microwire electrode was inserted in a 0.65 pM suspesion of N-CNT-Pd containing 1 M NaOH + 10 M methanol (dashed line) and after the electrode was in-situ modified in the same solution for 60 mins (solid line). Scan rate: 50 mV s^{-1}.

In sharp contrast to the clear oxidation *peaks* shown in the CV of the drop-cast experiments, the wire electrode after in-situ modification with N-CNT-Pd exhibits *steady state* currents at high overpotentials for both formate and methanol oxidation, indicating neither processes are inhibited by Pd oxide formation under these experimental conditions! Note that for the CV of the N-CNT-Pd modified wire electrode, current fluctuations, as shown in Figure 6.4, are variable due to the different state of absorbed carbon nanotubes on the wire electrode surface. Such Faradaic current fluctuations will be explained in detail in chapter 7.[36]

6.3.3 Nano-impacts of N-CNT-Pd

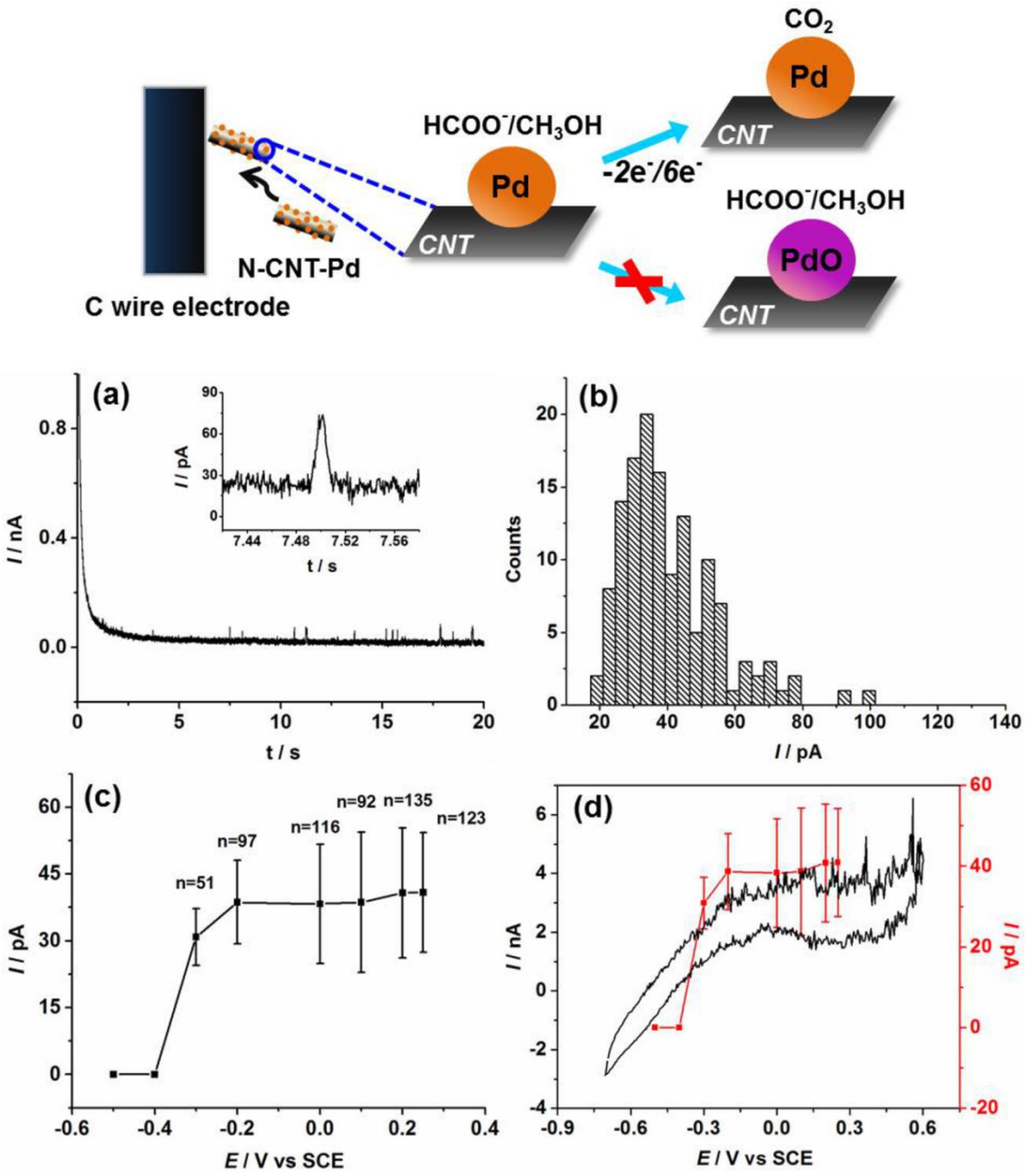

Figure 6.5: (a) Typical chronoamperogram obtained at 0.2 V vs. SCE for a carbon microwire electrode in a 0.65 pM suspesion of N-CNT-Pd containing 5 M formate. (b) The height distribution of 135 current spikes at 0.2 V vs. SCE. (c) Squares: the mean current of individual spikes at different potentials from nano-imapcts of N-CNT-Pd, where n is the number of the spikes. (d) Comparison of cyclic voltammetry of formate oxidation at the wire electrode in-situ modified with well separated N-CNT-Pd (black line) and nano-impacts analysis (red line) of formate oxidation on individual impacting N-CNT-Pd.

Nano-impact experiments of N-CNT-Pd were performed with the aim of separately studying the formate and methanol oxidation on individual impacting single N-CNT-Pd. To achieve this, a clean carbon microwire electrode was first inserted in a suspension of N-CNT-Pd (0.65 pM) containing 5 M formate. Chronoamperograms were then recorded at a series of applied potentials from -0.5 V to +0.25 V vs. SCE. Figure 6.5a shows a typical chronoamperogram at +0.2 V vs. SCE where oxidative spikes are observed, evidencing the impact of the individual carbon nanotubes. No spikes were detected at this potential in the absence of N-CNT-Pd (Figure 6.6a). A total number of 135 current spikes at +0.2 V vs. SCE were recorded, giving an average current of $4.1 \pm 1.5 \times 10^{-11}$ A and their height distribution is shown in Figure 6.5b. The average duration of the spike is short, about 30 ms. This short duration is possibly caused by the formation of CO_2 gas bubbles on the palladium surface[37] or due to adsorbed carbon intermediates, $CO_{(ad)}$, produced by the further reduction of CO_2,[38] leading to the deactivation of Pd active sites. The mean currents of the individual spikes as a function of potential from nano-impacts of N-CNT-Pd are shown in Figure 6.5c, where it is observed that the average current at the potentials more positive than -0.2 V vs. SCE show a plateau at around 40 pA. No spikes were detected at potentials more negative than -0.4 V vs. SCE (Figure 6.6b). The average current from the spikes is found to onset at the potentials at which formate oxidation is observed in the CV (Figure 6.1a), evidencing that the detected current spikes correspond to Faradaic currents associated with formate oxidation catalyzed by the individual impacting N-CNT-Pd.

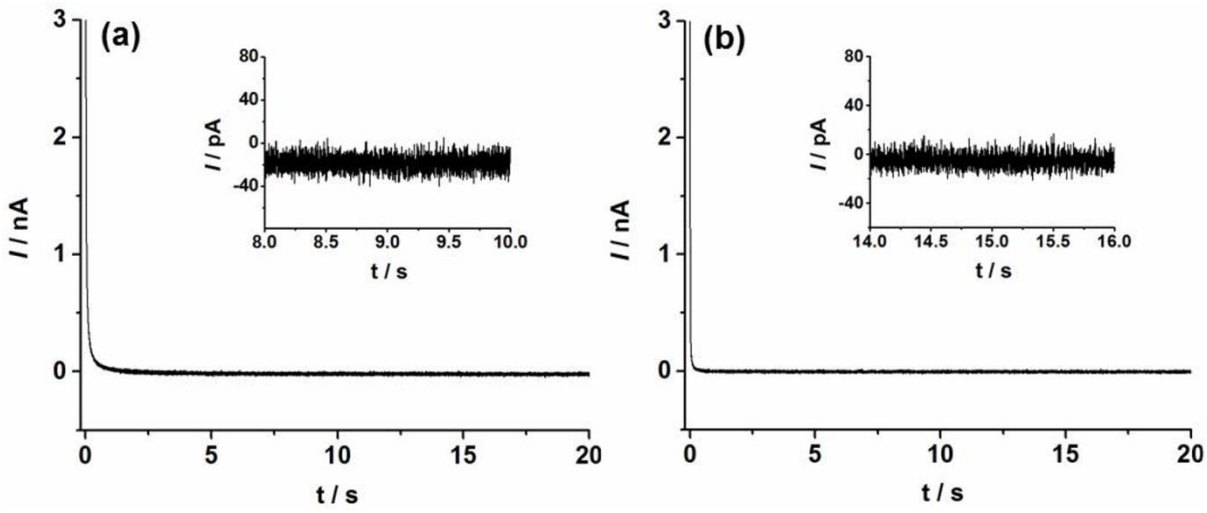

Figure 6.6: Chronoamperogram of a carbon microwire electrode (a) at +0.2 V vs. SCE in 5 M formate in the absence of N-CNT-Pd; (b) at -0.4 V vs. SCE in a 0.65 pM suspesion of N-CNT-Pd containing 5 M formate.

By modelling the N-CNT-Pd as a cylindrical electrode ($r = 6.5 \times 10^{-8}$ m; $l = 5 \times 10^{-8}$ m), for a mass transport control process, the expected peak current on single N-CNT-Pd from the oxidation of formate (5 M) can be estimated as 3.68×10^{-7} A. The average current of the spikes from formate oxidation is about 40 pA, which is significantly smaller than the expected peak current (3.68×10^{-7} A) for a mass transport control process. It further evidences that formate oxidation on individual N-CNT-Pds is a surface reaction rate limited process, rather than being under mass transport control. Moreover, from the dropcasting experiments, the expected current of formate oxidation at a *single* N-CNT-Pd (ca. 5 μm in length, 130 nm in diameter) can be estimated as 7.9 pA by directly dividing the peak current (8.3×10^{-5} A) (red line in Figure 6.3) by the amount of dropcast N-CNT-Pds ($1.0_5 \times 10^{7}$) (see section 2 of the appendix of this chapter). This value of 7.9 pA is much less than the average currents (~40 pA) detected from the nano-impact experiment. Therefore the higher currents likely result from the physical isolation of the carbon nanotubes in the impact experiment; in contrast the dropcast material will inevitably form irregular aggregated multilayers on GC electrode surface.

In the nano-impact experiments, the collision of individual N-CNT-Pd with the wire electrode creates extremely high mass transport conditions for formate oxidation because of the small physical size of the individual carbon nanotubes.[28, 29] Nano-impact analysis shows that the average current from formate oxidation on individual N-CNT-Pd remains stable even at the high overpotentials. The stable oxidation current is in agreement with the steady state current observed in the in-situ modification experiments (Figure 6.5d), further evidencing that under high mass transport conditions Pd oxide formation is significantly inhibited and as a result higher electro-oxidation efficiency for formate was achieved.

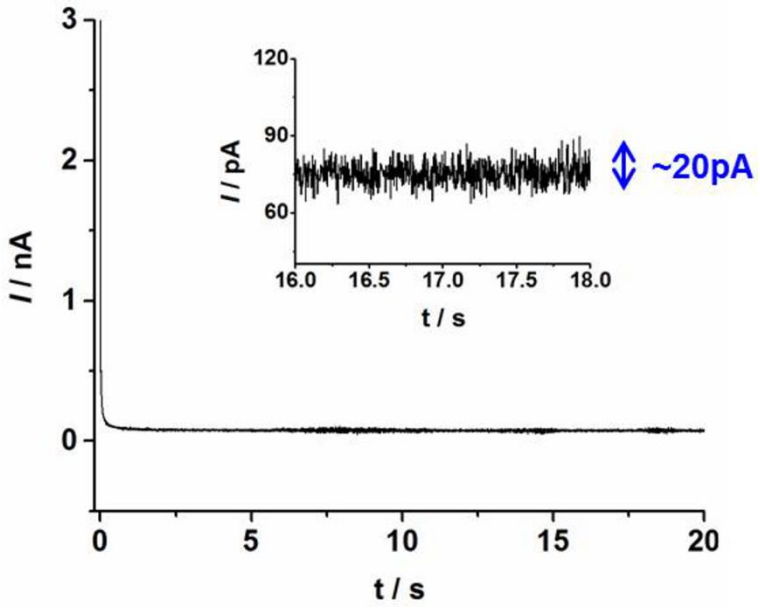

Figure 6.7: Chronoamperogram of a carbon microwire electrode at 0.0 V vs. SCE in a 0.65 pM suspesion of N-CNT-Pd containing 1 M NaOH and 10 M methanol.

The nano-impact experiments were also performed to detect the signals of methanol oxidation on individual N-CNT-Pds, but no spikes were detected (Figure 6.7). Based on the dropcasting experiments, the expected current from methanol oxidation on single N-CNT-Pd is calculated to be 1.2 pA. Although the average current from individual impacting N-CNT-Pds might be several times bigger than 1.2 pA in the nano-impact experiments according to

the results of formate oxidation, it is still too small to be detected due to the comparable background noise (~ 20 pA) (Figure 6.7).

6.3.4 Comparison and inferences

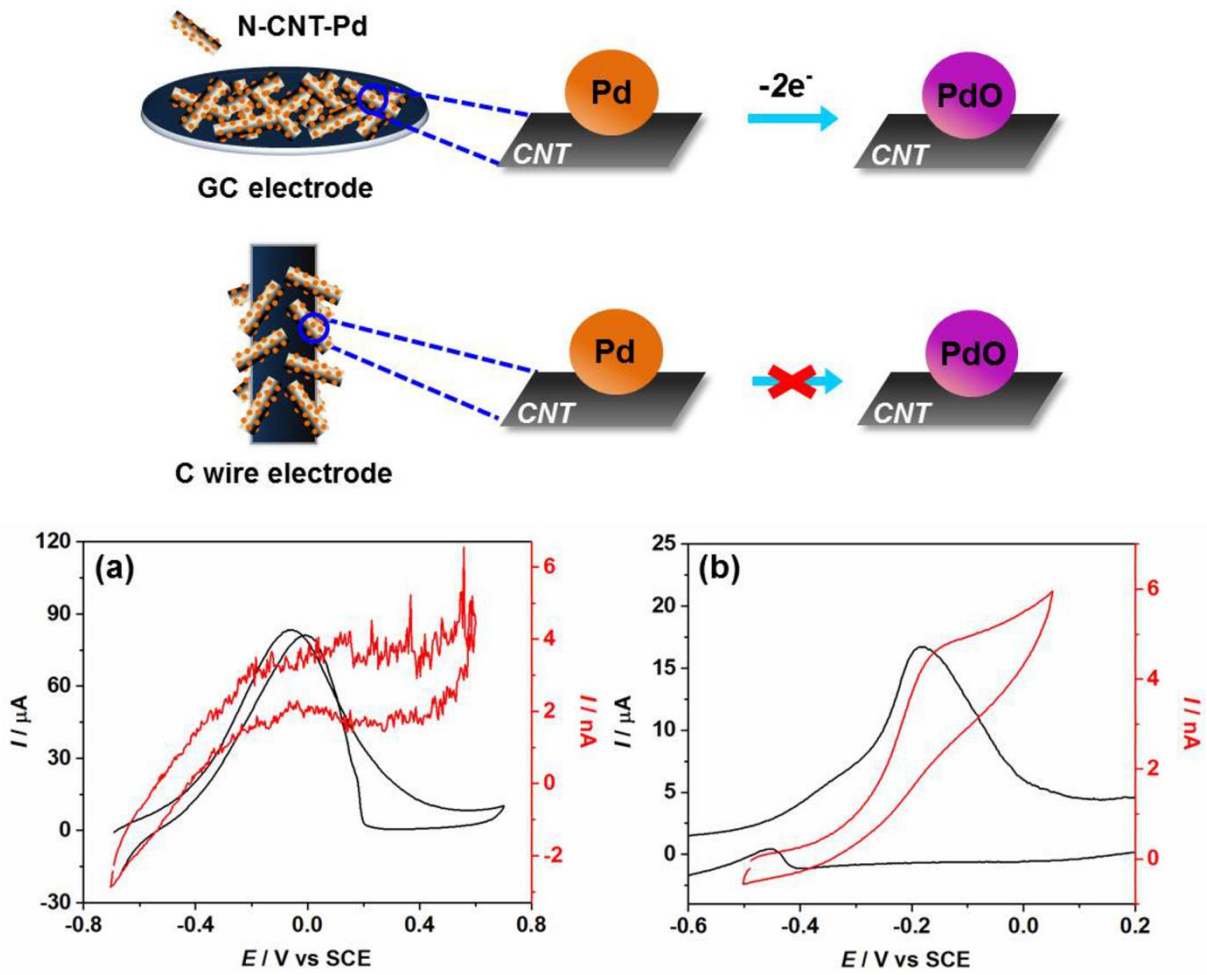

Figure 6.8: Comparison of cyclic voltammograms of formate oxidation (a) and methanol oxidation (b) on N-CNT-Pd drop-cast GC electrode (black lines) and the carbon microwire electrode in-situ modified with well separated N-CNT-Pd (red lines).

We next compare the CV of formate oxidation and methanol oxidation on the GC electrode drop-cast with N-CNT-Pd and their CV at the wire electrode modified with a dilute coverage of well separated N-CNT-Pd. A striking difference is that a *steady state* current is observed in both formate and methanol oxidation at spatially well separated individual N-

CNT-Pd, instead of the current *peaks* as shown in the CV response of the dropcast N-CNT-Pd (Figure 6.8). Consequently it is concluded that for well separated individual N-CNT-Pd, the palladium oxidation (eq. (6.3)) as a competitive reaction is significantly inhibited; hence the majority of Pd active sites on palladium nanoparticles remain active even at highly oxidizing potentials. The Pd active sites therefore continue to contribute to the catalysis of the formate or methanol oxidation at high potentials. Since the specific reaction routes for formate and methanol oxidation on palladium are intensively studied and reported differently[9-10, 39-43], the overall equations are shown here as representatives (eq. (6.1), (6.2)):

$$HCOO^- \rightarrow CO_2 + H^+ + 2e^- \quad (6.1)$$

$$CH_3OH + H_2O \rightarrow CO_2 + 6H^+ + 6e^- \quad (6.2)$$

$$Pd + H_2O \rightarrow PdO + 2H^+ + 2e^- \quad (6.3)$$

It was reported previously that palladium oxide formation was retarded in the presence of the formic acid or methanol.[11, 44] Thus, a likely factor responsible for the observed steady state current is that well separated individual N-CNT-Pd absorbed on the wire electrode surface experience very high mass transport conditions for formate or methanol oxidation. It provides a basis for the preference of formate or methanol oxidation during the competitive processes with palladium oxidation. In contrast an intermingled porous ‘mat’ of carbon nanotubes on the GC electrode is inevitably formed when using the dropcast technique. The resulted relatively limited mass transport conditions for the oxidation of formate or methanol facilitate the formation of the Pd oxide layer; probably the mass transport is a mixture of linear semi-infinite diffusion and thin layer transport. For well-separated individual N-CNT-Pds, there are large numbers of redox species around which creates high mass transport conditions, while overlapping diffusion regime is formed on the ‘mat’ of N-CNT-Pds due to

the confined volume of the available redox species.[18-20, 45, 46] Similar CVs to those seen with the dropcast N-CNT-Pd were observed when the carbon microwire electrode was inserted in a suspension of N-CNT-Pds of an extremely high concentration (9.2 pM) (ten times higher than that used in the in-situ modification method) for about 10 s, creating a higher population of large N-CNT-Pd ensembles which stick to the wire electrode surface, and are then transferred into the solution containing formate or methanol to run a CV. As shown in Figure 6.9, the oxidation current falls off at high overpotentials in the CV of both formate and methanol oxidation, further evidencing that the current inhibition by Pd oxide formation occurs on the large ensembles of the N-CNT-Pd. It is also demonstrated that the voltammetric response of the N-CNT-Pd towards formate or methanol oxidation can be easily tailored by using different methods to modify the electrodes.

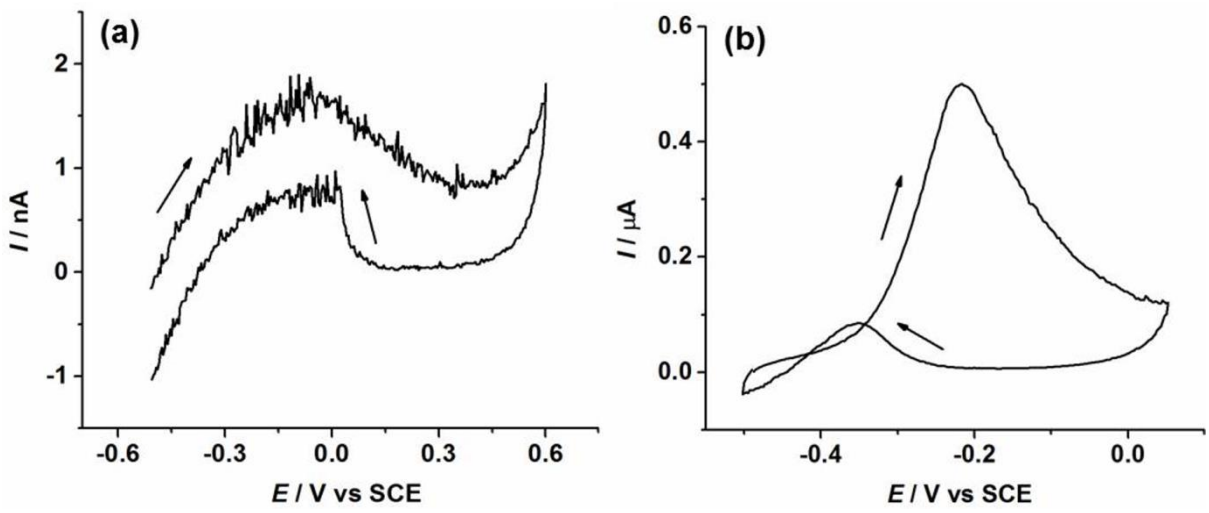

Figure 6.9: Voltammograms of the carbon microwire electrodes modified with higher population of large N-CNT-Pd ensembles in 5 M formate (a) (scan rate: 50 mV/s), 1 M NaOH + 10 M methanol (b) (scan rate: 72 mV s^{-1}).

Overall, Pd oxide formation and formate or methanol oxidation are two competitive processes. The inferior efficiency of formate and methanol oxidation on Pd in their application of fuel cells due in part to the significant inhibition of Pd oxide formation towards these oxidation processes. From the above comparison, it is seen that Pd oxide formation as a

competitive reaction can be retarded under high mass transport conditions for formate and methanol oxidation, which, in this work, was created on the well separated catalyst, N-CNT-Pd. This highlights how the design of the catalyst in fuel cells as well as the local mass transport conditions plays an important role on the energy conversion performance.

6.4 Conclusions

In this chapter, we recorded and compared the voltammograms of formate/methanol oxidation on dropcast N-CNT-Pd and on wire electrodes modified with well-separated individual N-CNT-Pd. It was found that the inhibition from the Pd oxide formation on the oxidative processes on the dropcast N-CNT-Pd became retarded with the use of well separated individual N-CNT-Pd where high mass transport conditions prevail. Further evidence was seen in the study of formate oxidation on a single N-CNT-Pd via the nano-impact method in which the oxidation process was also not hindered by Pd oxidation at high overpotentials. The discovery of the superior electro-catalytic performance under high mass transport conditions suggests requirements for the design of fuel cell development and offers the scope for new catalytic approaches to be developed.

Appendix

1. Estimation of the number of N-CNT-Pd in 1 monolayer on the GC electrode surface and the wire electrode surface

The average size of the N-CNT-Pd used was characterised by SEM analysis in Chapter 4. The size is about 5 μm in length and 130 nm in diameter. Assuming the CNTs are perfectly

tessellated on the GC electrode surface, the total length of nanotube in 1 monolayer can be estimated to be 54 metres through directly dividing the electrode geometrical area (6.98×10^{-6} m^2) by the diameter of N-CNT-Pd (130 nm). Then, the number of N-CNT-Pd can be estimated to be (1.1×10^7) based on the average length of the N-CNT-Pd (5 μm).

Similarly, the geometrical area of the wire electrode (2.20×10^{-8} m^2) is divided by the diameter of the N-CNT-Pd (130 nm) to get the accumulated length of N-CNT-Pd (0.17 metres) in 1 monolayer on the wire electrode surface, which corresponds to 3.4×10^4 CNTs.

2. Estimation of the number of N-CNT-Pd dropcast on the GC electrode

The mass of one pure CNT with 5 μm in length and 130 nm in diameter can be calculated to be 8.9×10^{-14} g from the density of 1.34×10^6 g m^{-3}. With the consideration of Pd decoration, the mass of one N-CNT-Pd is estimated to be 9.1×10^{-14} g according to the decorated percentage of Pd (2.4%, measured by inductively coupled plasma, ICP)[29]. Thus, the number of N-CNT-Pd dropcast on the GC electrode surface ($1.0_5 \times 10^7$ for formate oxidation; 1.3×10^7 for methanol oxidation) is derived by dividing the dropcast amount of N-CNT-Pd (0.96 μg for formate oxidation; 1.2 μg for methanol oxidation) by the mass of one N-CNT-Pd. These dropcast values are very close to the theoretical number (1.1×10^7) for 1 monolayer as estimated in section 1.

3. Estimation of the amount of N-CNT-Pd adsorbed on the wire electrode with in-situ modification method

The amount of N-CNT-Pd adsorbed on the wire electrode with in-situ modification method can be derived from the stead state current (about 4×10^{-9} A) of the formate oxidation at the modified wire electrode (Figure 6.4a) and the average current (about 4×10^{-11} A) of formate oxidation on individual N-CNT-Pd from nano-impacts analysis (Figure 6.5). Therefore, the

number of the N-CNT-Pd adsorbed on the wire electrode for the study of formate oxidation is estimated to be about one hundred.

References

[1] X. Li, C. Batchelor-McAuley, K. Tschulik, L. Shao and R. G. Compton, *ChemPhysChem*, **2015**, *16*, 2322-2325.

[2] S. Wasmus and A. Küver, *J. Electroanal. Chem.*, **1999**, *461*, 14-31.

[3] A. Hamnett, *Catal. Today*, **1997**, *38*, 445-457.

[4] C. Rice, S. Ha, R. I. Masel, P. Waszczuk, A. Wieckowski and T. Barnard, *J. Power Sources*, **2002**, *111*, 83-89.

[5] B. C. H. Steele and A. Heinzel, *Nature*, **2001**, *414*, 345-352.

[6] N. V. Rees and R. G. Compton, *J. Solid State Electrochem.*, **2011**, *15*, 2095-2100.

[7] A. Chen and C. Ostrom, *Chem. Rev.*, **2015**, *115*, 11999-12044.

[8] K. Jiang, H. X. Zhang, S. Zou and W. B. Cai, *Phys. Chem. Chem. Phys.*, **2014**, *16*, 20360-20376.

[9] B. D. Adams, R. M. Asmussen, C. K. Ostrom and A. Chen, *J. Phys. Chem. C*, **2014**, *118*, 29903-29910.

[10] C. Bianchini and P. K. Shen, *Chem. Rev.*, **2009**, *109*, 4183-4206.

[11] T. Takamura and Y. Sato, *Electrochim. Acta*, **1974**, *19*, 63-68.

[12] A. Capon and R. Parsons, *J. Electroanal. Chem. Interfacial Electrochem.*, **1973**, *44*, 239-254.

[13] Y. Pan, R. Zhang and S. L. Blair, *Electrochem. Solid State Lett.*, **2009**, *12*, B23-B26.

[14] K. R. Ward, M. Gara, N. S. Lawrence, R. S. Hartshorne and R. G. Compton, *J. Electroanal. Chem.*, **2013**, *695*, 1-9.

[15] M. C. Henstridge, E. J. F. Dickinson, M. Aslanoglu, C. Batchelor-McAuley and R. G. Compton, *Sens. Actuators, B*, **2010**, *145*, 417-427.

[16] I. Streeter, G. G. Wildgoose, L. Shao and R. G. Compton, *Sens. Actuators, B*, **2008**, *133*, 462-466.

[17] C. Batchelor-McAuley and R. G. Compton, *J. Phys. Chem. C*, **2014**, *118*, 30034-30038.

[18] H. S. Toh, K. Jurkschat and R. G. Compton, *Chem. Eur. J.*, **2015**, *21*, 2998-3004.

[19] S. J. Cloake, H. S. Toh, P. T. Lee, C. Salter, C. Johnston and R. G. Compton, *ChemistryOpen*, **2015**, *4*, 22-26.

[20] H. S. Toh, C. Batchelor-McAuley, K. Tschulik, M. Uhlemann, A. Crossley and R. G. Compton, *Nanoscale*, **2013**, *5*, 4884-4893.

[21] X. Xiao and A. J. Bard, *J. Am. Chem. Soc.*, **2007**, *129*, 9610-9612.

[22] A. J. Bard, H. Zhou and S. J. Kwon, *Isr. J. Chem.*, **2010**, *50*, 267-276.

[23] L. S. Y. Ly, C. Batchelor-McAuley, K. Tschulik, E. Kätelhön and R. G. Compton, *J. Phys. Chem. C*, **2014**, *118*, 17756-17763.

[24] W. Cheng and R. G. Compton, *Angew. Chem. Int. Ed.*, **2015**, *54*, 7082-7085.

[25] M. Pumera, *ACS Nano*, **2014**, *8*, 7555-7558.

[26] N. V. Rees, *Electrochem. Commun.*, **2014**, *43*, 83-86.

[27] W. Cheng and R. G. Compton, *Trends Anal. Chem.*, **2014**, *58*, 79-89.

[28] X. Li, C. Lin, C. Batchelor-McAuley, E. Laborda, L. Shao and R. G. Compton, *J. Phys. Chem. Lett.*, **2016**, *7*, 1554-1558.

[29] X. Li, C. Batchelor-McAuley, S. A. I. Whitby, K. Tschulik, L. Shao and R. G. Compton, *Angew. Chem. Int. Ed.*, **2016**, *55*, 4296-4299.

[30] J. Ellison, C. Batchelor-McAuley, K. Tschulik and R. G. Compton, *Sens. Actuators, B*, **2014**, *200*, 47-52.

[31] J. Ellison, K. Tschulik, E. J. E. Stuart, K. Jurkschat, D. Omanović, M. Uhlemann, A. Crossley and R. G. Compton, *ChemistryOpen*, **2013**, *2*, 69-75.

[32] T. Takamura and F. Mochimaru, *J. Electrochem. Soc.*, **1967**, *114*, 1251-1254.

[33] D. Shoup and A. Szabo, *J. Electroanal. Chem. Interfacial Electrochem.*, **1982**, *140*, 237-245.

[34] Y. Wang, B. Wu, Y. Gao, Y. Tang, T. Lu, W. Xing and C. Liu, *J. Power Sources*, **2009**, *192*, 372-375.

[35] I. Danaee, M. Jafarian, A. Mirzapoor, F. Gobal and M. G. Mahjani, *Electrochim. Acta*, **2010**, *55*, 2093-2100.

[36] H. Hodson, X. Li, C. Batchelor-McAuley, L. Shao and R. G. Compton, *J. Phys. Chem. C*, **2016**, *120*, 6281-6286.

[37] A. Mikołajczuk, A. Borodzinski, P. Kedzierzawski, L. Stobinski, B. Mierzwa and R. Dziura, *Appl. Surf. Sci.*, **2011**, *257*, 8211-8214.

[38] J. Y. Wang, H. X. Zhang, K. Jiang and W. B. Cai, *J. Am. Chem. Soc.*, **2011**, *133*, 14876-14879.

[39] M. Baumer, J. Libuda, K. M. Neyman, N. Rosch, G. Rupprechter and H.-J. Freund, *Physical Chemistry Chemical Physics* **2007**, *9*, 3541-3558.

[40] M. Borasio, O. Rodríguez de la Fuente, G. Rupprechter and H.-J. Freund, *The Journal of Physical Chemistry B* **2005**, *109*, 17791-17794.

[41] F. Miao, B. Tao, L. Sun, T. Liu, J. You, L. Wang and P. K. Chu, *Journal of Power Sources* **2010**, *195*, 146-150.

[42] Y. Zhou, J. Liu, J. Ye, Z. Zou, J. Ye, J. Gu, T. Yu and A. Yang, *Electrochimica Acta* **2010**, *55*, 5024-5027.

[43] C. Lamy, A. Devadas, M. Simoes and C. Coutanceau, *Electrochimica Acta* **2012**, *60*, 112-120.

[44] H. Miyake, T. Okada, G. Samjeske and M. Osawa, *Phys. Chem. Chem. Phys.*, **2008**, *10*, 3662-3669.

[45] M. Gara, E. Laborda, P. Holdway, A. Crossley, C. J. V. Jones and R. G. Compton, *Phys. Chem. Chem. Phys.*, **2013**, *15*, 19487-19495.

[46] A. Schneider, L. Colmenares, Y. E. Seidel, Z. Jusys, B. Wickman, B. Kasemo and R. J. Behm, *Phys. Chem. Chem. Phys.*, **2008**, *10*, 1931-1943.

Chapter 7

Single-Carbon Nanotube-Electrode Contact

In previous chapters, fluctuations in the current-time response of some electrocatalytic reactions including the hydrogen oxidation reaction (HOR) (Chapter 4), the oxygen reduction reaction (Chapter 5), formate oxidation and methanol oxidation (Chapter 6) mediated at single carbon nanotube surfaces with the use of the nano-impacts method is clearly observed. To elucidate the origins of the current fluctuation, in the first part of this chapter, we compare the chronoamperometric and cyclic voltammetric responses of HOR at a single palladium-coated carbon nanotube immobilised on the gold surface to analogous data on a carbon substrate to determine the possible influence of the substrate material on the nanotube-electrode electrical contact. No significant distinction between the gold and carbon was found, indicating in the light of the considerable differences in the substrate materials' intrinsic electronic structures that it is the nano-motion of a nanotube at the electrode surface, which is likely responsible for the observed current modulation. This nano-motion creates a varying contact resistance, to which the noise in the current-time signal of the mediated reaction is attributed. In addition, stochastic ex-situ adsorption of single nanotubes onto the gold electrode followed by careful drying of the electrode surface was found to drastically reduce the current fluctuation, again implying that the physical motion of the nanotube at the electrode is responsible for the modulation of current. This work has been published in *J. Phys. Chem. C.*[1]

Although removal of the solvent via drying the contact has been found to experimentally improve the systems response, an apparently large contact resistance is still observed from

the voltammograms of HOR at single immobilised carbon nanotubes as revealed by the much higher overpotentials than expected. Thus, in the second part of this chapter, a new methodology is developed to enable the measurement of the resistance across individual carbon nanotube-electrode contacts. Carbon nanotubes (CNTs) are suspended in the solution phase and occasionally contact the electrified interface, some of which bridge a micron sized gap between two microbands of an interdigitated gold electrode. A potential difference is applied between the contacts and the magnitude of the current increase after the arrival of the CNT gives a measure of the resistance associated with the single CNT-gold contact. These experiments reveal the presence of a high contact resistance (~50 MΩ) which significantly dominates the charge transfer process. Further measurements on ensembles of CNTs made using a dilute layer of CNTs affixed to the interdigitated electrode surface and measured in the absence of solvent showed responses consistent with the same high value of contact resistance. This work has been published in *J. Phys. Chem. Lett*.[2]

7.1 Single Carbon Nanotube Voltammetry: Investigating the Origin of the Current Fluctuations

7.1.1 Introduction

Success in detecting nanoparticle-mediated redox activity is in part predicated upon the redox reaction of interest being significantly slower on the 'inert' electrode substrate than on the nanoparticle surface of study. This large discrepancy in rates may be achieved either by the use of a suitable ‘inner-sphere’ electron transfer reaction, or by the insulation of the supporting electrode with a ‘thin’ partially passivating layer.[3, 4] The use of carbon as a supporting electrode material is often beneficial due to the commonly associated sluggish heterogeneous electron transfer kinetics.[5] Alternative metallic materials which often exhibit

slow electron transfer kinetics, such as mercury[6-8], are complicated by the ready formation of chloride salts[9] which can and do lead to erroneous results.

One prime aim of such mediated reaction studies is the ability to rapidly screen and study the structure-activity relationship of individual nanoparticles. In the catalytic nano-impacts experiments (see Chapter 2 section 2.2), assuming the nanoparticle is sufficiently conductive, the electrochemical reaction kinetics will likely be determined by the interfacial electron transfer: the rate of reaction may either be limited by the transfer of electrons between the nanoparticle and the supporting inert electrode, or at the nanoparticle/solution interface. Furthermore, as the nanoparticle approaches the potentiostated electrode from the solution phase the rate determining step will likely vary as a function of the nanoparticle/electrode separation. At large separations the electron transfer from the nanoparticle to the electrode will be determined by the tunnelling probability;[10] consequently, under this regime the rate of electron transfer will likely exhibit an exponential variation as a function of the inter nanoparticle/electrode distance.[10, 11] For contacts with a diameter smaller than the mean free path of an electron, the interfacial resistance will scale as the inverse square of the contact radius (the so-called Sharvin limit corresponding to ballistic transfer across the interface);[11] conversely for contacts larger than the electron mean free path, the transfer can be considered diffusive and the interfacial resistance will be proportional to the inverse contact radius (Holm/Maxwell limit).[12] Subsequently, at shorter distances and with the formation of an electrical contact, the interfacial rate of transfer may be sufficiently large for the rate determining step to switch to that of the nanoparticle/solution interface. However, the resistance of such a nanoparticle/electrode contact will depend upon a variety of factors, not least the size of the contact area. For smaller, highly symmetric nanoparticles (spherical for example), it is reasonable that the nanoparticles' electrical contact with the electrode will be

dominated by a single point. However, for larger and less symmetric particles the total current will constitute the summation of multiple parallel contributions.[12]

Such investigations into the activity of individual nanoparticles are also reliant on prolonged contact of the impacting nanoparticle with the electrode surface to allow the extraction of kinetic data; for instance a complete (forward then backward) scan at 50 mVs^{-1} over a potential range of 2 V requires a residence time of at least 80 s. The HOR at an individual nitrogen-doped, palladium nanoparticle-modified carbon nanotube (N-CNT-Pd) impacting with a carbon fibre wire electrode has been monitored voltammetrically (Chapter 4). The residence times of the N-CNT-Pds at the electrode surface are considerable (cf. >10s seconds), implying a relatively strong physical contact with the electrode. However, during the course of the impact the Faradaic current fluctuates significantly; these fluctuations were observed as 'noise' in current-time measurements. Consequently, the first part of this chapter aims to identify the physical origins of these fluctuations in the recorded current. This is undertaken by comparing the voltammetric responses of individual N-CNT-Pds towards the HOR at both carbon and gold substrates. The electronic structures of these two materials differ significantly. The carbon fibre used within this work is predominantly graphitic in nature; consequently the material is a semi-metal and the density of states of the two materials at their respective fermi levels differs by two orders of magnitude(0.28 states $atom^{-1}$ eV^{-1} for Au vs. 2.2×10^{-3} states eV^{-1} $atom^{-1}$ for HOPG).[5] The difference in electronic structure is clearly reflected, as well as in the case of the anisotropic resistivity of graphitic carbon.[13-15] Given that the fluctuations in current likely arise from its modulation at the nanoparticle/electrode interface, by altering the electronic structure of the electrode the physical origin of this modulation can be probed.

7.1.2 Experimental section

7.1.2.1 Chemicals

Preparation and characterization of the nitrogen-doped carbon nanotubes decorated with palladium nanoparticles (N-CNT-Pd) is shown in Chapter 4. KNO_3 was obtained from Sigma-Aldrich and was used as received without further purification. All solutions were made up with deionised water of resistivity not less than 18.2 MΩ cm (25^{o}C, Millipore) and outgassed with N_2 before taking measurements at 298 K. Hydrogen (≥ 99.98% H_2) and nitrogen were supplied by BOC, Surrey, UK.

7.1.2.2 Cyclic voltammetry of HOR at macroelectrodes

The Pt, Au and glassy carbon (GC) macroelectrodes used in the initial HOR experiment were of diameter 1.6 mm, 3.0 mm and 3.0 mm respectively. The Au microelectrode used for nanoimpact experiments was 48 μm in diameter. Working electrodes were polished with 1, 0.3 then 0.05 μm alumina slurries, rinsed with deionised water and dried with N_2 before use. Cyclic voltammetry of HOR at the Pt mactoelectrode was measured against a mercurous sulphate reference electrode (MSE) (+0.64 V vs. SHE) while that on the GC and Au macroelectrodes was recorded vs. Ag/AgCl (+0.235 V vs. SHE). In both cases, a Pt sheet works as the counter electrode. Experiments were carried out at T = 298 K in a thermostatted Faraday cage using an Autolab potentiostat (Metrohm-Autolab BV, Netherlands). A 0.2 M KNO_3 electrolyte was degassed with N_2 and then saturated with H_2 (~0.78 mM) by bubbling for 5 min before voltammograms were recorded.

7.1.2.3 Nanoimpact experiments on an Au microelectrode

Nanoimpact experiments on the Au microelectrode were performed with a two-electrode setup, an Ag wire serving as both a counter and pseudo-reference electrode. A suspension of

N-CNT-Pd was prepared by sonicating 2.4 mg N-CNT-Pd in 5 mL 0.2 M KNO_3 solution in a Fisher Scientific FB15050 ultrasonic bath until the nanoparticles were well-dispersed. 20 µL of this suspension (containing 9.6 µg N-CNT-Pd) was then added to 180 µL 0.2 M KNO_3 electrolyte which had previously been N_2-degassed and H_2-saturated. The solution was then bubbled briefly for a few seconds to disperse the nanoparticles. Higher nanoparticle concentrations were subsequently obtained by addition of further aliquots of the 2.4 mg N-CNT-Pd suspension. To detect nanoimpacts, the potential was held at +0.6 V vs. Ag wire for consecutive periods of 30 seconds. The voltammetry of the HOR was recorded at 50 mV s^{-1}.

7.1.2.4 Ex-situ adsorption of a single N-CNT-Pd on an Au microelectrode

An Au microelectrode was immersed in a suspension of 2.4 mg N-CNT-Pd in 5 mL 0.2 M KNO_3 for a few seconds followed by its subsequent removal. The electrode surface was then left to dry in air. During the immersion time the stochastic collision of a single nanoparticle with the electrode surface resulted in its adsorption with the evaporation of the remaining solvent partially strengthening the nanotube-electrode contact. The voltammetry of the N-CNT-Pd modified Au microelectrode was then recorded in the same H_2-saturated electrolyte as used in the previous nanoimpact experiments. An MSE reference electrode supplied by ALS, Japan and a Pt counter electrode were used.

7.1.3 Results and discussion

7.1.3.1 Cyclic voltammetry of HOR at macroelectrodes

The oxidation of a hydrogen saturated aqueous solution (0.77 mM) containing 0.2 M KNO_3 was studied voltammetrically at platinum, gold and GC macroelectrodes (Figure 7.1). On the

platinum electrode a clear quasi-reversible wave was observed at -0.4 V vs. Ag/AgCl corresponding to the two-electron oxidation of hydrogen, as given by;

$$H_2 - 2e^- \rightarrow 2H^+$$

The diffusional tail of the voltammogram is distorted at higher potentials (between -0.3 and -0.1 V vs. Ag/AgCl) due to the desorption/adsorption of the hydrogen from the platinum surface.[16] Note that the position of the HOR wave on Pt is not at 0.0 V vs. SHE. This arises predominantly from the non-unity stoichiometry of the redox reaction and the fact that under standard conditions (1 bar pressure hydrogen) the solution phase concentration of protons and hydrogen differ by almost three orders of magnitude.[17]

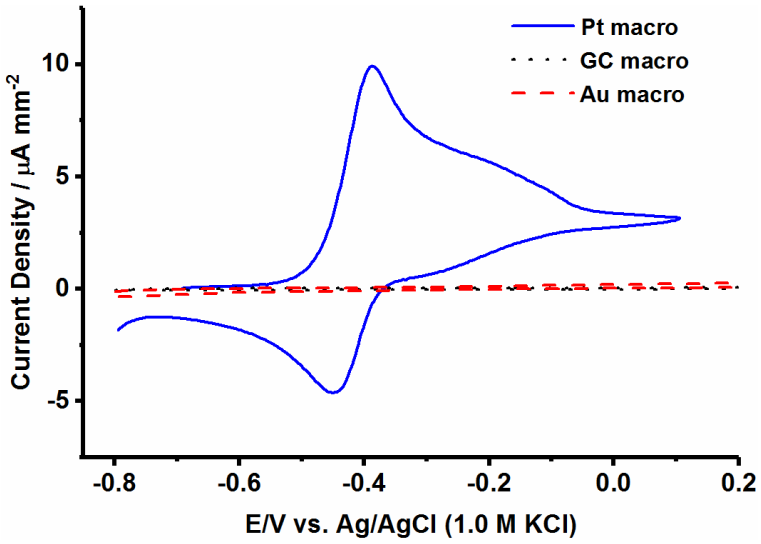

Figure 7.1: Cyclic voltammetric response of the HOR ($[H_2]_{sat.}$ = 0.77 mM) on a Pt (blue solid line), Au (red dashed line) and GC (black dotted line) macroelectrodes; notably the HOR peak ~-0.4 V (vs. Ag/AgCl) is absent on Au and GC. The response on Pt was recorded against an MSE (+0.64 V vs. SHE) reference electrode so has been shifted by +0.405 V for comparison with the GC and Au scans taken vs. Ag/AgCl (+0.235 V vs. SHE).

In contrast to the voltammetric response recorded at the platinum electrode, the GC and gold electrodes exhibited no appreciable activity towards the HOR prior to the oxidation of

the solvent medium which occurs from about +0.4 V vs. Ag/AgCl on both substrates. This is despite their ability to catalyse the proton reduction at a moderate overpotential.[1] However this disparity from the response on Pt enables their application to nanoimpact experiments as 'inert' substrate electrodes upon which the reaction mediated at the catalytically active nanoparticle may be probed.

7.1.3.2 Nanoimpact experiments on an Au microelectrode

In chapter 4, a carbon fibre wire electrode (length = 1mm; diameter = 7μm) was immersed in a suspension of N-CNT-Pd which was saturated with H_2. The current steps in the recorded chromoaperomograms is observed due to the arrival of an N-CNT-Pd at the electrode surface where upon impact it is able to catalyse the HOR, hence leading to an increase in the recorded current. The carbon fibre wire electrode is selected as a substrate electrode because it is microscopic in only one dimension, which significantly increases the probability of an impact occurring by virtue of the attainment of a quasi-steady state diffusion regime.[18] This offsets the slow mass transport of the N-CNT-Pd resulting from its low diffusion coefficient of 2×10^{-13} m^2 s^{-1}.[19] Since the fabrication of an analogous gold microwire electrode is infeasible due to its differing mechanical properties, a gold microdisc electrode of diameter 48 μm was instead employed. The distinctly smaller size of the gold microelectrode used as compared to the carbon fibre wire electrode requires a distinctly higher concentration of solution phase nanotubes to observe a reasonable impact frequency. During the course of an electrocatalytic impact the currents passed are in the nano-ampere range, consequently the use of a two-electrode system is possible in the absence of significant ohmic distortion. The silver wire was therefore used as both a combined pseudo-reference and counter electrode.

An oxidising potential (0.6 V vs. Ag wire) was applied to the gold working electrode and the resulting current recorded. In the presence of N-CNT-Pd clear current steps were

observed (Figure 7.2a, blue line, shows a representative current step). The magnitudes of the recorded steps are, although variable, highly comparable to those recorded for the same nanotube impacts on the carbon fibre wire electrode. Consequently, these current steps are again concluded to relate to the arrival of a single nanotube to the electrode surface, where upon contact the palladium present catalyses the HOR.

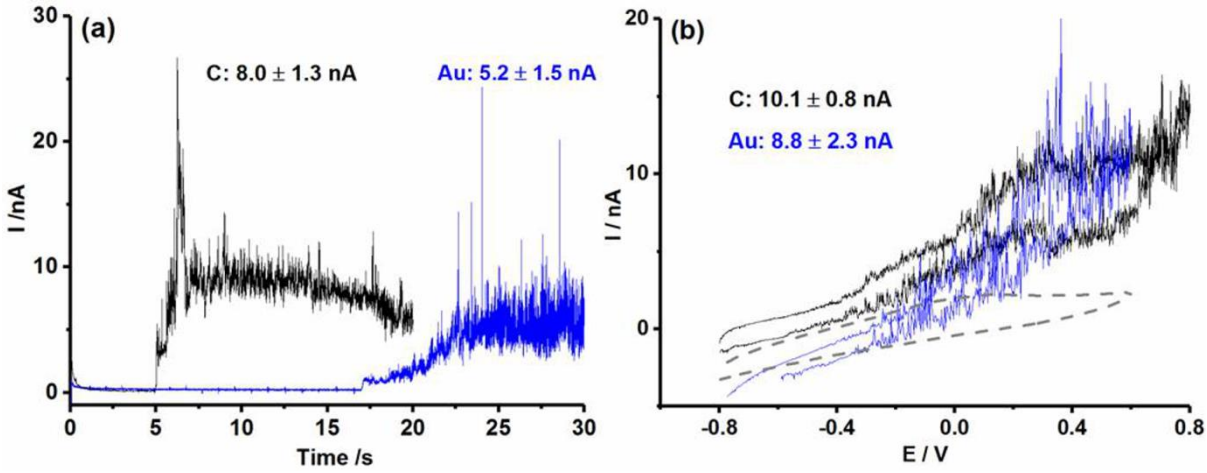

Figure 7.2: (a) 'Steps on' in the chronoamperometric profiles corresponding to impacts of single N-CNT-Pd with the Au microelectrode at + 0.6 V vs. Ag wire (blue) and carbon fibre electrode at + 0.1 V vs. Ag/AgCl (black). The step height above the baseline ± std. deviation is labelled; (b) CVs recorded during impacts of single N-CNT-Pd with the Au microelectrode vs. Ag wire (blue) and carbon fibre electrode vs. Ag/AgCl (black). A blank in H_2-saturated 0.2M KNO_3 without N-CNT-Pd is overlaid (grey dashed). The magnitude of Iss or Iqss above the blank ± std. deviation is labelled. All the measurements were conducted in H_2 saturated 0.2M KNO_3 N-CNT-Pd suspension. CVs were recorded at ν = 50 mV s^{-1}.

Next, upon observing an impact of a carbon nanotube at the electrode surface, a cyclic voltammogram of the oxidation of hydrogen at the individual carbon nanotubes was recorded. Figure 7.2b (blue line) depicts a typical example of the cyclic voltammetric response of individual carbon nanotubes catalysing the oxidation of the solution phase hydrogen on a gold supporting substrate. Also depicted in Figure 7.2b (dashed line) is the response of the gold microelectrode in the absence of N-CNT-Pd. No peak corresponding to the oxidation of

hydrogen was observed on the bare gold surface; this is consistent with that found on the gold macroelectrode (Figure 7.1).

Comparison of the chronoamperometric and voltammetric responses recorded for the single carbon nanotubes impacting at both the carbon and gold electrodes demonstrates that the electrochemical responses are indistinguishable on the two substrates. This is apparent from Figures 7.2 which shows fluctuations in the steady-state HOR current, for comparative step heights or steady-state current magnitudes respectively, as standard deviations. Given the extreme differences between the electronic structures of the two electrode materials (described above), this insensitivity to the electrode substrate is of distinct importance. Moreover, the relatively long residence times of the carbon nanotubes at the electrode surfaces (cf. tens of seconds) indicate a strong association of the carbon nanotubes to the electrode surface. This result highlights the differences between physical and electrical contact, in that although the nanoparticle is resident at the electrode, the properties of the electrical connection are clearly variable with time. The carbon nanotubes are highly conductive due to their multi-walled structure,[20] and their large sizes preclude current fluctuations relating to a shot noise process arising from the finite nature of the solution phase hydrogen concentration.[21] Given this, it is reasonable to conclude that these fluctuations are associated with the electrical connection between the electrode and nanoparticle. Of the cases featuring similar nanoparticle residence times, similar fluctuations have been observed; for example in the electrochemical response of individual spherical gold nanoparticles catalysing proton reduction on impact with a carbon fibre electrode.[22] Consequently, the physical origin of the observed fluctuations is likely common to all the aforementioned systems and is not related to the specific case of impacting carbon nanotubes. Hence, it is credible that the pre-dominant source of the observed current fluctuations relates to the nanoscopic motion of the nanoparticle at the electrode surface which serves to modulate the

electrical connection. In order to evidence this, we further turns to considering the response single carbon nanotubes which were adsorbed at the gold interface and the contact dried prior to electrochemical experimentation.

7.1.3.3 Ex-situ adsorption of a single N-CNT-Pd on an Au microelectrode

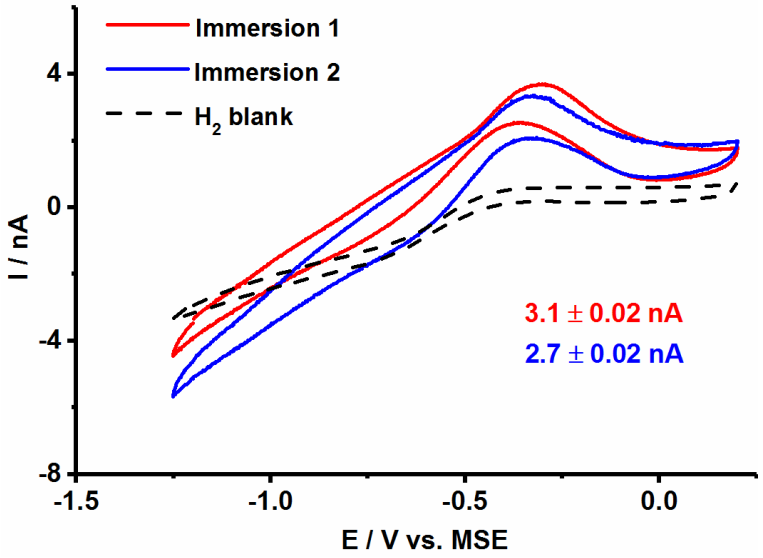

Figure 7.3: Cyclic voltammetric responses of the HOR from separate immersion experiments on the modified Au microelectrode (red, blue), where a single CNT-Pd is adsorbed ex-situ onto the electrode surface before drying, as compared to the unmodified Au microelectrode (black dashed). CVs are recorded in H_2-saturated 0.2 M KNO_3. The maximum current at higher potentials is labelled ± std. deviation.

The same gold microelectrode was immersed in the previously-described 2.4 mg N-CNT-Pd / 5 mL 0.2 M KNO_3 suspension for a few seconds, removed and allowed to dry in air. This enabled the stochastic ex-situ adsorption of a nanotube as described above. The modified electrode was then, after drying, inserted into the previously H_2-saturated electrolyte. Figure 7.3 depicts the representative voltammetric responses of the HOR on the Au microelectrode after modification with N-CNT-Pd. In a majority of cases the current amplitude was comparable to that expected for a single nanotube (2.75 nA for a single nanotube given an

average length of 5 μm) (see Chapter 4, Section 4.3.4). The voltammograms are distinctly different from the majority of observed responses of the in-situ impacted electrodes: notably, the magnitude of the voltammetric wave is not significantly different suggesting that in both examples, a single carbon nanotube is located on and in electrical contact with the gold electrodes. However, of most importance is that the large current fluctuations are no longer observable, and that HOR is inhibited at higher potentials, although this inhibition is reversible as evidenced by the increase in the current on the reverse scan. This 'switching-off' of the HOR at higher over potentials is likely associated with the electrochemical oxidation of the carbon nanotube-supported palladium nanoparticles. The removal of current fluctuations via drying of the electrode evidences that the noise is not inherent to the electrode material or the nanoparticle, but arises from the electrical contact between the nanoparticle and electrode, whereby drying of the electrode improves the contact properties. The extraction of physically meaningful data regarding the kinetics of an electron transfer process has the pre-requisite that large fluctuations in the current are not observed during the course of the Faradaic process. Such good electrical contacts may be formed via the drying of the electrode (as demonstrated) or may adventitiously occur over the course of an in-situ nanoparticle impact.

7.2 Quantifying Single Carbon Nanotube-Electrode Contact via the Nanoimpact Method

7.2.1 Introduction

The development of energy transformation technologies is, in part, built on the production of new and advanced catalytic materials.[23-25] These materials often seek to lower the overpotential associated with a redox reaction, prime examples being the reduction of oxygen or the oxidation of organic fuel stocks.[26-29] Carbon nanotubes feature extensively in this

work both as catalyst supports and as catalysts in themselves, either chemically modified or not.[28, 30] In the early stages of development the synthesized material of interest (i.e. CNTs) is often added as a layer on to a supporting electrode, the resulting electrochemical response of the modified electrode is recorded and used to evidence the 'activity' of the catalyst. Section 1 of the appendix of this chapter provides an illustrative overview of some of the numerous reports in the literature based on the use of CNTs as electrode materials and as the bridge between two electrodes. Importantly, it is commonly implicitly assumed that an ohmic contact with a relatively small resistance between the supporting electrode and the material of study is made. This issue of electrical connectivity becomes yet more complex when multilayer formations of the catalyst are considered.

The first part of this chapter has demonstrated how the connectivity of the material to the electrode surface influences the electrochemical response.[1, 31] Specifically the behavior of individual CNTs has been shown to be highly sensitive to the nature and quality of the contact with the electrode. Although removal of the solvent via drying the contact has been found to experimentally improve the systems response, an apparently large contact resistance is still observed (see section 2 of the appendix of this chapter). However, direct information regarding the connectivity of a carbon nanotube to an electrode surface is not readily obtainable using conventional electrochemical techniques. The second part of this chapter seeks to answer the question of the magnitude of the resistance between a single CNT and electrode, and then extends the study to consider ensembles of CNTs which are shown to have a similar high contact resistance to the single tube measurements. To enable single tube measurements, the nano-impact method is applied based on using multi-walled carbon nanotubes (MWCNTs) to bridge a micron sized gap between two electrodes. The work in previous chapters (and the first part of this chapter) using the nano-impact method relates to the measurement of electrical currents arising from an electrochemical reaction at the

nanoparticle/solution interface. Conversely, in the work presented in the second part, by contacting two electrodes with different potentials a current is induced to occur *across* the CNT. The magnitude of the current increase after the bridging of the CNT allows the associated resistance to be readily measured, revealing the presence of a high contact resistance of the single CNT-gold contact. The MWCNTs are semi-metallic and their inner conductivity sufficient that no significant potential drop occurs along the length of the nanotube. Conventional methods of measuring contact resistances as previously reported require complicated device fabrication and can only measure a single or a few CNTs in an experiment.[32, 33] In contrast, the present methodology enables a simple, statistical and non-destructive measurement of the contact resistance between the CNT and electrode, and is a novel application of the nano-impacts technique.

7.2.2 Experimental section

7.2.2.1 Chemicals

PR24-LHT carbon nanotubes (CNTs) and ethanol (≥ 99.8 %) were purchased from Pyrograf Products Inc. (Ohio, USA) and Sigma-Aldrich respectively.

7.2.2.2 Characterization of CNTs

Transmission electron microscopy (TEM) and dark-field optical microscopy were used to characterize the CNTs. TEM Imaging of CNTs (Figure 7.5a) was conducted with a transmission electron microscope JEOL JEM-3000F equipped with an EDX spectrometer with an accelerating voltage of 300 kV. Sample preparation involved dropcasting suspensions of CNTs in ethanol on holey carbon grids (Agar Scientific) and allowing the surface to dry. Optical measurements were performed on a Zeiss Axio Examiner microscope using a 20x oil-

immersion objective (NA = 0.5, EC Plan-Neofluar). A Hamamatsu ORCA-Flash 4.0 Digital CMOS camera (Hamamatsu, Japan) was applied to provide 16-bit images with 4 megapixel resolution. Camera exposure control was carried out with the software Zen 2 (blue edition, Carl Zeiss Ltd., Cambridge UK). 20 µL CNTs suspension in ethanol (1.2×10^{-13} M) was dropped on a clean slide and dried in air before the optical measurements. ImageJ (The National Institute of Health, USA) was employed to analyze the TEM and optical microscopy images.

7.2.2.3 Gold thin-film interdigitated band array electrode (IDE-Au)

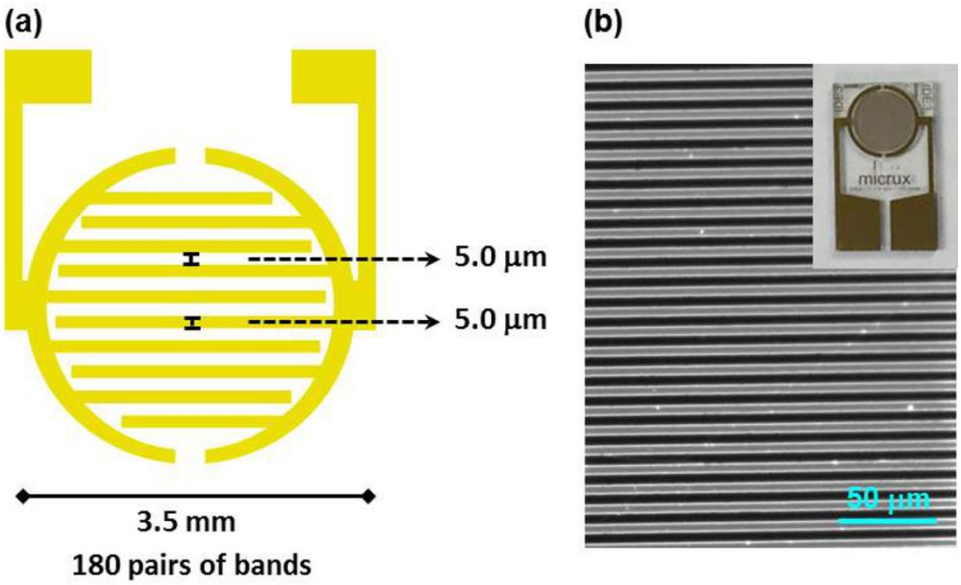

Figure 7.4: (a) Illustration of the interdigitated gold electrode (IDE-Au); (b) An optical microscope image of IDE-Au. Inset: a picture of the whole electrode.

A gold thin-film interdigitated band array electrode (IDE-Au) (ED-IDA3-Au, Micrux Technologies, Spain) is used in this work. The array consists of 180 pairs of bands which are 5.0 mm in width and separated by 5.0 mm gaps. An illustration of the electrode, an optical microscope image and a picture of the whole electrode are shown in Figure 7.4. More details

about the electrodes (ED-IDA3-Au, Micrux Technologies, Spain) can be found at http://www.micruxfluidic.com/archivos/MicruX_thin-film_IDE_electrodes.pdf.

7.2.2.3 Chronoamperometry of the IDE-Au dropcast with CNTs

0.7 ng of CNTs were drop-cast on a gold thin-film interdigitated band array electrode (IDE-Au) (ED-IDA3-Au, Micrux Technologies, Spain) and dried under a N_2 atmosphere. Chronoamperometry was recorded at the modified IDE-Au where a potential difference was applied between the two arrays. The two band arrays of the IDE-Au act as two separate electrodes. The measurements were conducted in a Faraday cage with an Autolab potentiostat (Metrohm-Autolab BV, The Netherlands) at 298 K.

7.2.2.4 Nano-impact experiments of CNTs on the IDE-Au

A suspension of CNTs in ethanol (1.2×10^{-13} M) were sonicated in a Fisherbrand ultrasonic bath S60 (230V 50/60Hz 150W) for 10 min to get a well dispersed suspension. The nano-impact experiments were conducted by inserting the IDE-Au into the suspension of CNTs then recording the chronoamperometry at the IDE-Au in the Faraday cage at 298 K.

7.2.3 Results and discussion

7.2.3.1 Characterization of CNTs

The CNTs used in this work were characterized with Transmission Electron Microscopy (TEM) and dark-field optical microscopy. In order to form a suspension of the carbon nanotubes in solution, sonication of the sample was conducted in a Fisherbrand ultrasonic bath S60 (230V 50/60Hz 150W). The influence of sonication upon the tube length is assessed using dark-field optical microscopy. As shown in Figure 7.5a, tube shaped nanostructures are observed in the TEM image and the diameter distribution of the tubes is displayed in the inset

of Figure 7.5a. The analysis of typical TEM images gives the mean diameter of the CNTs to be 100 ± 29 nm (96 samples). The inset of Figure 7.5b shows a representative optical microscopy image of CNTs after sonication for 10 min. Well dispersed individual CNTs were observed. The analysis of the images gives the length distribution of the CNTs (Figure 7.5b) and the mean length to be 7.1 ± 6.7 μm (412 samples).

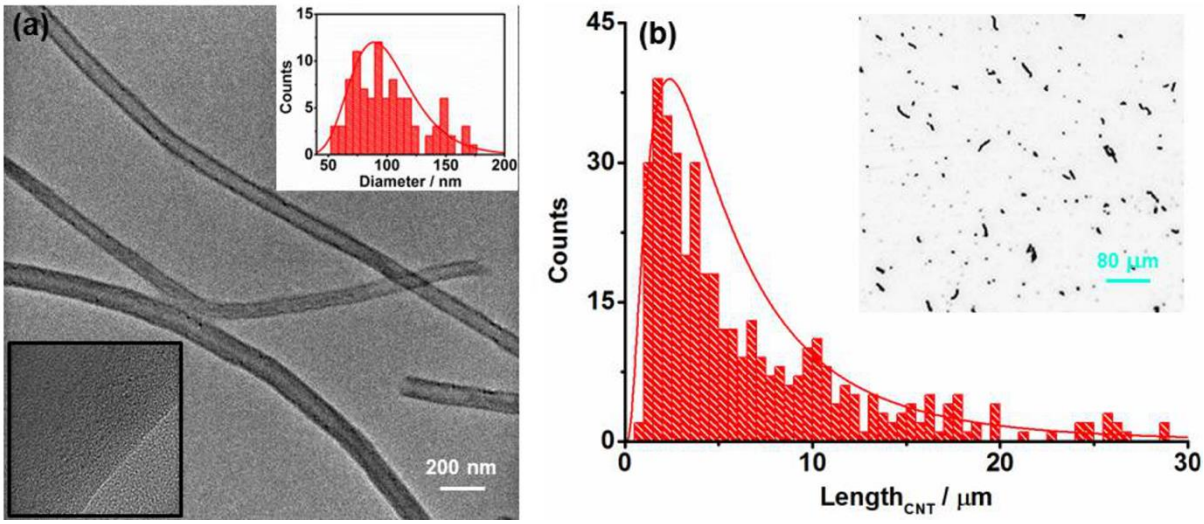

Figure 7.5: (a) Typical TEM image of the CNT. Upper inset is the diameter distribution of the CNT. Lower inset shows the amorphous outer edge and structured inner part of the CNT. (b) Length distribution of CNTs shown in dark-field optical microscopy images. The inset is a typical image of CNTs. The contrast of the image has been inverted for clarity.

Comparison of the optical microscopy images of CNTs with sonication for 0, 10, 120 min was performed and shown in Figure 7.6, and the size measurements give an average length of CNTs to be 13.3 ± 10.3 μm (292 samples), 7.1 ± 6.7 μm (412 samples), 3.2 ± 2.3 μm (312 samples) respectively. In Figure 7.6, the CNTs without sonication treatments (Figure 7.6a) are observed to be relatively long but significantly aggregated, while with long time (120 min) of sonication (Figure 7.6c) the majority of CNTs were broken to be too short (3.2 ± 2.3 μm) to bridge the gap (5 μm) of the IDE-Au. Hence, the CNTs with 10 min of sonication were used in the following experiments.

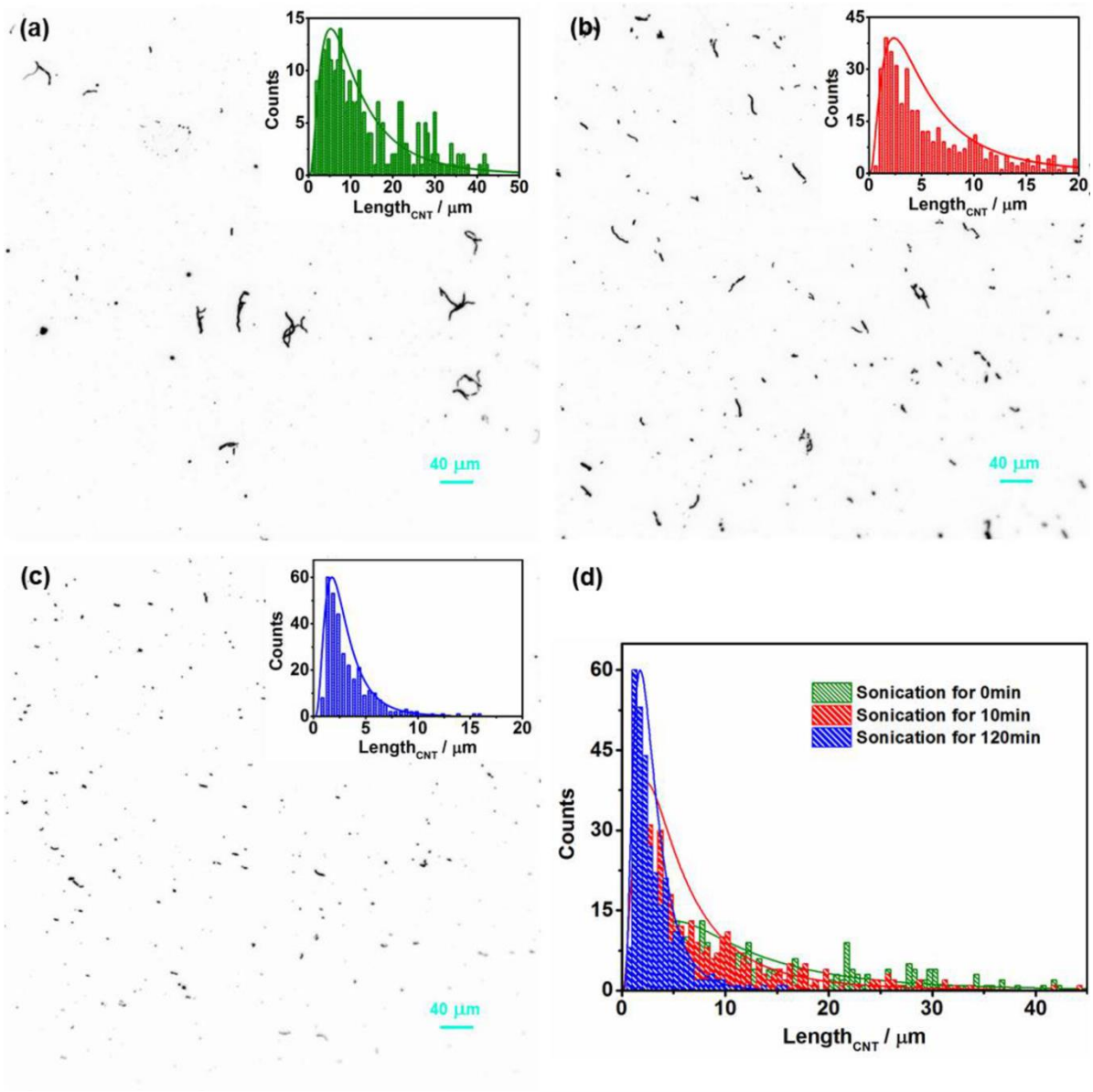

Figure 7.6: Dark-field microscope images of CNTs with vibration for 3min (a), sonication for 10min (b), sonication for 120min (c) and comparison of the length distribution of the CNTs (d).

7.2.3.2 Chronoamperometry of the IDE-Au dropcast with CNTs

As a first approximate route to determining the resistance between the electrode and carbon nanotube a suspension of carbon nanotubes (0.70 ng) in ethanol was dropcast on to a gold interdigitated band electrode array (IDE-Au). Upon evaporation of the solvent (drying under an N_2 atmosphere) the carbon nanotubes form a sub monolayer coverage (<0.1%) on the

surface. A significant number of these tubes will contact both sets of arrays on the electrode surface. Hence, upon application of a potential difference between the two sets of electrodes an electrical current is passed, the magnitude of which is equal to the sum of the currents across all of the bridging contacts. The chronoamperometric response of the modified IDE-Au was measured using potential differences of 0.1, 0.3, 0.6, 0.9 V between the two sets of electrodes (Figure 7.7).

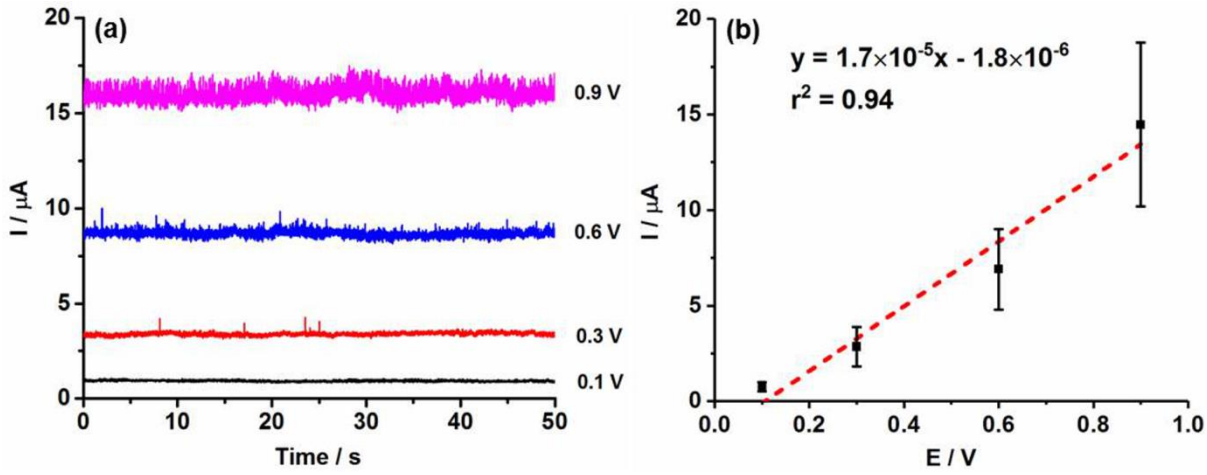

Figure 7.7: (a) Chronoamperometric profiles of IDE-Au dropcast with 0.7 ng of CNTs at 0.1, 0.3, 0.6 and 0.9 V. (b) The average current at 0.1, 0.3, 0.6 and 0.9 V. Dashed red line is the linear fitting curve.

The magnitude of the recorded current scales approximately linearly with the applied potential difference and in the absence of CNTs the current across the two electrodes is negligible. A plot of the average current measured against the applied potential was fitted and the resistance between the two arrays of microbands was determined to be 5.9×10^4 Ω. According to the image analysis in optical measurements, about 79 wt. % of the CNTs is longer than 5 μm and their average length is about 12 μm. The mass of a single CNT with 12 μm in length and 100 nm in diameter would be 1.26×10^{-13} g given the density of 1.34×10^6 g m^{-3}.[34] When 0.7 ng of CNTs was dropcast on the IDE-Au the maximum number of the

CNTs which are able to bridge the gaps of the IDE-Au can be estimated to be 4.4×10^3. Therefore, the expected resistance from a single CNT-gold contacts in air is calculated as $2.6 \pm 0.4 \times 10^8$ Ω by directly multiplying 4.4×10^3 to the total measured resistance ($5.9 \pm 0.8 \times 10^4$ Ω) of the dropcast CNTs.

Although indicative of a large contact resistance between the carbon nanotubes and the electrode, the above interpretation is subject to a number of assumptions. Specifically the potential drop between the CNT-CNT contacts[35] and the orientation of the tubes will be influential. Consequently, in order to gain a more accurate measurement of the resistance associated with the carbon nanotube a series of experiments on *individual* nanotubes were performed.

7.2.3.3 Nano-impact experiments of CNTs on the IDE-Au

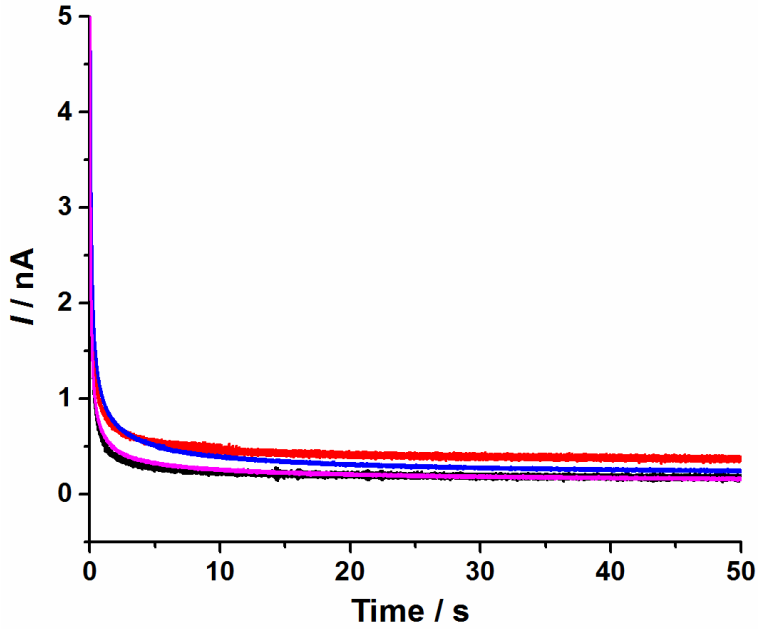

Figure 7.8: Chronoamperometry examples of IDE-Au in ethanol without CNT at 0.1 V.

Bridging contacts associated with individual carbon nanotubes were investigated by vertical submersion of the interdigitiated electrode array into a carbon nanotube containing solution

(1.2×10^{-13} M, subject to 10 min of sonication). The suspension contained no electrolyte. Due to Brownian motion the tubes collide randomly with the array. If a potential difference is held across the two interdigitated contacts and assuming an electrical contact is made between them, then an increase in current will be recorded corresponding to the presence and arrival of a carbon nanotube at the interface. The magnitude of the current gives a direct measure of the resistance associated with the bridge between the two interdigitated electrodes. Experimentally, in the absence of CNTs the background signal is related to small parasitic current between the interdigitated arrays, which is slightly variable (Figure 7.8) and the average corresponds to a resistance of ~ 0.5 GΩ. In the presence of CNTs current features were observed. A typical chronoamperometric profile is shown in Figure 7.9a (blue line). Although no features are present on some chronoamperometric profiles, a number of scans exhibit continuous current steps, where the current switches between two (Figure 7.9a) or more (Figure 7.10) apparently discrete levels. These steps are ascribed as relating to the collision of individual CNTs with the IDE-Au. Some of the impacting CNTs lie on the surface of the IDE-Au, and for those with the length over 5 μm their landing may bridge the gap between neighboring bands and consequently switch 'on' the electric circuit (Figure 7.9b). The regular current steps in one or more consecutive scans were recognized to be one collision event and attributed to the physical motion of the landing CNTs during the contact. 79 collision events (at 0.1 V) of individual CNTs were recorded with chronoamperometry and the current steps were analyzed, giving a mean current of $5.5 \pm 0.3 \times 10^{-10}$ A. The distribution of the current steps is shown in the inset of Figure 7.9a.

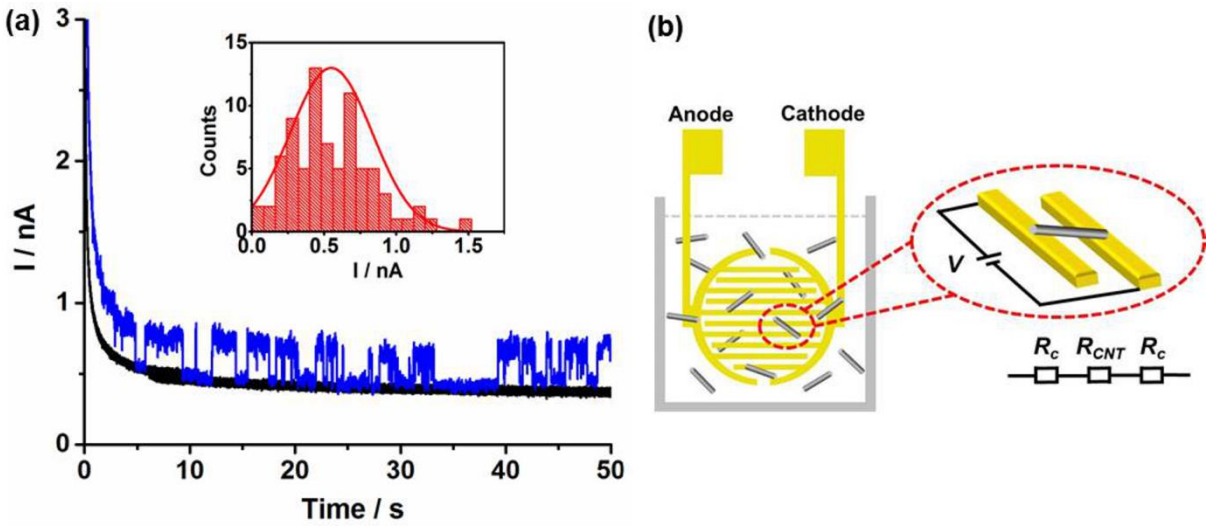

Figure 7.9: (a) Chronoamperometric profiles of IDE-Au in pure ethanol (black line) and a suspension of CNT (1.2×10^{-13} M) (blue line) at 0.1V. Inset: the distribution of current steps from 79 collision events. (b) Illustration of the nano-impact experiment of CNTs at IDE-Au.

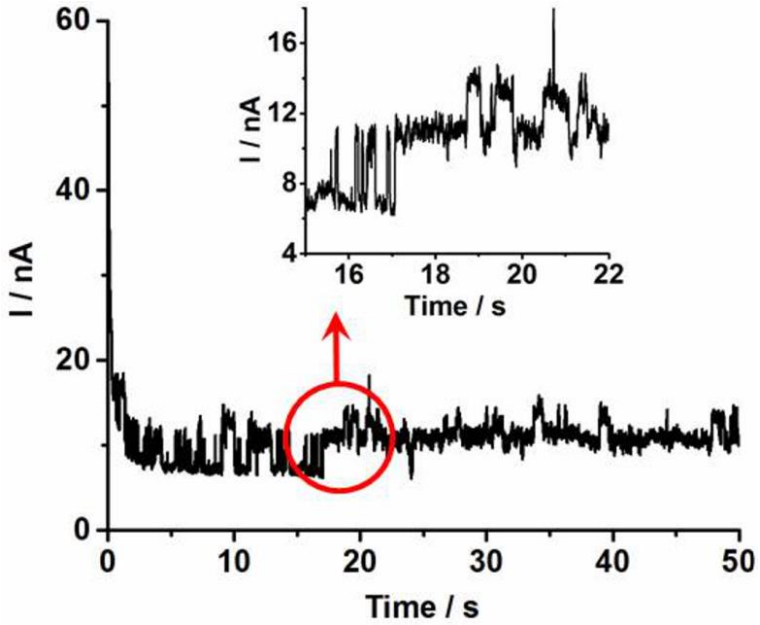

Figure 7.10: Chronoamperometry showing two discrete current steps at IDE-Au in a suspension of CNT (1.2×10^{-13} M) at 0.3 V.

In order to further evidence that the recorded current fluctuations are associated with the carbon nanotubes, nano-impact experiments were also performed in the suspension of the

CNTs with 120 min of sonication treatment. No current steps were detected in the chronoamperometic profile (Figure 7.11). From the optical microscopy measurements after 120 min of sonication the CNTs have a mean length of 3.2 ± 2.3 μm (Figure 7.6c). Consequently, after such a duration of sonication few of the tubes have the required length to bridge the inter-electrode gap. Since the concentration of the remaining CNTs longer than 5 μm is very low, the frequency of the collision events is decreased to undetectably low levels during the period of the measurement.

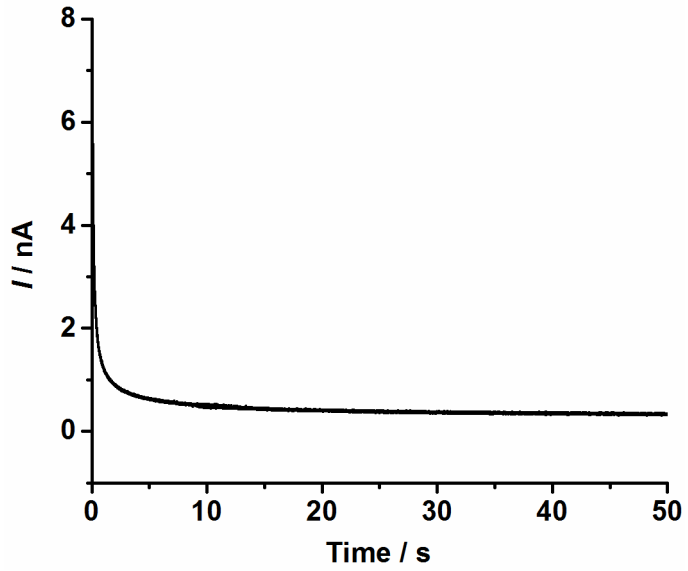

Figure 7.11: Chronoamperometric profiles of IDE-Au in a suspension of CNT (2.8×10^{-13} M) after sonication for 120 min at 0.1V.

Quantitative evaluation of the electrical transport performance of single CNTs on the gold substrate was further carried out by investigating the current steps at four different potentials applied between the arrays of microbands. Figure 7.12a shows the representative chronoamperometric profiles of IDE-Au in a suspension of CNTs (1.2×10^{-13} M) at 0.1, 0.3, 0.6 and 0.9 V. It is found that the current steps increase with the increase of the applied potential. During the measurements, 79, 58, 60, 44 current steps were collected at 0.1, 0.3, 0.6 and 0.9 V respectively, and the plot of average current against potential shows good

linearity (Figure 7.12b). Note that the current for each step was obtained by averaging the recorded current on the step. From the slope of the linear fitting the average total resistance of a single CNT bridging two gold substrates was realised with the nano-impact method and determined to be 1.1 ± 0.1 × 10^8 Ω. It should be recognized that the magnitude of the measured resistance is sensitive to the nature of the CNTs and the surface of the electrode.

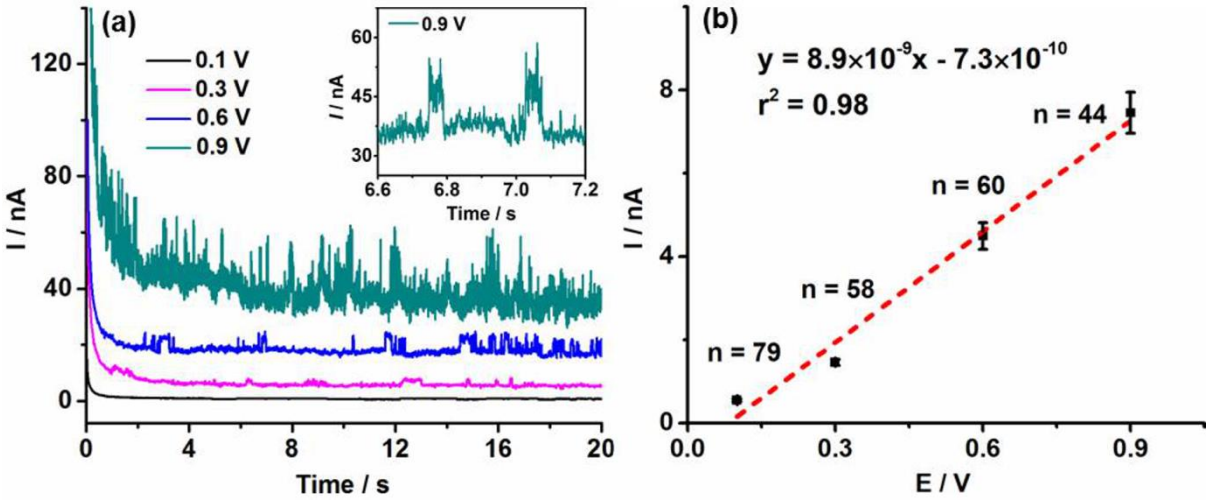

Figure 7.12: (a) Chronoamperometric profiles of IDE-Au in a suspension of CNT (1.2 × 10^{-13} M) at 0.1, 0.3, 0.6 and 0.9V. The Inset is a zoom in of the profile at 0.9V. (b) The average step current at 0.1, 0.3, 0.6 and 0.9V. Dashed red line is the linear fitting curve.

Returning to the ensemble experiments where a layer of CNTs were dropcast so that when 0.7 ng of CNTs were affixed to the IDE-Au, the maximum number of the CNTs which are able to bridge the gaps of the IDE-Au can be estimated to be 4.4 × 10^3 (see section 7.2.3.2). Therefore, the expected resistance from a single CNT-gold contact in air is calculated as 2.6 ± 0.4 × 10^8 Ω by directly multiplying 4.4 × 10^3 by the total measured resistance (5.9 ± 0.8 × 10^4 Ω) of the dropcast CNTs. This value is comparable to that (1.1 ± 0.1 × 10^8 Ω) obtained from the single CNT-gold contacts in ethanol via the nano-impact method. It is therefore indicated that, in terms of the electron transport performance, the property of the CNT-gold contacts in ethanol is similar to that in the dropcast CNTs which is *dry* and performed in the

absence of a solution phase. The slightly higher value of single CNT-gold contact resistance estimated from the ensemble measurement than that directly obtained using the nano-impact method is attributed as relating to a possible overestimate of the number of CNT bridging contacts formed.

We next consider the origin of this ~100 MΩ bridging resistance. As schematically shown in Figure 7.9b, for a single CNT with two ends contacting the gold substrate, the total measured resistance (R_{tot}) consists of the internal resistance of the CNT (R_{CNT}) and two contact resistances ($2R_c$) between the CNT and gold substrate. It has been reported that R_c contains both an intrinsic (R_{int}) and extrinsic (R_{ext}) component.[33] R_{int} is the quantum resistance ($R_{int} = R_q = 3.25$ kΩ) arising from interfacing with a quantum confined system,[36] while the R_{ext} component results from the transport of carriers at the CNT-gold contact. The literature reported resistivity of individual CNTs ranging from 7.8 μΩ•m to 117 μΩ•m,[37] moreover, the R_{CNT} of a single CNT with 5 μm in length (the distance between the electrode arrays) and 100 nm in diameter can be estimated to be within the range of 5-74 kΩ. This value for R_{CNT} is significantly less than the measured resistance ($1.1 \pm 0.1 \times 10^8$ Ω) for an individual bridging contact. Hence, the major component of the measured resistance is associated with the contact between the gold and carbon materials.

In addition, the magnitude of the impact currents is found to be insensitive to the size of the gap between the two electrodes. Nano-impact experiments were further conducted with the IDE-Au10 (both each band and gap are 10 μm in width) in the suspension of CNTs with 10 min of sonication treatments. The chronoamperometric profiles of the IDE-Au10 were recorded at 0.1 V and 36 current steps were analysed, giving an average step current of $3.7 \pm 0.8 \times 10^{-10}$ A. Herein, only those over 10 μm can bridge the gap of the IDE-Au10 and be detected in the chronoamperometric scans. It was found that the average step current from the IDE-Au10 is close to the value obtained with the IDE-Au5 used in this work (both each band

and gap are 5 μm in width) ($5.5 \pm 0.3 \times 10^{-10}$ A) at the same potential (comparison of current steps distribution is shown in Figure 7.13), indicating that the total measured resistance doesn't show dependence on the length of the CNTs which is proportional to R_{CNT}. It is thus further confirmed that the reminder R_c plays a dominant role in the transport performance of the CNTs on the gold substrate.

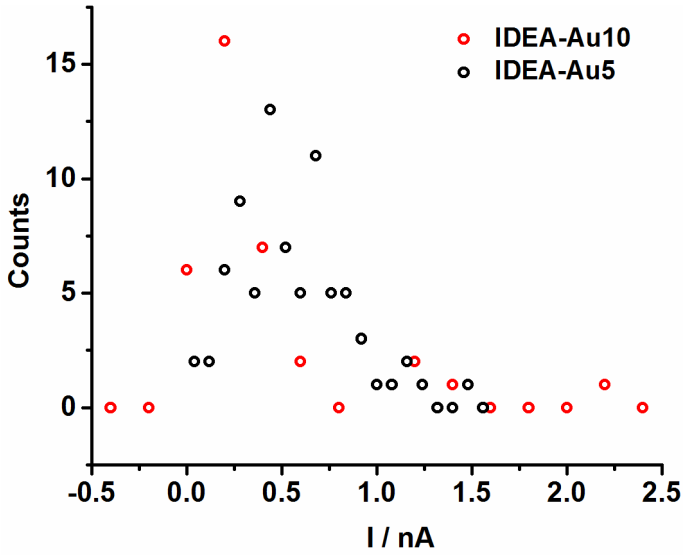

Figure 7.13: Comparison of the distribution of the current steps detected at IDE-Au5 (both each band and gap are 5 μm in width) and IDE-Au10 (both each band and gap are 10 μm in width).

The magnitude of this measured contact resistance (~50 MΩ) is significant and implies that, for many experimental cases, a practical limit in terms of the current per particle may exist. For an isolated particle with an associated current of only 1000 pA and a contact resistance of 50 MΩ, a measurable (50 mV) drop in potential at the electrode/particle interface will exist. An important and yet unanswered question is how the morphology and architecture of large ensembles of tubes – with numerous electrode-CNT contacts – may influence the connectivity of the entire CNT catalyst network.

7.3 Conclusions

In this chapter, the first work studied chronoamperometric and voltammetric responses of individual N-CNT-Pds at a gold electrochemical interface and compared to the response observed for impacts at a carbon fibre microwire electrode. Although the electronic properties of the electrode substrates differ significantly, the electrochemical responses are found to be essentially indistinguishable: current fluctuations of a similar magnitude were present for both substrates. Instead the fluctuations are attributed to the nano-motion of the nanotube at the electrode surface, which modulates its electrical contact and therefore the resulting current. Moreover, ex-situ adsorption to the gold electrode followed by drying of the interface improves the electrical connection between the nanoparticle and substrate such that the voltammetric response arising at a single carbon nanotube may be recorded in the absence of large current fluctuations.

Next, a new method allowing the rapid measurement of the resistance across individual CNT-electrode contacts was developed. The charge transfer process is shown to be significantly dominated by the presence of a high contact resistance (~50 MΩ). This is consistent with ensemble measurements made in the absence of solvent where a dilute layer of CNTs were affixed to the electrode surface. When studying new nanomaterials electrochemically, either at the single particle or bulk (ensemble) scale, the desire is for the experimental rate determining step to be the reaction at the catalyst/solution interface and not that of the contact between the electrode and nanomaterial. The magnitude of the above reported contact resistance suggests this may not always be the case.

Appendix

1. Overview of some of the numerous reports in the literature based on the use of CNTs as electrode materials and as the bridge between two electrodes

Some illustrative reports of applications of CNTs in the sustainable energy technologies (fuel cells, batteries and solar cells) and in electrochemical sensors and biosensors are listed as follows. In addition, some of the reports relating to the CNTs as the bridge between two electrodes are shown.

Fuel cells:

CNTs	Function	References
Carbon nanotubule-Pt nanoparticles membranes	Conducting materials	Carbon Nanotubule Membranes for Electrochemical Energy Storage and Production. *Nature* **1998**, *393*, 346-349
MWCNTs	Conducting materials	Improved Charge Transfer at Carbon Nanotube Electrodes. *Adv. Mater.* **1999**, *11*, 154-157
Pt/MWCNTs	Catalyst support	Preparation and Characterization of Multiwalled Carbon Nanotube-Supported Platinum for Cathode Catalysts of Direct Methanol Fuel Cells. *J. Phys. Chem. B* **2003**, *107*, 6292-6299
Pt-Ru/MWCNTs	Catalyst support	Characterization and Evaluation of Pt-Ru Catalyst Supported on Multi-Walled Carbon Nanotubes by Electrochemical

		Impedance. *J. Power Sources* **2006**, *160*, 915-924
Pt-Pd/CNT	Catalyst support	Carbon Nanotube Supported Platinum–Palladium Nanoparticles for Formic Acid Oxidation. *Electrochim. Acta* **2010**, *55*, 4217-4221
Pt-Fe, Pt-Co, Pt-Ni/CNT	Catalyst support	Fabrication of Bimetallic Pt–M (M = Fe, Co, and Ni) Nanoparticle/Carbon Nanotube Electrocatalysts for Direct Methanol Fuel Cells. *J. Power Sources* **2009**, *188*, 347-352
NSWCNT	Electro-catalyst	Highly Efficient Metal-Free Growth of Nitrogen-Doped Single-Walled Carbon Nanotubes on Plasma-Etched Substrates for Oxygen Reduction. *J. Am. Chem. Soc*. **2010**, *132*, 15127-15129
CNT-Graphene	Electro-catalyst	An Oxygen Reduction Electrocatalyst Based on Carbon Nanotube-Graphene Complexes. *Nat Nano* **2012**, *7*, 394-400
Pt-Ru/NCNT	Catalyst support	PtRu Nanoparticles Supported on Nitrogen-Doped Multiwalled Carbon Nanotubes as Catalyst for Methanol Electrooxidation. *Electrochim. Acta* **2009**, *54*, 4208-4215
CoO/NCNT	Catalyst support	Oxygen Reduction Electrocatalyst Based on Strongly Coupled Cobalt Oxide Nanocrystals and Carbon Nanotubes. *J. Am. Chem. Soc.* **2012**, *134*, 15849-15857

$CoMn_2O_4$/PDDA-CNTs	Catalyst support	Noncovalent Hybrid of $CoMn_2O_4$ Spinel Nanocrystals and Poly (Diallyldimethylammonium Chloride) Functionalized Carbon Nanotubes as Efficient Electrocatalysts for Oxygen Reduction Reaction. *Carbon* **2013**, *65*, 277-286
Pt/PAH-CNTs	Catalyst support	Carbon Nanotubes Decorated with Pt Nanoparticles Via Electrostatic Self-Assembly: A Highly Active Oxygen Reduction Electrocatalyst. *J. Mater. Chem.* **2010**, *20*, 2826-2830

Batteries:

CNTs	Functions	References
LBL-CNT-coated on ITO	Conducting materials	High-Power Lithium Batteries from Functionalized Carbon-Nanotube Electrodes. *Nat Nano* **2010**, *5*, 531-537
Fe_3O_4/CNT	Conducting materials	Structure and Electrochemical Performance of Nanostructured Fe_3O_4/Carbon Nanotube Composites as Anodes for Lithium Ion Batteries. *Electrochim. Acta* **2010**, *55*, 1140-1144
MnO_2/CNT	Conducting materials	Coaxial MnO_2/Carbon Nanotube Array Electrodes for High-Performance Lithium Batteries. *Nano Lett.* **2009**, *9*,

		1002-1006
CNT-conducting polymer	Conducting materials	Flexible, Aligned Carbon Nanotube/Conducting Polymer Electrodes for a Lithium-Ion Battery. *Chem. Mater.* **2007**, *19*, 3595-3597
SnO_2-Au/CNT	Conducting materials	One-Pot Synthesis of Carbon Nanotube@SnO_2−Au Coaxial Nanocable for Lithium-Ion Batteries with High Rate Capability. *Chem. Mater.* **2008**, *20*, 6951-6956

Solar cells:

SWCNT−TiO_2	Conducting materials	Single Wall Carbon Nanotube Scaffolds for Photoelectrochemical Solar Cells. Capture and Transport of Photogenerated Electrons. *Nano Lett.* **2007**, *7*, 676-680
Pt nanoparticles on SWCNT	Catalyst support	Platinum Nanoparticle-Adsorbed Carbon Nanotube Yarns for Efficient Fiber Solar Cells. *ACS Nano* **2012**, *6*, 7191-7198.
CNT-CdS	Conducting materials	Photoinduced Electron Transfer in Aqueous Carbon Nanotube/Block Copolymer/Cds Hybrids: Application in the Construction of Photoelectrochemical Cells. *J. Mater. Chem.* **2009**, *19*, 8990-8998
SWCNT-Polymer	Conducting materials	Combining Single Wall Carbon Nanotubes and Photoactive Polymers

		for Photoconversion. *J. Am. Chem. Soc.* **2005**, *127*, 10051-10057
SWCNT−TiO_2	Conducting materials	Photoreactive TiO_2/Carbon Nanotube Composites: Synthesis and Reactivity. *Environmental Science & Technology* **2008**, *42*, 4952-4957
Aligned carbon nanotube	Conducting materials	A Free-Standing Aligned-Carbon-Nanotube/Nanocomposite Foil as an Efficient Counter Electrode for Dye Solar Cells. *Energy & Environmental Science* **2012**, *5*, 8377-8383

Sensors:

CNTs	Electrochemical biosensors	Carbon-Nanotube Based Electrochemical Biosensors: A Review. *Electroanalysis* **2005**, *17*, 7-14
CNT-Nafion	Electrochemical biosensors	Solubilization of Carbon Nanotubes by Nafion toward the Preparation of Amperometric Biosensors. *J. Am. Chem. Soc.* **2003**, *125*, 2408-2409
CNT-Teflon	Electrochemical sensors and biosensors	Carbon Nanotube/Teflon Composite Electrochemical Sensors and Biosensors. *Anal. Chem.* **2003**, *75*, 2075-2079
CNTs	Electro-catalyst	Low-Potential Stable Nadh Detection at Carbon-Nanotube-Modified Glassy Carbon Electrodes. *Electrochem. Commun.* **2002**, *4*, 743-746

Pt nanoparticles/CNT	Conducting materials	Electrochemical Biosensing Platforms Using Platinum Nanoparticles and Carbon Nanotubes. *Anal. Chem.* **2004**, *76*, 1083-1088

CNTs as the bridge between two electrodes:

SWCNT	Conducting materials	Individual single-walled carbon nanotubes as nanoelectrodes for electrochemistry. *Nano Lett.* **2005**, *5*, 137-142.
SWCNT	Conducting materials	Carbon nanotube intramolecular p-i-n junction diodes with symmetric and asymmetric contacts. *Sci. Rep.* **2016**, *6*, 22203.
SWCNT	Conducting materials	High-work-function metal/carbon nanotube/low-work-function metal hybrid junction photovoltaic device. *NPG Asia Mater.* **2015**, *7*, e220.
CNTs	Conducting materials	Defining and Overcoming the Contact Resistance Challenge in Scaled Carbon Nanotube Transistors. *ACS Nano* **2014**, *8*, 7333-7339.
SWCNT	Conducting materials	High-Performance Field Effect Transistors from Solution Processed Carbon Nanotubes. *ACS Nano* **2010**, *4*, 6659-6664.

2. Comparison of CVs of HOR for different CNT-electrode contacts

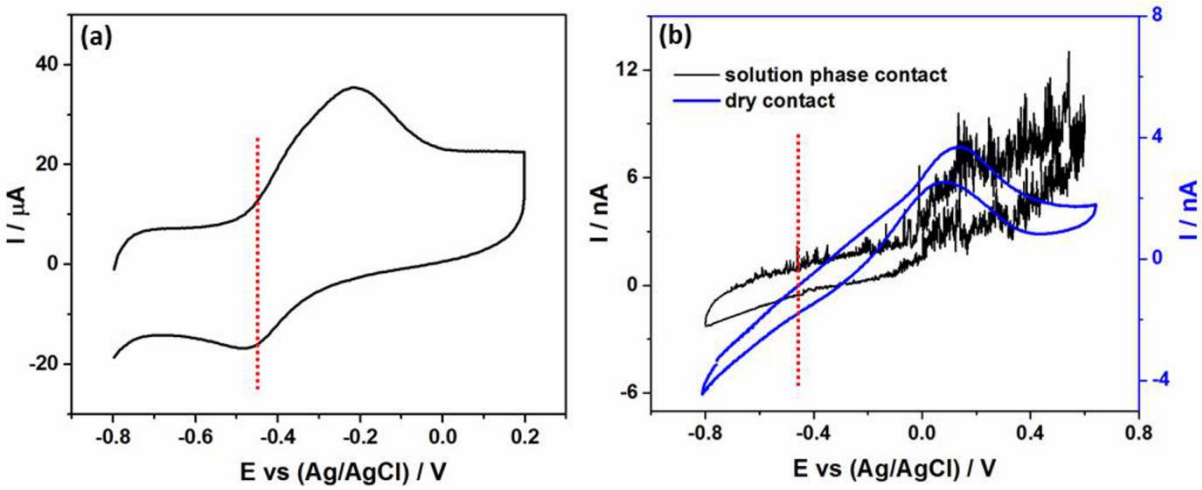

Figure 7.14: (a) CV of HOR at the glassy carbon electrode dropcast with N-CNT-Pd; (b) CV of HOR for single N-CNT-Pd-electrode contact in the solution phase (black line) and for N-CNT-Pd-electrode contact in the absence of solvent (blue line). Vertical dot line represents the reversible half-wave potential ($E_{1/2}$) for the HOR (-0.194 V vs. SHE).

In Figure 7.14a, the CV shows a quasi-irreversible peak for HOR at the ensemble Pd/CNT modified electrode. The mid-point potential (-0.348 vs. Ag/AgCl) is relatively close to the expected reversible HOR half-wave potential (-0.449 vs. Ag/AgCl) (-0.194 V vs. SHE)[38], indicating the low resistance for the CNT 'mat'-electrode contact. However, HOR at both single CNT-electrode contact in the solution phase via the nano-impact method (black line) and the dry CNT-electrode contact (blue line) occur at comparatively high overpotentials. Although the removal of the solvent reduces the current fluctuation, there is still no major change in the position of the HOR wave. Hence in this case we conclude that the conductivity of CNT-electrode contact is not dominated by the presence of the solvent.

References

[1] H. Hodson, X. Li, C. Batchelor-McAuley, L. Shao and R. G. Compton, *J. Phys. Chem. C*, **2016**, *120*, 6281-6286.

[2] X. Li, C. Batchelor-McAuley, L. Shao, S. V. Sokolov, N. P. Young and R. G. Compton, *J. Phys. Chem. Lett.*, **2017**, *8*, 507-511.

[3] J. Kim, B.-K. Kim, S. K. Cho and A. J. Bard, *J. Am. Chem. Soc.*, **2014**, *136*, 8173-8176.

[4] J. Kim and A. J. Bard, *J. Am. Chem. Soc.*, **2016**, *138*, 975-979.

[5] W. J. Royea, T. W. Hamann, B. S. Brunschwig and N. S. Lewis, *J. Phys. Chem. B*, **2006**, *110*, 19433-19442.

[6] R. Dasari, D. A. Robinson and K. J. Stevenson, *J. Am. Chem. Soc.*, **2013**, *135*, 570-573.

[7] R. Dasari, K. Tai, D. A. Robinson and K. J. Stevenson, *ACS Nano*, **2014**, *8*, 4539-4546.

[8] R. Dasari, B. Walther, D. A. Robinson and K. J. Stevenson, *Langmuir*, **2013**, *29*, 15100-15106.

[9] T. R. Bartlett, C. Batchelor-McAuley, K. Tschulik, K. Jurkschat and R. G. Compton, *ChemElectroChem*, **2015**, *2*, 522-528.

[10] J. G. Simmons, *J. Appl. Phys.*, **1963**, *34*, 1793-1803.

[11] Y. V. Sharvin, *Sov. Phys. JETP*, **1965**, *21*, 655-656.

[12] R. Holm and E. Holm, *Electric Contacts: Theory and Application, 4th ed.*, Springer-Verlag, Berlin/Heidelberg/New York, **1967**.

[13] *CRC Handbook of Chemistry and Physics*, CRC Press, Cleveland, **1974**.

[14] P. R. Wallace, *Phys. Rev.*, **1947**, *71*, 622-634.

[15] A. K. Dutta, *Phys. Rev.*, **1953**, *90*, 187-192.

[16] F. Gloaguen, J. M. Léger and C. Lamy, *J. Electroanal. Chem.*, **1999**, *467*, 186-192.

[17] X. Jiao, C. Batchelor-McAuley, E. Kätelhön, J. Ellison, K. Tschulik and R. G. Compton, *J. Phys. Chem. C*, **2015**, *119*, 9402-9410.

[18] J. Ellison, C. Batchelor-McAuley, K. Tschulik and R. G. Compton, *Sens. Actuators, B*, **2014**, *200*, 47-52.

[19] A. Ortega and J. G. a. d. l. Torre, *J. Chem. Phys.*, **2003**, *119*, 9914-9919.

[20] K. Kanghyun, J. Doyoung, L. Kangho, K. Haeyong, Y. Byung Yong, L. Jung Il and K. Gyu Tae, *Nanotechnology*, **2010**, *21*, 335702.

[21] E. Kätelhön, K. J. Krause, B. Wolfrum and R. G. Compton, *ChemPhysChem*, **2014**, *15*, 872-875.

[22] L. S. Y. Ly, C. Batchelor-McAuley, K. Tschulik, E. Kätelhön and R. G. Compton, *J. Phys. Chem. C*, **2014**, *118*, 17756-17763.

[23] J. Suntivich, H. A. Gasteiger, N. Yabuuchi, H. Nakanishi, J. B. Goodenough and Y. Shao-Horn, *Nat Chem*, **2011**, *3*, 546-550.

[24] Y. Jiao, Y. Zheng, M. Jaroniec and S. Z. Qiao, *Chem. Soc. Rev.*, **2015**, *44*, 2060-2086.

[25] M. K. Debe, *Nature*, **2012**, *486*, 43-51.

[26] V. Stamenkovic, B. S. Mun, K. J. J. Mayrhofer, P. N. Ross, N. M. Markovic, J. Rossmeisl, J. Greeley and J. K. Nørskov, *Angew. Chem.*, **2006**, *118*, 2963-2967.

[27] V. R. Stamenkovic, B. Fowler, B. S. Mun, G. Wang, P. N. Ross, C. A. Lucas and N. M. Marković, *Science*, **2007**, *315*, 493-497.

[28] H. Lee, S. E. Habas, G. A. Somorjai and P. Yang, *J. Am. Chem. Soc.*, **2008**, *130*, 5406-5407.

[29] C. Bianchini and P. K. Shen, *Chem. Rev.*, **2009**, *109*, 4183-4206.

[30] Y. Li, W. Zhou, H. Wang, L. Xie, Y. Liang, F. Wei, J.-C. Idrobo, S. J. Pennycook and H. Dai, *Nat Nano*, **2012**, *7*, 394-400.

[31] X. Li, C. Batchelor-McAuley, S. A. I. Whitby, K. Tschulik, L. Shao and R. G. Compton, *Angew. Chem. Int. Ed.*, **2016**, *55*, 4296-4299.

[32] C. Lan, P. Srisungsitthisunti, P. B. Amama, T. S. Fisher, X. F. Xu and R. G. Reifenberger, *Nanotechnology*, **2008**, *19*, 125703.

[33] A. D. Franklin, D. B. Farmer and W. Haensch, *ACS Nano*, **2014**, *8*, 7333-7339.

[34] D. J. Yang, Q. Zhang, G. Chen, S. F. Yoon, J. Ahn, S. G. Wang, Q. Zhou, Q. Wang and J. Q. Li, *Phys. Rev. B*, **2002**, *66*, 165440.

[35] A. F. Holloway, D. A. Craven, L. Xiao, J. D. Campo and G. G. Wildgoose, *J. Phys. Chem. C*, **2008**, *112*, 13729-13738.

[36] S. Datta, *Quantum Transport: Atom to Transistor*, Cambridge University Press, Cambridge, **2005**.

[37] H. Dai, E. W. Wong and C. M. Lieber, *Science*, **1996**, *272*, 523-526.

[38] C. Lin, X. Jiao, K. Tschulik, C. Batchelor-McAuley and R. G. Compton, *J. Phys. Chem. C*, **2015**, *119*, 16121-16130.

Conclusions

Electron transfer at solid/liquid interfaces underpins energy transformation science and technology most notably in fuel cells, solar cells and batteries. Smaller dimensions of the electroactive surface create conditions of high mass-transport permitting the resolution of faster electrode kinetic effects and hence providing better mechanistic understandings. This thesis has investigated some key reactions involved in the energy conversion applications at single catalytic nanoparticles-the palladium nanoparticle decorated carbon nanotube (CNT-Pd) via the 'nano-impact' method. The following conclusions have been drawn:

1. The current amplification by the production of under-potential deposited hydrogen (H_{UPD}) from proton reduction on palladium nanoparticles decorated carbon nanotubes (CNT-Pd) was used as an indicator to evidence the electrode collision of individual carbon nanotubes. The present method not only enables the detection and characterization of the individual CNT-Pd in a non-destructive and stochastic way but also reveals the good conductivity and reactivity of the CNT-Pds.

2. A facile procedure which enables rapidly and easily gathering of single nanotube voltammetry was established by investigating the hydrogen oxidation reaction (HOR) at single CNT-Pds. Single catalytic CNT-Pds reside on the support electrode for such sufficiently long time once colliding with the electrode that cyclic voltammetry of HOR on single decorated carbon nanotube can be realized.

3. Single nanotube voltammetry of the oxygen reduction reaction (ORR), in combination with new theoretical models, demonstrates that the reduction of oxygen on Pd involves the initial formation of absorbed superoxide $O_2^{\cdot-}$ (ads) with fast electron transfer kinetics but with an apparent low transfer coefficient due to double layer effects arising from the coulombic

interactions of the adsorbed superoxide species inside the double layer. This gives new physical insights into some of the many electrode processes involving adsorbed intermediates.

4. Comparison of the voltammograms of formate/methanol oxidation on CNT-Pd ensembles and well-separated individual CNT-Pds shows that the inhibition from the Pd oxide formation on the oxidative processes on the ensembles became retarded with the use of well separated individual N-CNT-Pd where high mass transport conditions prevail, suggesting requirements for catalyst design developments in fuel cells.

5. Finally, the investigation of the origins of the current fluctuation observed in single nanotube voltammetry reveals that the physical motion of the nanotube at the electrode surface is responsible for the modulation of current. A new method allowing the rapid measurement of the resistance across individual CNT-electrode contacts further indicates that the charge transfer process is significantly dominated by the presence of a high contact resistance, providing major implications for the widespread use of CNTs in electrochemical applications.

The above significant discoveries on single catalytic nanoparticles demonstrate the importance of methodology development for studying electrochemistry at nanoscale on both fundamental and applied electrochemistry.